KIT SCIENTIFIC REPORTS 7624

Radionuclide Source Term for HLW Glass, Spent Nuclear Fuel, and Compacted Hulls and End Pieces (CSD-C Waste)

Bernhard Kienzler
Marcus Altmaier
Christiane Bube
Volker Metz

KIT Scientific Publishing

Bernhard Kienzler, Marcus Altmaier, Christiane Bube, Volker Metz

Radionuclide Source Term for HLW Glass, Spent Nuclear Fuel, and Compacted Hulls and End Pieces (CSD-C Waste)

Karlsruhe Institute of Technology
KIT SCIENTIFIC REPORTS 7624

Radionuclide Source Term for HLW Glass, Spent Nuclear Fuel, and Compacted Hulls and End Pieces (CSD-C Waste)

by
Bernhard Kienzler
Marcus Altmaier
Christiane Bube
Volker Metz

KIT Scientific Publishing

Report-Nr. KIT-SR 7624

Hinweis

Dieser Bericht wurde von KIT-INE gemäß Angebot Nr. 20003459 vom 05. 10 2010 im Auftrag der Gesellschaft für Anlagen- und Reaktorsicherheit (GRS) mbH, Schwertnergasse 1, 50667 Köln im Rahmen des Projekts „Vorläufige Sicherheitsanalyse Gorleben“ (VSG) erstellt.
Der Bericht gibt die Auffassung und Meinung des Auftragnehmers wieder und muss nicht mit der Meinung des Auftraggebers übereinstimmen.
Der Bericht wurde unter der Bezeichnung KIT-INE 003/11 an den Auftraggeber (GRS) übergeben.

Impressum

Karlsruher Institut für Technologie (KIT)
KIT Scientific Publishing
Straße am Forum 2
D-76131 Karlsruhe
www.ksp.kit.edu

KIT – Universität des Landes Baden-Württemberg und
nationales Forschungszentrum in der Helmholtz-Gemeinschaft

KIT Scientific Publishing 2012
Print on Demand

ISSN 1869-9669
ISBN 978-3-86644-907-7

Radionuclide Source Term for HLW Glass, Spent Nuclear Fuel, CSD-C Waste

Abstract

A source term for release of radionuclides from high-level waste glass, spent nuclear fuel, and compacted hulls and end pieces of fuel elements (CSD-C waste) is derived for different scenarios of a final repository within the salt dome Gorleben. The considered scenarios assume the presence of NaCl or $MgCl_2$ rich solutions in the near field of the waste products. Formulation of the source term is based on a discussion of kinetic and thermodynamic mobilization / retention and the influence of temperature on these processes. The expected geochemical conditions for the scenarios are analyzed. Maximum expected concentrations of the radionuclides Am, Th, U, Np, Pu, Tc, Zr and rare earth elements are derived for the simplified scenarios. These scenarios are based on the absence of carbonate and elevated temperature effects are not treated explicitly. Except for sorption on canister materials and canister corrosion products, radionuclide retention by sorption processes is of minor importance for the proposed backfill of the repository concepts.

Radionuklid-Quellterm für hochradioaktives Glas, abgebrannten Kernbrennstoff und kompaktierte Hülsen und Endstücke (CSD-C)

Zusammenfassung

Ein Quellterm für die Radionuklidfreisetzung aus hochradioaktivem Glas, abgebranntem Kernbrennstoff und kompaktierten Hülsen und Endstücke von Brennelementen (CSD-C Abfälle) wird für verschiedene potentielle Entwicklungen eines Endlagers im Salzstock Gorleben abgeleitet. Für die Ableitung des Quellterms werden Szenarien angenommen, die die Anwesenheit von NaCl- und $MgCl_2$-reichen Lösungen im Nahfeld der Abfallprodukte unterstellen. Die kinetisch und thermodynamisch kontrollierten Prozesse der Radionuklidfreisetzung / -rückhaltung und der Temperatureinfluss auf diese Prozesse werden diskutiert. Die erwarteten geochemischen Bedingungen werden analysiert. Die maximal zu erwartenden Konzentrationen der Radionuklide Am, Th, U, Np, Pu, Tc, Zr und Seltenenerdelemente werden im Rahmen vereinfachter Szenarien für carbonatfreie Systeme ohne explizite Berücksichtigung von höheren Temperaturen abgeleitet. Mit Ausnahme der Sorption an Behältermaterialien ist die Radionuklidrückhaltung durch Sorptionsprozesse an den gegenwärtig vorgeschlagenen Versatzstoffen von geringer Bedeutung.

TABLE OF CONTENTS

LIST OF TABLES

LIST OF FIGURES

Abbreviations

BWR	boiling-water reactors
FIAP	fraction of inventory in the aqueous phase
FP	fission product
FWP	Framework programme
HLW	high-level waste
IRF	instant release fraction
KKI	Isar nuclear power plant (“Kernkraftwerk Isar”)
KKO	Obrigheim nuclear power plant (“Kernkraftwerk Obrigheim”)
KWU	nuclear power plant union (“Kraftwerk Union”)
LET	linear energy transfer
LWR	light water reactors
M	Molar, Mol H^+ per Liter
m	molal, Mol H^+ per kg H_2O
MOX	mixed-oxide fuel
NPP	nuclear power plant
PWR	pressurized-water reactors
RN	radionuclides
RT	room temperature
UOX	Uranium-oxide fuel
WP	work package
Zry	Zircaloy

1 Introduction

The formulation of a source term for radionuclide release from high-level waste glass, spent nuclear fuel, and compacted hulls and end pieces of fuel elements (CSD-C waste) supports the fundamental requirements regarding the safety concept and design of a final repository for heat-generating radioactive waste defined by the German Federal Ministry for the Environment, Nature Conservation and Nuclear Safety [1]. According to these "Safety Requirements Governing the Final Disposal of Heat-Generating Radioactive Waste", manageability of the waste containers must be guaranteed for a period of 500 years.

A survey and an update of a radionuclide source term study [2, 3] that had been developed earlier for high-level waste glass, spent nuclear fuel of power reactors (boiling water reactors, BWR, and pressurized water reactors, PWR) and compacted CSD-C wastes is compiled and adapted by KIT-INE in this report. In accordance with the goals of the project "Preliminary Safety Analysis Gorleben" (vSG) [4] the specific objectives of the present report are

- to compile the present scientific knowledge on the behavior of heat-generating waste under saline conditions,
- to describe the relevant geochemical conditions and radionuclide mobilization / retention processes in the near field of the waste products,
- to provide data for a preliminary radionuclide source term with respect to scenarios, which include the presence of NaCl or $MgCl_2$ rich solutions in the near field,
- to discuss uncertainties of the source term data and
- to identify issues requiring further research.

Due to simplifications in the definition of the scenario and geochemical boundary conditions, the formulation of the radionuclide source term has explicitly a preliminary and orienting character and does not supersede the development of a site-specific radionuclide source term in a Safety Case for a potential repository in the Gorleben salt dome.

The previous radionuclide source term studies [2, 3] are based upon several reports which had been prepared by FZK-INE on behalf of the Federal Office for Radiation Protection (BfS) in the years 1995 until 2001. For the development of a source term for vitrified high-level wastes, results of the BfS project are updated by a publication of Grambow and Müller (2001) on the kinetics of glass dissolution [5] and the results reported in the European 6^{th} Framework Programme (FWP) Integrated Project NF-Pro [6]. The NF-Pro report summarizes the result of previous EU projects such as GLASTAB (Long-term behavior of glass: Improving the glass source term and substantiating the basic hypotheses) and GLAMOR (A Critical Evaluation of the Dissolution Mechanisms of High-level Waste Glasses in Conditions of Relevance for Geological Disposal).

The source term for spent nuclear fuel of light water reactors (LWR) bases upon several reports which have been prepared by FZK-INE within European projects [7-9] and on behalf of the Federal

Office for Radiation Protection (BfS) in the years 1995 until 2001 [10, 11]. Additional results have been reported in the European 5th and 6th FWP projects SFS [12], NF-Pro [6] and MICADO [13]. These projects covered

(1) the evolution of spent nuclear fuel prior to water ingress,

(2) the quantification of key processes affecting the source term for the spent nuclear fuel matrix under geological repository conditions.

Regarding spent nuclear fuels, the discussion of mobilization / retention processes is updated by recent publications on the hydrogen effect and counteracting processes on the UO_2 matrix dissolution as well as the instant / rapid release fraction of radionuclides. The documentation of the present scientific knowledge on the behavior of spent nuclear fuel deals mainly with spent UOX. Documentation and discussion of spent MOX fuel is very limited because only very few experimental data are available.

Zircaloy, a zirconium alloy with various metallic constituents, is commonly used as the fuel rod cladding material. While in boiling water reactors Zircaloy-2 is the preferred cladding material, Zircaloy-4 is used in pressurized water reactors. The mass of Zircaloy in German PWRs amounts to about 290 kg/Mg HM (heavy metal), in BWRs to about 320 kg/Mg HM (including the fuel assembly channels) [14]. The structural materials consist of 13 kg/t HM Inconel with 7-18 wt. % Fe and < 2000 ppm Co according to data provided in the vSG project [15]. The end pieces consist also of Inconel[1] with a mass of 42 kg/tHM. Inconel alloys are typically used in high temperature applications. According to Neeb [14], different types of Inconel are used, which are separated from the UO_2 fuel during reprocessing and compacted. This kind of waste is called CSD-C and is considered as heat producing waste, too. Up to now, information on the radionuclide source term for this waste form is scarce.

The following topics are covered and updated by this report:

- Data and processes for the different waste forms
    - HLW Glass
      - Kinetics of HLW glass dissolution
      - Temperature effects
    - Spent Nuclear Fuel (UOX/MOX)
      - Kinetics of spent nuclear fuel dissolution
      - Instant / rapid release fraction
      - Matrix dissolution
      - Temperature effects
      - Hydrogen effect
    - Compacted hulls, end pieces and spacers (CSD-C waste)
      - RN-Inventory of the CSD-C waste forms
    - - Initial Composition of the materials
      - Reactions during irradiation in a nuclear reactor

[1] Inconel is a trademark and refers to a group of austenitic nickel-chromium-based alloys.

- Boundary conditions for the considered evolution scenario in the case of high-level waste glass, spent nuclear fuel and CSD-C waste
- Radionuclide source term
  - Kinetically controlled radionuclide mobilization including the instant release of SNF
  - Thermodynamically controlled radionuclide mobilization
  - Effect of temperature on radionuclide solubility
- Solubility limits for actinides, lanthanides and technetium
- Discussion of sorption effects
- Open questions and recommendations (R&D)

2 General remarks on estimation of radionuclide solubility

The solubility of actinides and long-lived fission products was investigated intensively during the last decades. The investigations aimed both on experimentally supported solubility data to be used for source terms and on the determination of thermodynamic data which are the basis for geochemical modeling. Only limited amounts of radionuclides can be dissolved in water. The solubility of a substance in water is a specific material parameter which can be described by three factors:

- Solubility controlling solid (solubility product, log $K°_{sp}$)
- Complexation reactions (complex formation constants, log $\beta°$)
- Ion-ion interactions (activity coefficients γ)

The experimentally measured solubility can be considered as a superposition of these factors. A thermodynamic parameterization requires systematization and separation of these factors and is scientifically ambitious. In the scope of the OECD-NEA thermodynamic database project (NEA-TDB), data for Am, Th, U, Np, Pu and Tc have been collected and critically reviewed [16-21]. These data from the NEA TDB are valid for solutions of lower salinity and not for highly concentrated salt brines. In highly concentrated salt solutions, the effect of the ion-ion interaction coefficients gets increasingly important. A correct description of such saline systems requires a reliable, complete and consistent set of model parameters, such as the Pitzer parameters [22]. A complete set of thermodynamic and model data is available for some systems only. No Pitzer parameters exist e.g. for actinide-carbonate species in $MgCl_2$ solutions. As a consequence, it is not possible for all relevant geochemical conditions to predict radionuclide solubility by geochemical modeling. Therefore, the maximum radionuclide concentrations estimated for the source term need to be derived from experimentally well investigated reference systems and evaluated accordingly.

The solubility data provided by this study represent radionuclide concentrations in the solutions without considering any sorption effects onto solid materials. They represent upper limit estimates. It is known from numerous studies in salt brines, that sorption will provide for significant radionuclide retention and lower concentrations away from the source (or if the source is exhausted) in the aqueous system than projected for pure thermodynamic solubilities. Thermodynamic solubility represents an upper limit borderline for maximal achievable concentration in a given geochemical system.

2.1 Methods for estimating radionuclide solubilities

The methods for estimation of radionuclide solubilities are described in detail, elsewhere [23]. According to the boundary conditions for the safety analysis, the radionuclide solubility will be estimated for two different simplified conditions:

1) pure saturated carbonate-free NaCl and

2) pure saturated carbonate-free $MgCl_2$ solutions.

The following criteria are applied for estimating the radionuclide solubilities:

Characteristics of the salt solutions according to the dominating cations NaCl / $MgCl_2$. The characteristics of the main components (cations and anions) of the geochemical milieu influence the solubility of actinides in brines. NaCl and $MgCl_2$ systems need to be treated separately. The evaluation of the ion-ion interactions is based on the ionic strength and is defined by the main components.

Effect of pH (-log(m_{H+}), molal concentration of H^+, concentration scale: mol/kg H_2O***).*** The solubility and speciation of actinides are strongly depending on pH. This behavior is usually observed over a wide range of pH conditions. Consequently, small changes of the pH might affect the solubility of actinides strongly. The expected pH ranges need to be defined.

Redox conditions and dominating actinide oxidation state. The solubility and speciation of actinides depend strongly on their oxidation state. These are correlated with the ambient geochemical milieu and redox conditions. Under the considered evolution scenario, reducing conditions are prevailing over the long-term.

Solubility controlling solids. Actinides may form different solids, depending on geochemical conditions. Different solids may have completely different solubilities. Therefore the knowledge of the solid actinide phases controlling solubility for a given set of boundary conditions is indispensible. Colloids of tetravalent actinides are additional species which contribute significantly to the total solubility.

Complexing ligands. Actinides show a strong tendency towards hydrolysis. Complexation reactions with other inorganic ligands like carbonate or nitrate are also known. Complex formation may also take place with other ligands (EDTA, organic acids, detergents, isosaccharinic acid, etc) which can be present in the low level waste forms. Hydrolysis reactions and the formations of actinide-hydroxide complexes are dominating species under the assumed geochemical conditions; the effect of other complexing ligands has not been assessed within this study reflecting the assumption of simplified scenarios under absence of carbonate.

Ionic strength. The effect of ion-ion interactions may significantly increase the solubility of some actinides. It is not possible to reliably extrapolate radionuclide solubility exclusively from data obtained at low ionic strength. Assessment of the influence of ion-interaction processes on radionuclide solubility therefore is of high importance.

Temperature. The temperature dependence of complex formation constants and the activity coefficients of the different aquatic species are only available for a limited number of species. For solids, the crystallinity increases by increasing temperatures and the tendency towards formation of metastable solids observed at room temperature is less pronounced. Complex formation reactions, however, tends to increase with increasing temperatures. It should be noted, that both the solubility products (of the solubility limiting solid phase) and the tendency towards complex formation (with ligands present in solution) determine the solubility for a given element or compound and given boundary conditions. From this it can be assumed that opposite trends in solid phase stability and complex formation are likely to offset, resulting in rather moderate changes in total solubility with temperature. If concentrations do not change dramatically with increasing temperature this might be due to a compensation of counter current effects, e.g. decreased solubility and increased tendency

towards complex formation. In this case, the distribution of the aqueous species may change drastically at nearly constant overall nuclide concentration. Due to a lack of thermodynamic data for elevated temperatures, the solubility limits for room temperature are assumed to be valid also for elevated temperature conditions. As this approach is certainly a strong simplification introducing rather large uncertainties, a verification of radionuclide solubility limits for elevated temperature conditions is necessary, as it is mentioned in the outlook (see Chapter 0).

Determination of thermodynamic constants based on analogies

In many cases, the RN solubility can be calculated or derived directly from experiments or interpolated at least. Due to experimental problems or a lack of suited experimental methods, a number of systems cannot be accessed experimentally. In such cases, suited analogue systems have to be applied. In some cases, experimental data of analoga can be used, e.g. Nd(III), Eu(III) or Cm(III) for Am(III). Furthermore, the thermodynamic data for Np(V) and U(VI) are well established, whereas reliable data for Pu(V) or Pu(VI) are largely missing. For these systems, the application of data from analogues is often to be preferred.

Most of the chemical properties of the actinide elements in the oxidation states An(III, IV, V or VI), except for redox reactions, show distinct similarities [24, 25]. The systematic trends in their behavior are frequently correlated with their effective charge and the ionic radius. This well known chemical principle of the oxidation state analogues together with systematic trends in the actinide series can be used to estimate solubility limitations.

The following parameters have to be considered:

(1) Solubility controlling solids (solubility product)

Actinides (and lanthanides) of the same oxidation state (III and IV) and comparable ionic size form oxides, hydroxides and carbonate solids with the same stoichiometries and very similar crystalline structures. Slight differences however, have significant effects on lattice energies and hence Gibbs energy and solubility products impeding direct quantitative transfer of data. Systematic trends in the actinide series allow interpolation of data and estimation of unknown solubility products. This may be useful as a first estimate for an underdetermined system but as a general approach for deriving solubility products, this method cannot be recommended. Experimental validation of the extrapolated solubility is in any case mandatory.

(2) Dissolved species and complexes

The hydrolysis and complex formation constants of metal ions having comparable electron configuration are correlated with respect to the strength of the electrostatic interaction energy $^{el}E_{M\text{-}L}$ between the metal ion and the negatively charged ligands [24-27]. The systematic decrease of the stepwise complex formation constant can be described by a relatively simple approach [28]. These systematic correlations allow estimates for uncertain experimental data for intermediate species or for estimation of unknown equilibrium constants. Given the uncertainty of extrapolated complex formation constants, experimental verification is therefore as well advised.

(3) Activity coefficients (Ion-ion interaction parameters)

The activity coefficient of an aquatic species is determined by its interactions with other ions in the solutions and with the water molecules (H_2O). For aquo-ions or complexes having the same charges and symmetries, slight differences in the ionic radii have negligible effects on the activity coefficients [16]. Consequently, the ion-ion interaction effects (or the coefficients of the SIT or Pitzer model) of these aqueous species can be set equal.

Geochemical model calculations allow a robust prediction of the main geochemical processes defining the geochemical boundary conditions in a repository. They also provide a powerful tool to model radionuclide solubility and speciation under a broad set of geochemical conditions. Both on the national (German THEREDA project) and international scale (e.g. NEA-TDB, IUPAC, …) the importance of supplying complete sets of reliable quality assured thermodynamic data as main input-parameter for model calculations has been realized. Despite these efforts, for aqueous systems at high ionic strength conditions, thermodynamic databases are rather incomplete with respect to thermodynamic data; especially adequate ionic strength corrections (activity coefficients) are often missing. Within this work on the radionuclide source term, predictions based upon measured solubility data are preferred against calculated data. The solubility limits derived in this study are based upon measured solubility data in well-defined reference systems. It should be understood, however, that for systems with good thermodynamic description available (like the carbonate free NaCl solutions considered within this study) a good agreement between geochemical model calculations and the measured solubility data is observed (cf. Fig. 23 and Fig. 24, Chapter 6.1).

2.2 Definitions and units

Actinide solubility and derived equilibrium constants are defined in literature partly in the molar concentration scale (c_i = mol i / Liter solution), partly in the molal concentration scale (m_i = mol i / kg H_2O). In the following, the radionuclide concentrations are given in the molar scale. Solubility is defined specifically for elements (not for the individual isotopes).

For all solubility data, a clearly defined thermodynamic definition of the pH is required. Details for concentrated salt solutions are given in ref. [29]. The pH is defined by the negative decadic logarithm of the chemical H^+ activity:

$$pH = - \log a_{H+} = - \log m_{H+} - \log \gamma_{H+}$$

In diluted solutions (I < 0.1) this definition is unambiguous, and after calibration of pH electrodes by standard pH buffers, the pH can be measured directly. In saline solutions several problems occur, for instance related to the conventions used to define activity coefficients. In addition, the combination pH electrodes used are equipped with diaphragms where diffusion potentials are formed. These diffusion potentials influence the measured potential systematically. As a consequence, the directly measured ”pH” in saline solutions is an operative experimental value (pH_{exp}) (without direct physical/chemical relevance) and has to be corrected as described below.

In contrast, the H^+ concentrations are well defined both in the molar scale (M, Mol H^+ per Liter) and in the molal concentration scale (m, Mol H^+ per kg H_2O). These values are determined from the op-

erative pH_{exp} values and an empirically determined parameter A which is specific for the matrix system.

- $\log M_{H+} = pH_{exp} + A_M$ (molar scale) = pH_c
- $\log m_{H+} = pH_{exp} + A_m$ (molal scale) = pH_m

By geochemical modeling, the molal H^+ concentration is calculated which can be recalculated to activities. This recalculation needs a convention with respect to the activity coefficients. The convention results in a pH (e.g. convention used in EQ3/6):

$pH_{(EQ3/6)} = - \log m_{H+} - \log \gamma_{H+(EQ3/6)}$

In this report, the definition $pH = pH_m = - \log m_{H+} = pH_{exp} + A_m$ (molal scale) is used for better readability.

3 Relevant data and processes

3.1 HLW glass

The following glass compositions are considered within this study:

- Minimum and maximum specification of the CSD-V glass returned from Areva's La Hague re-processing plant in France (labeled COGEMA)
- the inactive glass composition SON-68 (used in many experiments)
- an actinide doped glass CEA-R7T7
- a glass composition BNFL Blend 1 typical for the British Sellafield vitrification process
- glass formulations from the WAK high-level waste solidification in the VEK plant

An overview on the most important mechanisms and parameters regarding the performance of HLW glass is given in the following section.

Glass composition

Three classes of components can be differentiated in the glass structure: network formers, intermediates, and modifiers. The network formers (silicon, boron) build a highly cross-linked three-dimensional network of chemical bonds. The intermediates (titanium, aluminum, zirconium, beryllium, magnesium, zinc) can enter the network by substitution and act as network formers and modifiers, depending on the glass composition. The modifiers (calcium, lead, lithium, sodium, potassium) alter the network structure and are usually present as interstitial cations. Nearby non-bridging oxygen atoms, bound by one covalent bond to the glass network, hold one negative charge to compensate for the positive charge of the neighboring ions. The modifiers change the glass properties with respect to melting point or hydrolytic resistance. Lanthanide elements which are main constituents of the HLW act as network modifiers. Glasses need a well balanced composition of network formers, intermediates, and modifiers to prevent the formation of crystallites. An overview on the different relevant glass compositions is provided in the Appendix (Tab. A - 2).

The glasses listed in the appendix are all boro-silicate glasses having similar compositions. Experimental investigations using the simulated glass products SON 68 and GP WAK 1 did not reveal significant differences in their interactions with water or brines. For the inactive glass SON68, which simulates the active R7T7 reference waste glass, an extensive dataset of properties exists. Models were developed to explain the alteration behavior of this glass by formation of a gel layer and diffusion processes [2]. Application of the models to other glass compositions is questionable. Glass with a high alumina/silica ratio, for example, develops only very thin alteration layers, in which Si may, or may not be depleted. Hence, the concept of silica diffusion through the gel may not be applicable. The model of [2], which will be used for assessing the glass corrosion, has been tested and developed for WAK and COGEMA glass.

Evolution of glass alteration

The mechanism of glass dissolution is primarily driven by a number of processes that are schematically presented in Fig. 1. The two main reactions that are opposed to one another are the parallel reactions of “matrix dissolution” and “water diffusion / hydration of the glass matrix / ion exchange reactions”. The fastest process is the rate-dominating process in parallel reactions, whereas in sequential reactions, the slowest reaction governs the rate.

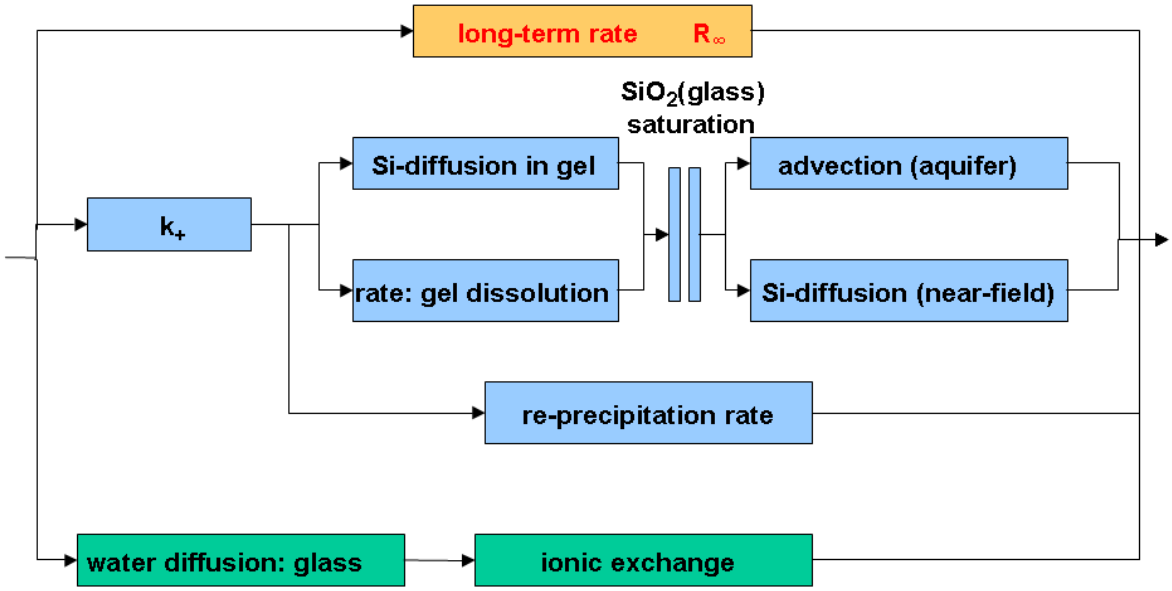

Fig. 1 Schematic drawing of the glass corrosion model according to [2]; the long-term rate is colored orange, matrix dissolution processes are shown in blue color and water diffusion / ion exchange reactions are marked with green color.

The combination of various mechanisms and processes lead to consecutive regimes of glass alteration (see Fig. 2):

1) Assuming instantaneous fill up with brine in case of container failure, the glass will corrode at the maximum (initial) rate.

2) However, if the permeable container is not completely or slowly filled with brine, as expected in the case of access of a limited brine volume, hydration by a vapor phase prior to the dissolution by liquid water might have to be considered. Vapor phase hydration is much slower than the initial rate.

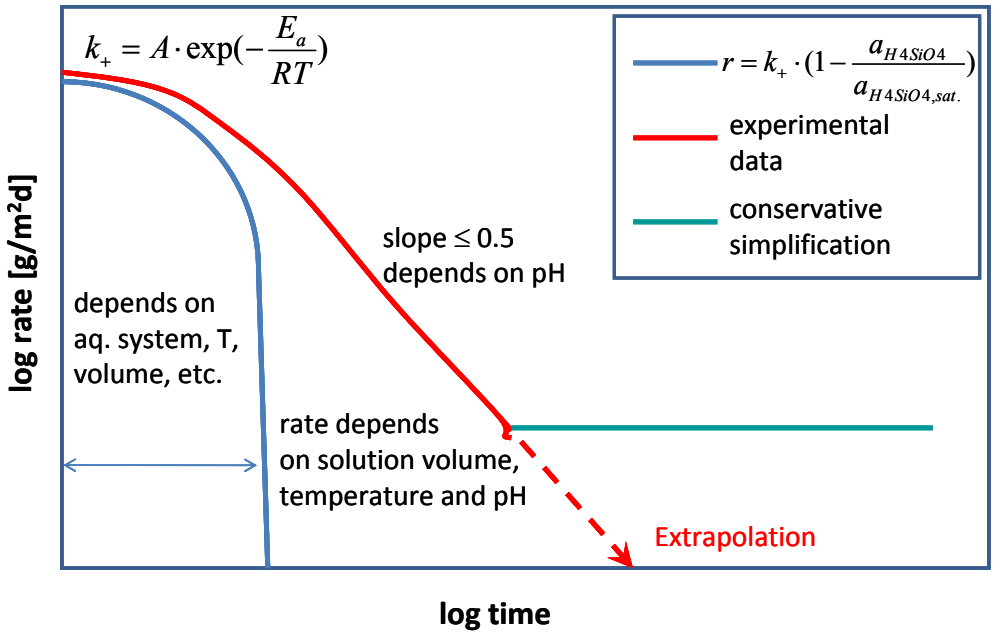

Fig. 2 Sketch of the different stages of HLW glass dissolution.

Due to the formation of the gel layers and/or the accumulation of glass constituents in solution, the glass corrosion rate decreases with time (see Fig. 2). The decrease will continue until a residual corrosion rate (long-term rate) is reached, which is not zero. Reasons may be the continuous removal of dissolved glass matrix constituents, and remaining diffusion processes [6]. The explanation of the dominating mechanism responsible for the finite long-term dissolution rate is an important remaining problem. As a result of secondary phase formation, the glass corrosion rate may under conditions discussed in [6], e.g. secondary phase formation leading to a detachment of the gel layer, increase again to values higher than the residual rate ('alteration resumption') [6].

Temperature of the near field

Temperatures up to 200 °C need to be considered for the disposal of HLW glass. Corrosion and leach test have been performed in salt brines up to 190 °C [3]. Temperature will have a significant influence on glass corrosion in a scenario with early brine intrusion. However, temperatures are assumed to decrease to ≤ 80 °C within the first 1000-5000 years. In the European project NF-Pro [6] the impact of the temperature of the near field on the glass source term is considered to be insignificant for a scenario, where the temperature is ≤ 50 °C when solution will contact the glass (after corrosion of the canister).

Radiolysis

In the scenarios considered in this report, the dominating γ-emitter ^{137}Cs has decayed, when the brine contacts the glass. The same is true for the dose dominating β emitting nuclides. Therefore, the impact of radiolysis on the HLW glass performance is insignificant (see also [30], "Stellungnahme Nr. 9"). For α-radiolysis, this was shown from experiments with the α-doped CEA-R7T7 simulate [3, 31].

Mechanical effects

Mechanical stresses caused by the cooling or by variation of the temperature field due to the radioactive decay [32] are important as far as they lead to breaking or fissuring of the glass. This increases

the surface area of the glass which may be exposed to the brine. From investigations of simulated glass blocks it was possible to obtain a realistic but conservative estimation of this surface area. R7T7 glass blocks are fractured inside the canister. The cracking is directly related to the temperature gradient between the core and outer surface of the glass block during cooling after the glass is poured and, to a lesser extent, to the thermal shock arising from decontamination of the package and to possible impacts during handling. The relation between the stress level and fracturing is difficult to quantify: it depends on the shape of the package as well as on any heterogeneity liable to redistribute stresses in the glass. The surface area, exposed to water can slightly increase with time, due to stresses, and chemically initiated fissure formation. Alternatively the accessible surface area may decrease due to cementation by formation of alteration products in the fissures, but these changes are neglected or included in the uncertainty of the surface area estimation.

Glass changes during storage

The HLW glass will be disposed after a certain interim storage period. Changes of the pristine glass prior to brine access are considered to have negligible effects on the barrier performance of the glass.

Glass alteration in absence of near field materials

The glass alteration after contact with brines in absence of near field materials has been investigated in various studies [3]. The applicability of this knowledge to systems including near field materials such as canister or backfill materials needs to be confirmed [6].

The glass alteration is considered to be very important, at least for the short and medium term of glass dissolution. On the long term, glass alteration may still be important, but the effect is then covered by the residual corrosion rate. So far, the long-term corrosion rate has been described only qualitatively but needs further investigation.

Radionuclide inventory of HLW glass

The glass composition is defined in WP 3 of the vSG project [15].

3.1.1 Temperature dependence of HLW glass dissolution

The influence of temperature on the long-term corrosion was investigated for the various HLW glasses (see Tab. A - 2 in the Appendix) in different salt solutions [30]. The temperature range was between 90 °C and 190 °C. Tests with R7T7 glass revealed that Si saturation concentrations (shown in Tab. I) are higher in NaCl solution than in $MgCl_2$ solution. The release of the highly soluble element Li behaves differently: up to 150 °C the release rates are the same for NaCl- and $MgCl_2$ solutions, however, for 190 °C, the release rate increases by a factor of 2 in the case of the $MgCl_2$ solution [33]. Li and B are used as indicators for matrix dissolution.

Tab. I shows the concentrations of Si in saturated NaCl and $MgCl_2$ solutions which were determined as a function of time for the temperature range between 110 °C to 190 °C and test durations of 18 to 40 months [34].

Tab. I Steady state silicon concentration [Si] released from HLW glass as function of temperature

Temperature	NaCl system measured [Si]	$MgCl_2$ system measured [Si]
110 °C	16.3 ± 2.8 ppm	12.8 ± 1.5 ppm
150 °C	41.3 ± 7.3 ppm	24.6 ± 1.6 ppm
190 °C	85.3 ± 20.1 ppm	49.1 ± 4.1 ppm

Fig. 3 shows that the final Si concentration in NaCl solution depends strongly on the temperature. However, for all three temperatures no significant variation with time was found.

The pH showed different behavior in the solutions: In NaCl solution pH was found between 6 and 8 for all temperatures, whereas in $MgCl_2$ systems the pH dropped to values between 6 and 5 [34].

Only for Li, a constant increase of the concentrations was observed (see Fig. 4). For Li, the rate (derived from the slope of the concentration) is 0.05 ppm day^{-1} for 110 °C, 0.12 ppm day^{-1} for 150 °C and increases to 0.25 ppm day^{-1} for 190 °C in NaCl and to 0.45 ppm day^{-1} in $MgCl_2$, respectively. The release of Li from the glass is controlled by diffusion with an Arrhenius temperature dependency of the diffusion coefficient.

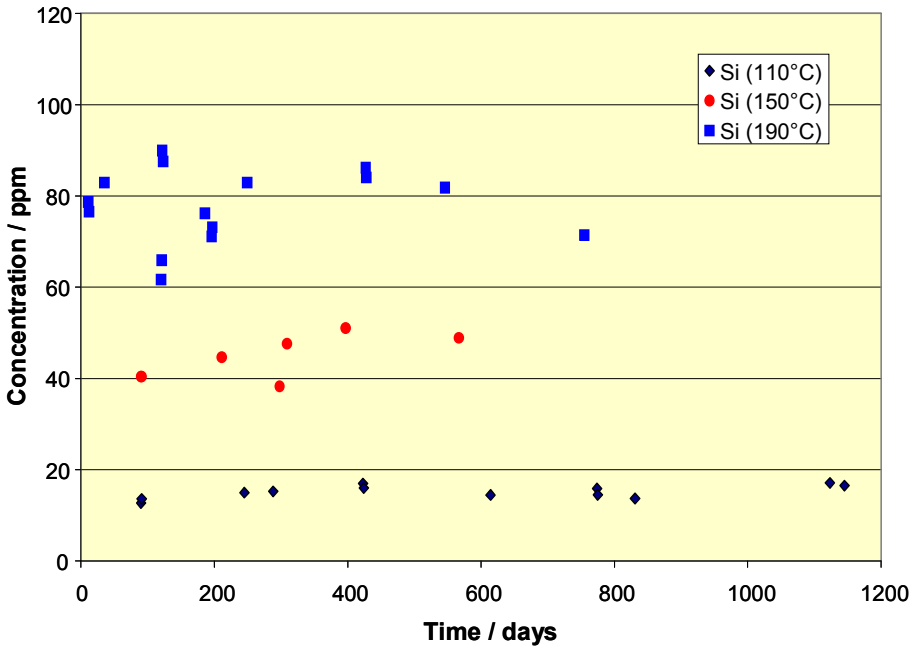

Fig. 3 Si concentration with time from corroding R7T7 glass in saturated NaCl solution.

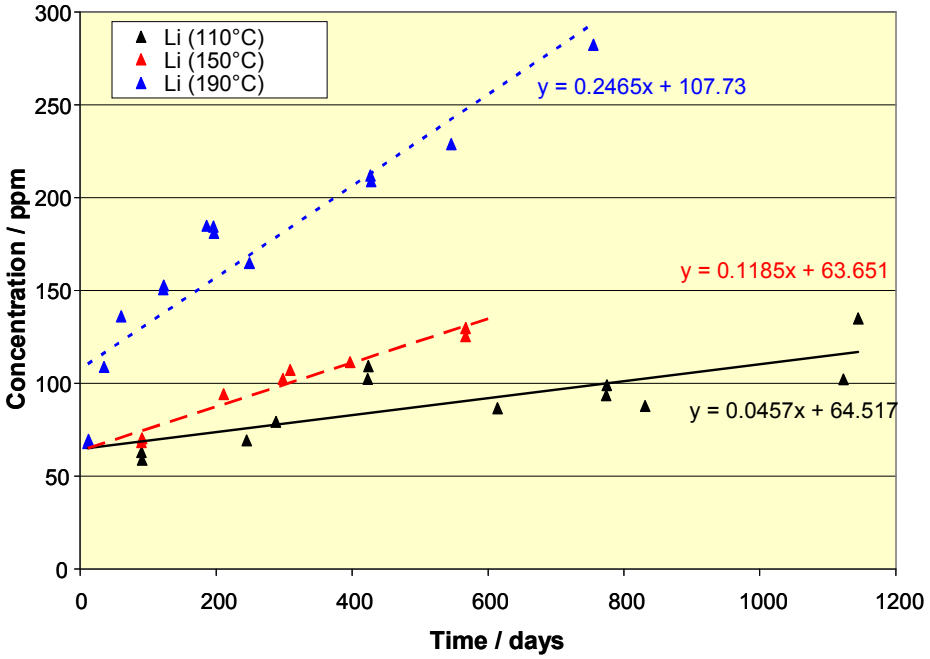

Fig. 4 Li concentration with time from corroding R7T7 glass in saturated NaCl solution.

3.1.2 Kinetics of HLW glass dissolution

Various glass corrosion models have been developed to quantify the release of glass constituents associated to either matrix dissolution or ion exchange. Within the present study the "Grambow model" [2, 5] is applied. The model describes the penetration of water into the glass network, which is assumed to be a prerequisite for both reactions. The penetration of water into the glass is described by an advection/dispersion/reaction equation. The hypothesis that the transport of H_2O molecules is rate limiting for the release of alkali ions and boron is a simplification. In reality, water inward-diffusion is expected to be coupled by an inter-diffusion process to the outward-diffusion of alkali ions and boron in a rather complex way, where each component flux depends on the gradients of all the components.

The model is based on the well known affinity/transition state theory-based interfacial reaction equation according to Aagaard and Helgeson [35].

$$r = \frac{d\xi}{s \cdot dt} = \vec{r} \cdot \left(1 - exp\left(\frac{-A_j}{RT} \right) \right) \qquad \text{eq. 1}$$

where ξ denotes reaction progress, s the effective surface area, A_j affinity $A_j = -RT\ ln(Q/K)$, R the gas constant, T the absolute temperature, Q the ion activity product and K the equilibrium constant of the dissolution reaction.

The saturation of the solution with regard to a silica end member plays a decisive role in slowing down glass corrosion rates and the rate law often takes the simple form of a first-order dissolution rate law characterized by a forward rate constant k_+ (unit: kg glass/(m^2 s)), the activity of dissolved silicic acid a_{Si} and a corresponding temperature-dependent saturation constant K_{SiO2} at the dissolving glass surface. The rate r of the corrosion reaction is given in simplified manner by

$$r_{shortterm\ rate}(T) = k_+ \cdot \left(1 - \frac{Q}{K(T)}\right) = k_+ \cdot \left(1 - \frac{a_{Si}}{K_{SiO_2}(T)}\right) \quad \text{eq. 2}$$

The temperature dependence of the rate constant k_+ is modeled by an Arrhenius law using the activation energy E_a:

$$k_+ = A \cdot exp\left(\frac{E_a}{RT}\right) \quad \text{eq. 3}$$

The reaction rate r is modeled by following equation under consideration of surface reactions and Si transport [36]:

$$r_{shortterm\ rate}(T) = k_+(T) \cdot \left(1 - \frac{k_+(T) \cdot FS \cdot \beta \cdot L + \phi \cdot D_{Si,aq}(T) \cdot \rho_{Lsg} \cdot m_{ccb}}{K_{SiO_2}(T) \cdot \phi \cdot D_{Si,aq}(T) \cdot \rho_{Lsg} + k_+(T) \cdot FS \cdot \beta \cdot L}\right) \quad \text{eq. 4}$$

where β is a factor for surface roughness, L is the distance from the surface, ϕ is porosity, $D_{Si,aq}$ is the diffusion coefficient for dissolved silicic acid, ρ is the solution density, m_{ccb} is the silicium concentration in the inflow and FS is a conversion factor FS = f_{Si} (1 - f_{prec})/MW_{SiO2} calculated from the Si fraction in the glass (f_{Si}), a factor quantifying the Si retention (e.g. by precipitation of secondary phases) and the molar mass of SiO_2 (MW_{SiO2}).

The term $k_+(T)$ can be derived by exponential fitting (unit: kg m^{-2} d^{-1}) to experimental data according to [8]:

$$r_{shortterm\ rate}(T) = 6.4 \cdot 10^6 \cdot exp\left(\frac{-8323}{T}\right) \quad \text{eq. 5}$$

For the long term dissolution rate, measured rates in water and salt solutions as function of the temperature are available [37], see Fig. 5. The long term rate can be fitted to the temperature T (in K) using an exponential equation (unit: kg m^{-2} d^{-1}):

$$r_{longterm\ rate}(T) = 5.6 \cdot 10^2 \cdot exp\left(\frac{-7397}{T}\right) \quad \text{eq. 6}$$

(R^2 = 0.8649)

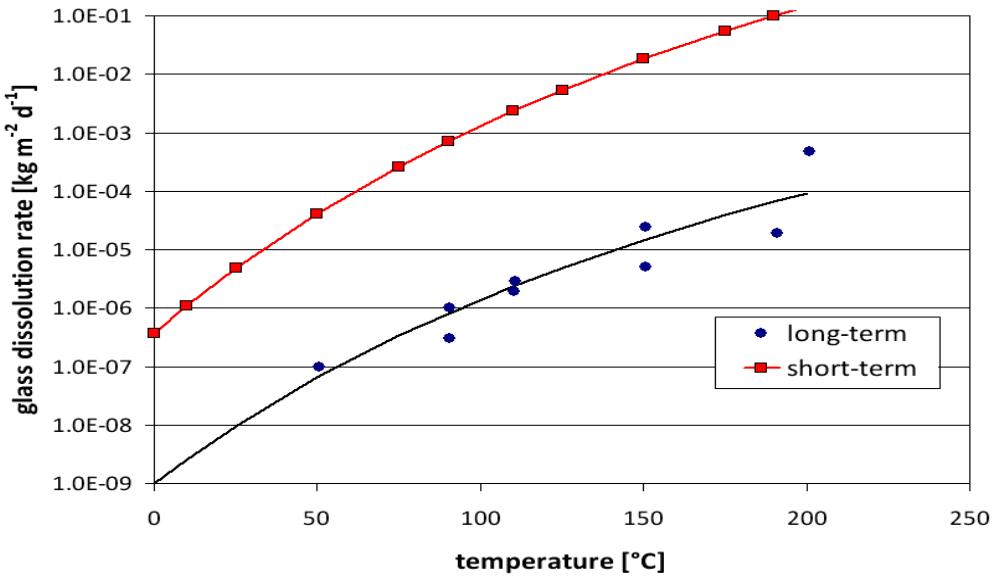

Fig. 5 Calculated short term (eq. 4) and experimental long term dissolution rates of HLW glass dissolution tests in salt solutions and water.

Before Si saturation is reached, the release rate of easily soluble elements e.g. boron from the glass matrix can be described similar to the release rate of Si. However, Si reacts at the surface of the corroding glass forming the gel layer. For this reason, the measured concentration of the easily soluble elements is always higher compared to the Si concentration. After Si saturation, the dissolution rate of the easily soluble elements decreases by several orders of magnitude by stabilization of the glass matrix due to Si saturation. Glass is not a thermodynamically stable phase. For this reason, the release of the easily soluble elements continues at a slow rate.

The mechanism of glass dissolution under Si saturation is not yet clear, possible mechanisms have been discussed in literature [38]:

1. solubility and kinetics of the formation of Si-rich secondary mineral phases
2. water diffusion and hydratation of the glass network and/or ion exchange
3. limitation of the Si transport rate through the corrosion/gel layer

The mobilization rate of easily soluble elements (such as Li, Na, Cs, B) from the HLW glass is described by the dissolution rate until Si saturation plus the long term dissolution rate (see Fig. 2).

$$r_{easily\ soluble\ elements} = r_{short\ term\ rate\ (Si)} + r_{\infty} \qquad \text{eq. 7}$$

3.2 Spent nuclear fuel from LWRs

Spent nuclear fuel consists of heterogeneous fractured ceramic UO_2 pellet contained in a cladding rod made from zirconium alloys. Spent nuclear fuel is characterized by a large variety of mixed phase assemblages, a complex distribution of actinides, fission products (FP) and distinct structural heterogeneities that results from the fuel's irradiation history, the neutronics and the initial composition of the fuel. In addition to radionuclides in the spent nuclear fuel itself, activation products are present in the cladding. Presently, spent nuclear fuels with typical burn-ups (35 to 45 MWd/kg U), contain about 95 wt. % of UO_2 (mainly ^{238}U, remaining ^{235}U and ^{236}U produced from ^{235}U by neutron capture;

e.g. [39]). Transuranium elements, fission and activation products occur in many different forms in the spent nuclear fuel. Kleykamp et al. (1985) [40] established a classification for the fission products, according to their chemical and mineralogical properties:

1. Fission gases and other volatile fission products (Kr, Xe, Br, I) which occur as finely dispersed bubbles within grains, at grain boundaries and in pores [41]; to some extent they are released to the open porosity of the fuel and gap.

2. Metallic fission products (Mo, Tc, Ru, Rh, Pd, Ag, Cd, In, Sn, Sb, Te) forming immiscible, micron- to nanometer-sized precipitates. The metallic phases found are ε-Ru(Mo, Tc, Rh, Pd) solid solutions (so-called ε-particles) with variable concentrations of the components, β-Mo(Tc, Ru) and α-Pd(Ru, Rh).

3. Fission products forming oxide precipitates (Rb, Cs, Ba, Sr, Zr, Nb, Mo, Te). These oxides tend to have the general composition $AB[O_3]$ and to adopt a cubic perovskite-type structure with Ba, Sr, and Cs in the A sites and Zr, Mo, U and lanthanides (Ln) in the B sites [40, 42].

4. Fission products occurring as oxides in the UO_2 fuel matrix (Sr, Zr, Nb, Y, and the lanthanides La, Ce, Pr, Pm, Sm). Zr and rare earth elements are partially or completely miscible with UO_2 to form a solid solution [43].

There are continuous transitions between the four groups, which depend on the burn-up and consequently on the chemical state and solubilities of the fission products [44]. For example, prominent Sr and Zr isotopes occur in the dominating ceramic precipitate $(Ba_{1-x-y}Sr_xCs_y)(U,Pu,Ln,Zr,Mo)O_3$ as well as solid solutions in the UO_2 matrix. Similarly to lanthanides, transuranium elements (Pu, Am, Cm, Np) occur in the UO_2 matrix, where they substitute U.

In their review, Bruno and Ewing [39] describe that the distribution of radionuclides is not homogeneous within a single pellet because of the steep thermal gradient within the pellet (temperature above 1000 °C at the centre of the pellet and decreasing to few hundreds degrees Celsius at its rim). Thermal excursion during reactor operation cause a coarsening of the grain size, extensive microfracturing and migration of fission gases and volatile fission products to grain boundaries, fractures, and the "gap" between the edge of the fuel pellet and the surrounding metal cladding. Due to a gradient in the burn-up with relatively high burn-ups at the pellet periphery, porous and fine grained microstructure "high burn-up structures" are formed. These high burn-up structures are characterized by relatively high concentrations of ^{239}Pu at the fuel rim, polygonization of the UO_2 grains resulting in a reduction in the size of individual grains [43]. According to the classification of Kleykamp [40, 44], Johnson et al. [45] and Poinssot et al. [46], radionuclides are spatially distributed among

(i) the gap region,

(ii) grain boundaries,

(iii) UO_2 grains / the UO_2 fuel matrix and

(iv) the high burn-up structures / the rim region,

which is depicted in Fig. 6.

Assuming the presence of aqueous solution in the near field as well as breaching of fuel canisters and fuel rods, the alteration of the spent nuclear fuel and the consecutive release of radionuclides involves the combination of many different processes, which can be grouped into two stages (e.g. [39]):

- Fast release of radionuclides at the time of waste package failure. The fast released radionuclide fraction is generally referred to as the Instant Release Fraction (IRF)
- A much slower, long-term radionuclide release that results from the alteration and dissolution of the UO_2 fuel matrix.

The IRF concerns a fraction of few percent principally of ^{135}Cs, ^{129}I and possibly ^{79}Se, ^{99}Tc, ^{107}Pd. Radionuclides in structural metal parts of the fuel elements and in the fuel cladding are often also considered as contributing to the IRF.

With regard to the long-term radionuclide release, the decrease in the radiation dose rate with time will lead in the long term to a situation where radiolysis effects are negligible. Whether or not radiolysis effects are detrimental to spent nuclear fuel stability depends to a large extent on the time when the fuel canister will fail. In case of canister breaching at a stage, when the spent nuclear fuel inventory is in the range of several tens to 10000s of GBq/(kg HM), the UO_2 matrix dissolution and radionuclide release will be governed by radiolytically enhanced processes. Considering presence of aqueous solution and breaching of the fuel canister after several 10000 years (when relatively low inventories remain; see Fig. 7), chemically driven matrix dissolution and radionuclide release will occur. The main processes affecting alteration of the spent nuclear fuel and the consecutive release of radionuclides are depicted schematically in Fig. 8.

Spent nuclear fuel alteration processes and radionuclide release processes depend on many spatially and temporal varying geochemical parameters. In the following, the definition of an alteration progress indicator and fuel properties defined by the burn-up and radiolytic processes in salt brines are described. The relevance of the canister concept and disposal concept for the alteration processes and radionuclide release processes is also discussed.

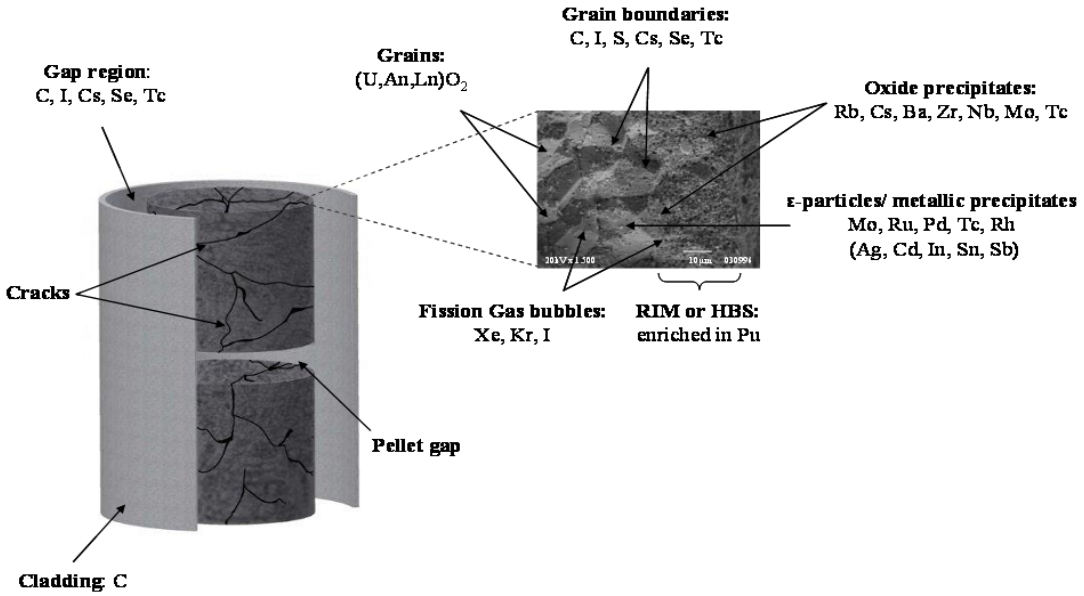

Fig. 6 Schematic illustration of the microstructure of cladded spent nuclear fuel and the distribution of actinides, fission and activation products [43].

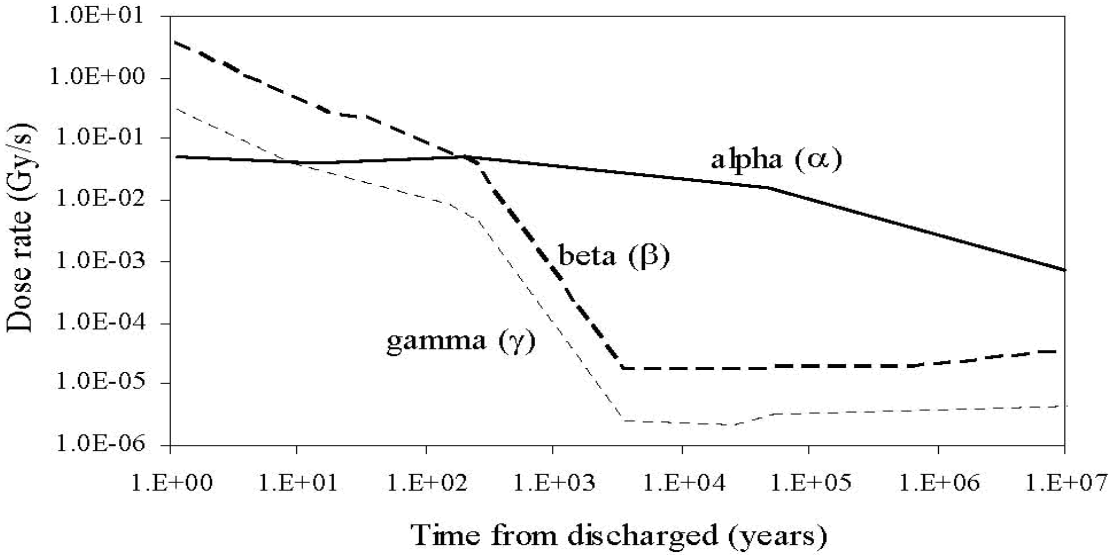

Fig. 7 Calculated α-, β- and γ-dose rate as a function of time after discharge from the reactor for a UO_2 spent nuclear fuel with a burn-up of 60 (MWd/kgU) ([43] based on data of [47])

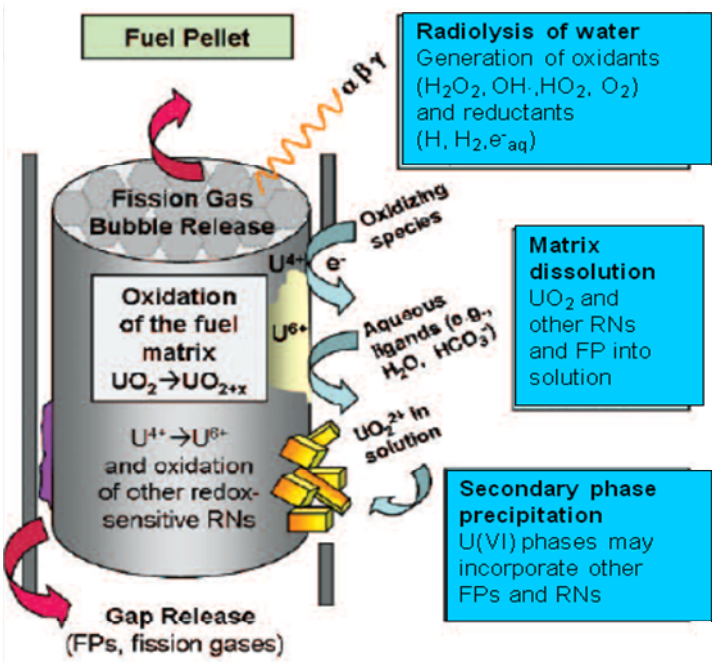

Fig. 8 Schematic illustration of the fundamental processes governing the alteration of spent nuclear fuel (modified after [39]).

Definition of an indicator for spent nuclear fuel matrix dissolution and "FIAP" definition

The main component of spent nuclear fuel is tetravalent uranium as UO_2. Its solubility is very low, and it was confirmed that redox reactions, interactions with groundwater components and corrosion products as well as the formation of secondary phases control the observed uranium concentrations in the solutions. For this reason, attempts have been made to identify a fission product which could

be used as indicator for the UO_2 matrix dissolution. This fission product should be dissolved congruently with U (when U is significantly undersaturated with respect to secondary U phases), should occur as oxide in the UO_2 fuel matrix, should not show accumulations in the rim and gap, should not be redox sensitive, should be scarcely involved in sorption processes and should be readily soluble in the considered aqueous system.

Spent nuclear fuel corrosion experiments in diluted and saline solutions showed that ^{90}Sr and U release rates were rather similar, as long as the U concentration was significantly undersaturated with respect to secondary U phases [33, 48, 49]. Thus, it was concluded that the ^{90}Sr release can be used as indicator for the dissolution of the UO_2 matrix. Most experimental studies on alteration of the spent nuclear fuel matrix in brines were derived from static tests which followed a leaching of the rapidly released radionuclide fraction including a minor portion of the ^{90}Sr inventory. After the release of the ^{90}Sr inventory attributed to the instant release fraction, the ^{90}Sr release was thought to reflect the dissolution of the UO_2 matrix and be useable as matrix indicator. However, the UO_2 matrix dissolution rate is mostly lower than the ^{90}Sr release rate because most of the dissolved U is rapidly re-precipitated again as secondary phases [9].

The dimensionless term *Fraction of Inventory in the Aqueous Phase,* FIAP, of an element was introduced [50] to relate the dissolved concentration of a radionuclide to its concentration in the spent nuclear fuel. Regarding the Sr release from spent nuclear fuel, $FIAP_{Sr}$ (or "Sr-FIAP") is calculated according to eq. 8 with index i for Sr:

$$FIAP = \frac{[conc]_i \cdot V_{solution}}{H_i \cdot m_{spent\ fuel}} = \frac{m_{i,aq}}{m_{i(spent\ fuel)}} \qquad \text{eq. 8}$$

where $[conc]_i$ is the concentration of i in solution ($g \cdot mL^{-1}$), $V_{solution}$ is the volume of solution (mL), H_i corresponds to the fraction of inventory for i (g/g), $m_{spent\ fuel}$ is the mass of the spent nuclear fuel sample (g), $m_{i,aq}$ is the mass of i in the aqueous phase (g) and $m_{i(spent\ fuel)}$ is the mass of i in the spent nuclear fuel sample (g).

Burn-up and fission yield

Upon irradiation in the reactor core, the nuclear fuel changes its properties, e.g. chemical composition, radionuclide inventory and pellet structure. At a burn-up of 52 MWd/kg HM (heavy metal), the concentration of fission products reaches ~5.4 wt. % in an enriched uranium fuel (UOX) and ~5.2 wt. % in a mixed-oxide fuel (MOX). Details can be found in textbooks on radiochemistry of nuclear fuel / power plants [14, 51].

According to Neeb [14], the disintegration of the heavy nuclides in the neutron-induced fission reaction results in an asymmetric mass division process with a lighter and a heavier fragment. Mass distribution can be expressed by the fission yields. For ^{235}U fission, the heavy fragment is located around mass number 138, while the lighter fragment is distributed around mass number 95, with fission yields of about 7 % each. In between the two peaks, mass distribution curves for fission products show a minimum with fission yields on the order of 0.01 %. For fission of ^{239}Pu, the distribution curves have a similar shape but peaks of the mass fragments are shifted towards mass numbers 99 and 140. In both fission curves, a certain fine structure can be observed close to mass number 133,

which originates from the preferential formation of fission fragments with the magic neutron numbers 50 and 82 in the nucleus (i.e. saturated neutron shells).

A total kinetic energy of 167 MeV is distributed between the two fragments according to the reciprocal ratio of their masses, which causes the fragments to move in opposite directions (~10µm recoil length) affecting the crystalline properties of the spent nuclear fuel. The major amount of kinetic energy (~95 %) is converted into electronic stopping power, while a minor amount is expended in atomic collisions causing lattice effects. Around the fragment path, a displacement field of cylindrical symmetry is usually observed (spur) with a diameter of 10nm and a length of ~6µm. The UO_2 lattice is affected by the high-speed movement of the fragments causing an intense ionization of the fragments and high local temperatures (~3000 °C) within a diameter of around 10 nm. Among the effects of the fission fragments are lattice defects caused by the knocking out of atoms from their regular positions, radiation-induced creep and fission-induced densification of the UO_2 matrix and re-dissolution of small fission gas bubbles [14].

In order to describe the relevant radionuclide mobilization / retention processes and to provide data for a preliminary radionuclide source term, averaging is applied:

- An enrichment of 4 % ^{235}U and a burn-up of 50 GWd/t HM is assumed
- It is not distinguished between BWR and PWR spent nuclear fuel.
- Homogeneous burn-up over the length of the fuel elements / rod is assumed.

The inventory of some radionuclides in the spent nuclear fuel is given in the WP 3 report [15] and Tab. II.

A series of technical impurities in the spent nuclear fuels (given in [15]) are listed in Tab. III. The impurities are related to the production process of the fuel. Significant is the nitrogen content in the range of 30 ppm which is considered as an upper limit by the fuel producer ANF in Lingen, Germany in UO_2 fuel.

Tab. II Inventories of selected fission products in spent nuclear fuel [15].

Element	DWR UO_2 55 GWd/t	DWR MOX 55 GWd/t
Se	86.9	64.8
Sr	1424.0	757.3
Y	744.0	394.1
Zr	5795.0	4136.0
Mo	5424.0	4995.0
Tc	1266.0	1282.0
Ru	4176.0	5101.0
Rh	647.4	1090.0
Pd	2273.0	4071.0
I	339.0	459.8
Cs	4616.0	5378.0
Ba	2467.0	2365.0
La	2012.0	1887.0

Element	DWR UO_2 55 GWd/t	DWR MOX 55 GWd/t
Ce	4370.0	3910.0
Nd	6221.0	5440.0
Eu	273.0	370.3

Tab. III Technical impurities in the spent nuclear fuel caused by the production process (WP 3 report, [15]).

Element	Concentration [ppm]	**Element**	Concentration [ppm]
F	4	**Na**	5
H_2O	2	**Pb**	5
Bor	0.5	**Sn**	5
Fe	15	**V**	5
Si	6	**Zn**	5
Ni	3.5	**Ti**	5
N	30	**Th**	5
C	4	**Ta**	5
Cl	4.5	**P**	5
Ca	10	**W**	5
Ag	5	**Li**	1
Bi	5	**Al**	21
Co	5	**K**	10
Cu	5	**Cr**	3
Mg	5	**Mn**	1
Mo	5		

Radiolysis of salt brines

Radiolysis of salt brines in the near field of spent nuclear fuel is highly important with regard to radiation induced matrix dissolution and radionuclide release. Radiolytic decomposition of aqueous solutions is accompanied by the formation of redox agents. With respect to radiolysis in salt brines, H_2 molecules are the main reductants, whereas radiolytic oxidants are dominated by oxo-halogenides, such as HClO (both for high and low linear energy transfer (LET) radiation), OH^- (for high LET) and Cl_2^- (for low LET) [52]. Since most oxidizing radiolysis products are more reactive than the radiolysis product H_2, the relatively stable UO_2(s) matrix of spent nuclear fuel may be oxidized into the much more soluble U(VI), as long as concentrations of inhibitors such as H_2 are sufficiently low [39, 53, 54]. However, high hydrogen concentrations will be achieved in the near field of the fuel, mainly caused by anaerobic corrosion of the Fe-based waste canisters. The effect of hydrogen on the radiolytic yield of long-lived products in concentrated NaCl solutions was measured by means of γ-radiolysis [55-57]. These γ-irradiation experiments under hydrogen pressure showed a decrease in the radiolytic production of H_2 and O_2 but still a remarkable yield of chlorate compared to experiments conducted without hydrogen. Various research studies have been dedicated to examine the influence of molecular hydrogen on the radiolysis of pure water, diluted aqueous solutions and NaCl rich solutions ([58] and references therein). To the present knowledge, a single reaction accounts for the influence

of molecular hydrogen on radiolysis of aqueous solution ($^{\bullet}OH + H_2 = H_2O + H^{\bullet}$). Ultimately, this reaction converts oxidizing $^{\bullet}OH$ radicals into reducing $H^{\bullet}$ radicals.

The radiolysis of highly concentrated NaCl and $MgCl_2$ solutions was investigated by several authors, e.g. [58, 59]. Using pulse radiolysis it was found that the Cl_2^- radical anions are formed in acidic solutions. In neutral or slightly alkaline solutions radical anions Cl_2^- were observed only in concentrated solutions (> 0.1M Cl^-). The yield of different radiolytic products formed by γ-radiolysis from NaCl brines at ambient temperature and dose rates between 0.1 and 1 kGy/h were determined [59, 60]. In concentrated NaCl both H_2, O_2 and ClO_3^- were formed proportionally to the dose and independently from the dose rate with radiation-chemical yields of 0.6, 0.16 and 0.074 molecules per 100 eV, respectively. An extended kinetic model for the chloride system which includes the formation of chlorate was used to simulate the experimental results [52].

Though bromide is a minor constituent in brine, it is present in a concentration range relevant for radiolytic processes, i.e. up to 10^{-1} mol (kg H_2O)$^{-1}$ [61-63] Results of α- and γ-radiolysis experiments in NaCl brine demonstrate (i) it is not the major constituent Cl^-, but the presence of Br^- traces that dominates formation of radiolytic species, and (ii) Br^- concentrations of 10^{-4} to 10^{-3} mol (kg H_2O)$^{-1}$ considerably promote radiolytic decomposition, even at 10^{-2} mol H_2 (kg H_2O)$^{-1}$ [55-57]. In a pulse-radiolysis study, Ershov et al. (2002) [64] investigated the interaction of bromide and chloride ions in concentrated NaCl-NaBr solutions. They determined the production of a broad range of molecular (Cl_2, ClBr, Br_2) and ionic (Cl_3^-, Cl_2Br^-, $ClBr_2^-$, Br_3^-) radiolysis products. The hydrolysis of ClBr, Br_2 results in the formation of hypobromite HOBr. Hypobromite is the starting substance for the formation of more stable bromates of higher oxidation state.

Disposal concept

A disposal concept for spent nuclear fuel, the so called "direct disposal of spent nuclear fuel" was developed in the vSG project [65] and will be optimized within WP 6. Disposal concepts have been developed for different emplacement options. Option B is split into two alternatives for disposal of heat-generating waste: In option B1 the use of POLLUX casks is considered for final disposal, while option B2 covers the transport, storage and final disposal in CASTOR casks. In emplacement option C, the disposal of heat-generating waste in vertical boreholes is considered [(2)].

The POLLUX canister consists of a shielding cask with a screwed lid and an inner cask with bolted primary and welded secondary lid. The inner cask consists of fine-grained steel 15 MnNi 6.3, the thickness of the cylindrical wall is 160 mm according to the mechanical and shielding requirements. The outer cask provides shielding. Its thickness is 265 mm and it consists of cast iron GGG 40. The weight of the inner cask (including spent nuclear fuel is 31 Mg, the weight of the outer cask is 34 Mg. 10 complete fuel elements can be packed into a POLLUX cask. Another possibility is the accommodation of consolidated fuel rods (5.4 tHM). For Gorleben, disposal of POLLUX casks in horizontal galleries is foreseen at distances of several meters between the galleries (15 m - 36 m) and between each cask (1 m - 5 m). Afterwards, the galleries should be backfilled using crushed rock salt.

[(2)] *Option A* comprises the horizontal disposal of waste with negligible heat generation.

Disposal concept C considers the emplacement in vertical boreholes. At present, it remains to be demonstrated that retrievability of the wastes can be achieved for the disposal in vertical boreholes as it is requested by the safety requirements [1]. Within this concept, the spent fuel will be packed into BSK 3 casks. The BSK 3 cask was designed for accommodation of consolidated fuel rods. The outer shape of this cask corresponds to the HLW canisters of the COGEMA type, which are packed into a so-called “triple pack” of three canisters. This fact would allow mixed disposal of spent fuel and vitrified waste. The capacity of a BSK 3 is designed for three PWR fuel elements or 9 BWR fuel elements. The wall thickness of the BSK 3 is 50 mm, sufficient to keep the mechanical forces resulting from the convergence of the rock salt.

In both types of casks, inner baskets are applied holding the fuel elements or fuel rods. The basket will be composed of stainless steel (1.4541) coated with borated steel sheets (1 wt. % B) and copper.

The POLLUX casks will be stored in horizontal galleries; BSK 3 casks in vertical drill holes. The characteristics of the 2 disposal concepts are given in Table I. Relations between potentially contacting water (solution) and iron or Fuel are listed. The table shows, that within the disposal galleries or drill holes only a minor amount of water would be available to corrode the casks or fuel.

Tab. IV Characteristic data of the POLLUX and BSK 3 disposal concepts for spent fuel [65] and calculated ratios of inventory to solution.

		POLLUX concept	**BSK 3 concept**
Number of fuel rods per cask		3000	900
external diameter d_a		156 cm	43 cm
inner diameter d_i		69 cm	35 cm
Length of the canister		552 cm	498 cm
Mass of steel per cask		57 Mg	2.9 Mg
Mass of polyethylene per cask		1540 kg	7 kg
drift/drill hole cross-section area		17 m^2	0.3 m^2
Void volume gallery per cask (without backfill)		140 m^3	0.85 m^3
Backfill porosity (t = 500 yrs.)		10 %	10 %
		PWR / BWR	PWR / BWR
mass ratios in kg/L	fuel (U) / solution	0.4	19.1 / 19.8
	steel / solution	4.1	34.1
mol ratios in mol/L	U / water	1.6 / 1.7	80.4 / 83.2
	Fe / water	73.0	610.9

3.2.1 Spent nuclear fuel dissolution

The alteration rate of the spent nuclear fuel matrix depends on the surface area. Uncertainties in measured surface area of spent nuclear fuel samples are very large, up to 5 orders of magnitude for a given constant specific geometric surface area [13]. However, there exists no proportionality in the relationship between the measured surface area and the spent nuclear fuel dissolution rate. Hanson and Stout [50] observed a decrease in dissolution rates, while surface area increases upon long term

leaching. Due to the high uncertainties in specific surface areas of SNF samples, radionuclide release rates and SNF dissolution rates are given generally in FIAP per day; in some cases surface normalized dissolution (e.g. in units mg m^{-2} d^{-1}) are estimated.

3.2.1.1 Instant release fraction

Within the European projects SFS (5th Framework Programme) and MICADO (6th Framework Programme), the IRF concept was revised and defined as the radionuclide inventory located within microstructures with low confinement properties: the fuel plenum, gap zone, fracture surfaces, the rim zone with high-burn up structures and grain boundaries [13]. The fast/instant release processes depend on spent fuel properties, including those caused by the manufacturing process, in-reactor fuel operating parameters such as linear power rating, burn-up, linear power, fuel temperature, ramping processes, and interim storage time. The IRF at a given time is defined as the sum of the short term release of the radionuclide inventory in the gap interface between the cladding and the pellet, the fractures (released in weeks) and also to grain boundaries (released during months). In experiments with high burn-up SNF samples it is observed that the IRF contribution from the gap between the spent nuclear fuel and the Zircaloy cladding is about one order of magnitude larger than the IRF contribution from the fuel grain boundaries. The least IRF contribution originates from internal grain boundaries [43]. A comprehensive review of published IRF data derived from leaching experiments was carried out during the SFS project by Johnson et al. (2004) [66]. An updated IRF assessment lowered the estimated IRF significantly [67, 68].

The initial distribution of radionuclides between the various microstructures is not completely understood, in particular for high burn-up and MOX fuels. This is particularly the case of highly mobile elements like ^{36}Cl. In static and dynamic leaching experiments with high burn-up SNF samples, González-Robles [43] determined an inhibitive influence of the high burn-up structure on the IRF. This structure is characterized by a relatively high surface area on one side and a high fission product content, which reduces the UO_2 matrix dissolution on the other side. In this study the predominance of the inhibiting effect of the fission products on the UO_2 matrix dissolution and consequently the protective effect of the high burn-up structure on the radionuclide release were demonstrated.

3.2.1.2 Matrix dissolution

Since the SNF activity decreases with time due to the radioactive decay, it is important to relate the rate of the radiation induced SNF matrix dissolution to the residual activity. Most studies on the effect of activity on SNF matrix dissolution kinetics focus on “old” spent nuclear fuel, which is dominated by α-emitters (e.g. [69-78]). Poinssot and coworkers reviewed the large experimental dataset and drew the following major conclusions on the SNF matrix dissolution kinetics [46, 68]):

- Spent nuclear fuel alteration rates decrease with decreasing α-activity except for the lowest α-activities for which the rate seems to be controlled by solubility of uranium phases and to be independent of the α-activity.

- A specific activity threshold occurs below which the α-radiation induced matrix dissolution is negligible.

Transition of radiation induced to solubility controlled matrix dissolution

The effective dose threshold is a purely empirical measurement of the competition between oxidants production and subsequent matrix alteration on the one hand, and the consumption of oxidants by the other aqueous ions on the other hand. As a consequence, the activity threshold depends on the geochemical environment. Based on experiments in deionized water, it has been estimated to be in the range 18 - 33 MBq g^{-1}. This α-activity range corresponds to spent nuclear fuel ages between 3500 and 55000 yrs (see Fig. 9 and Fig. 10) depending on the fuel types: between 4.5 ky and 15 ky for a 60 GWd/t UOX fuel, and between 42 ky and 55 ky for a 60 GWd/t MOX fuel. The α activity of a typical spent fuel from Biblis NPP (4 % initial enrichment, 50 GWd/t_{HM}) is shown in Fig. 10. The threshold, when α radiolysis will no longer contribute to the matrix dissolution is reached after several thousands of years. The contribution of γ radiation becomes negligible after some hundreds of years.

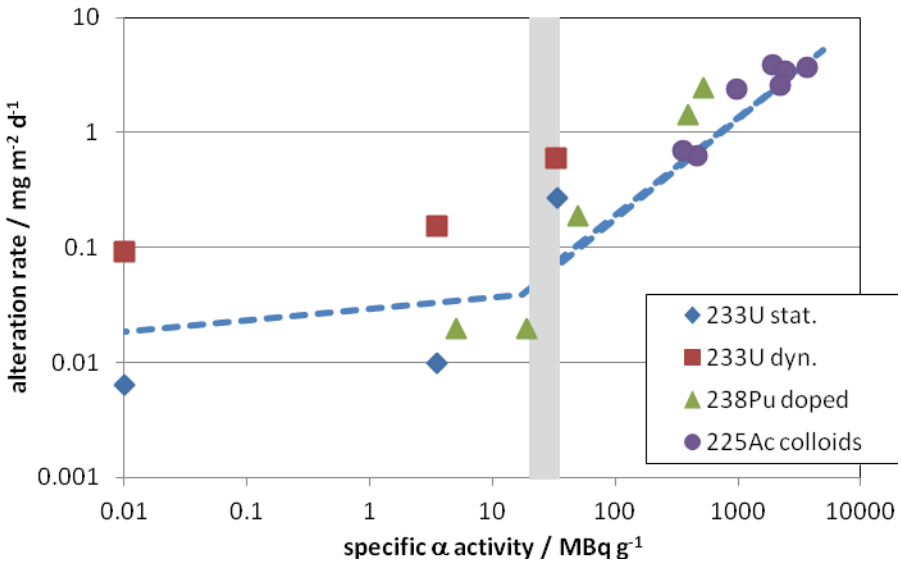

Fig. 9 Dissolution rates of α-doped UO_2 samples as function of specific α-activity (taken from [68]).

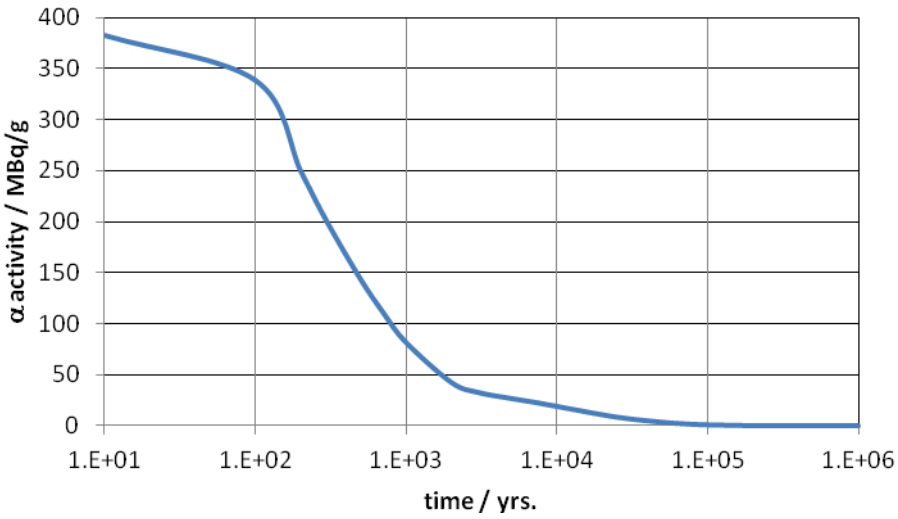

[79]

Fig. 10 Specific α-activity of a typical Biblis reactor fuel (initial 4 % ^{235}U, 50 GWD/t_{HM}).

Hydrogen effect

Radiation induced SNF matrix dissolution can only occur if the non-radiolytic redox couples in the near field do not consume the radiolytic oxidants. Since high hydrogen concentrations will be achieved in the near field of the fuel, mainly caused by anaerobic corrosion of the Fe-based waste canisters, a strong inhibition of the SNF matrix dissolution is expected. Leaching experiments with spent nuclear fuel and UO_2(s) as well as radiolysis studies indicate that molecular hydrogen both impedes radiolytic decomposition of the diluted and saline solution and considerably inhibits corrosion of the UO_2(s) matrix [53-55, 58, 70, 80-87]. Still, there is insufficient knowledge about the molecular mechanisms of the protective hydrogen effect on SNF corrosion [57, 84]. A recent international benchmark study on modeling of spent nuclear fuel corrosion shows that model uncertainties are still very large, especially regarding the effect of hydrogen as well as the respective parameters of the radiolytic reactions [88]. This hydrogen effect, without being well understood, is considered in the SKB's and Posiva's safety analyses [89].

Fig. 11 shows the dissolution rate as a function of hydrogen gas pressure at constant dose rate as it is used in the SKB SR 97 spent nuclear fuel alteration/dissolution model [89] under the influence of near field hydrogen. The curves show variations of the base case obtained by assuming a significantly lower α-dose rate (factor 100), a higher reaction rate between oxygen molecules and uranium dioxide (by a factor 10), and a higher reaction rate between hydrogen peroxide and uranium dioxide (by a factor 10). The variations reveal that for all cases at hydrogen pressures >0.45 MPa the dissolution rates of spent nuclear fuel as a function of hydrogen gas pressure is below 10^{-7} FIAP per year. Complete dissolution would require 10 million years.

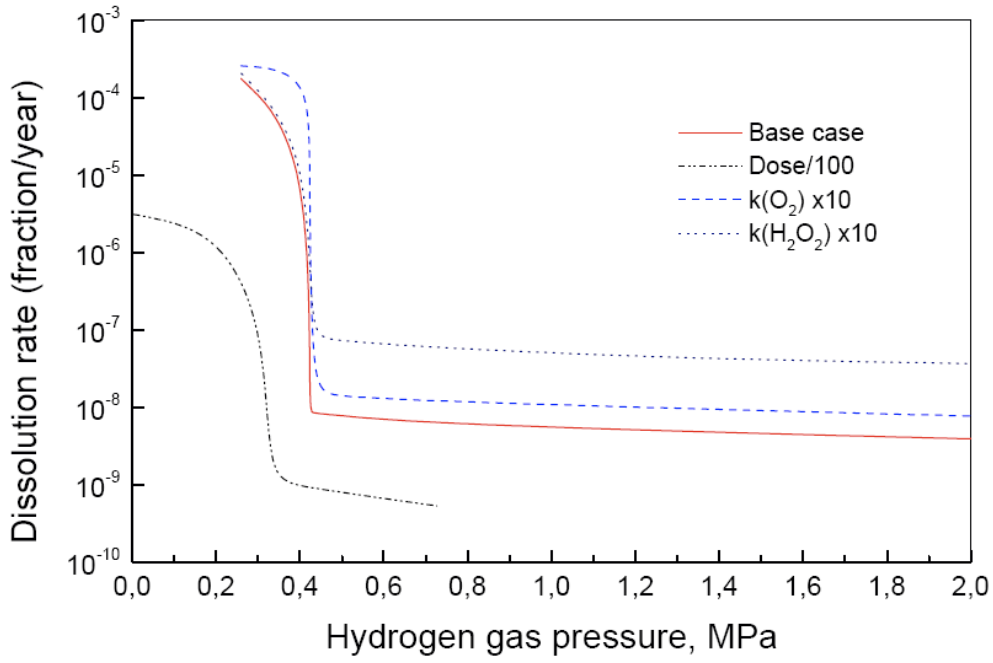

Fig. 11 Dissolution rate as a function of hydrogen gas pressure at constant dose rate for SKB's SR 97 spent nuclear fuel alteration/dissolution model under the influence of near field hydrogen [89].

The inhibition effect of hydrogen on radiation induced dissolution of the SNF matrix was observed in leaching experiments with UO_2(s) and SNF samples in groundwater simulates. These groundwater simulates contain only few constituents, mainly Na^+, Cl^- and HCO_3^-/CO_3^{2-}. Bromide is a minor con-

stituent in groundwater of deep geological formations. Nevertheless, it is present in a concentration range relevant for radiolytic processes, i.e. up to 10^{-3} mol (kg H_2O)$^{-1}$ in granitic groundwater (e.g. [90, 91]), up to 10^{-4} mol (kg H_2O)$^{-1}$ in argillaceous pore-water (e.g. [92]) and up to 10^{-1} mol (kg H_2O)$^{-1}$ in salt brines from deep salt formations [61-63].

In recent experimental studies, SNF dissolution and γ-radiation induced UO_2(s) dissolution were studied at elevated hydrogen pressure in NaCl brine containing 10^{-4} and 10^{-3} mol Br^- (kg H_2O)$^{-1}$ [56, 57]. Both, in the γ-radiolysis experiment with Br^- and without Br^-, the UO_2(s) sample was oxidized, and the concentration of dissolved uranium controlled by precipitation of secondary U(VI) phases. In the spent nuclear fuel dissolution experiment measured U concentrations were between solubilities of U(VI) and U(IV) phases. The release rate of Sr was significantly increased in the presence of Br^- traces. Results of the spent nuclear fuel corrosion and γ-radiolysis experiments allow the conclusion that Br^- traces reduce significantly the protective hydrogen effect with respect to the release of certain radionuclides and the yield of radiolytic products.

3.2.1.3 Modeling of the spent nuclear fuel dissolution rate

A conceptual IRF model has been developed attributing the rapid radionuclide release to the various microstructures present within the fuel pellet within the European SFS project (5th FWP). The fast / instant release fraction is defined as the sum of two terms: The first term represents the fraction of radionuclides rapidly released by fresh irradiated fuels. The second term takes into account any evolution of the inventory availability prior to the arrival of water in the spent nuclear fuel rod [13]. IRF values of the first term are based on the correlation between fission gas release (FGR) during irradiation and leaching data available in literature. A detailed description of effects relevant for FGR a modeling procedures are given in the Ph.D. thesis of Blair (2008) [93]. Modeling procedures for athermal diffusion and displacement processes of labile fission products are described by Lewis and Sills (1991) [94] and Wise (1988) [95]. Still, the various processes governing the IRF are insufficiently integrated into modeling of the gas release on the different microstructures of the spent fuel pellet, the pellet gap, defects in cladding material. Similarly, modeling of correlations between the gas release fraction and the fast release of non-gaseous fission products are characterized by considerable uncertainties. The forthcoming European FIRST-Nuclides project (7th Framework Programme) aims to couple experimental results with model development and the impact of different experimental findings on the refinement of fast / instant release prediction capability.

The so-called Matrix Alteration Model (MAM) was developed during the European SFS project [96-98]. The Matrix Alteration Model includes (i) modeling of the generation of oxidants and reductants by a kinetic radiolysis model of radiolysis (ii) oxidation of the spent nuclear fuel surface, (iii) reduction of (molecular) aqueous oxidants and (iv) dissolution of spent nuclear fuel matrix and radionuclides release according to the uranium speciation and groundwater composition with or without consideration of electrochemical processes. The Matrix Alteration Model is schematically illustrated in Fig. 8. In the past years, this model approach was continuously improved (see European projects SFS [99], MICADO [13], [100]). MAM allows predicting the matrix alteration rate of the spent nuclear fuel pellet with a defined geometry under different environmental conditions. There are still some processes not considered by the model, such as influence of radiolytically produced radicals, effects of minor groundwater constituents, formation of secondary phases, etc.

3.2.2 Temperature effects

3.2.2.1 Temperature dependence of radiolytic reactions

Many reactions involved in radiolysis of diluted and concentrated aqueous solutions are well known at ambient temperature. Regarding radiolysis of pure water and water containing few trace components, rate constants, activation energies, and G-values at elevated temperatures have been determined for several reactions of importance for predicting steady-state concentrations of radicals and products during operation of nuclear reactors (e.g. [101-123]). Regarding radiolysis in pure water, a database of G-values (Tab. V), rate constants and activation energies was compiled by Christensen et al. [124]. Reported activation energies of the radiolytic reactions are in the range of 8 - 80 kJ mol^{-1}. There are only very few experimental studies dealing with the temperature influence on radiolytic reactions in chlorine / chloride rich solutions (e.g. [55, 123]).

Summarizing the temperature dependencies of the various elementary radiolysis reactions would be out of scope of this documentation of the present scientific knowledge on the behavior of heat-generating waste under saline conditions. Instead, selected studies are mentioned to exemplify temperature effects on radiolysis of aqueous solution. The concentration of the hydroxyl radical, $OH^{\bullet}$, is critical for the evolution of radiolytic chain reaction and consecutive UO_2(s) / spent nuclear fuel corrosion reaction. For instance, the inhibiting effect of molecular hydrogen on radiolysis of water is controlled by a reaction with the hydroxyl radical ($OH^{\bullet} + H_2 = H^{\bullet} + H_2O$). Elliot and McCracken [108] showed that the pKa for the hydroxyl radical drops by 1.03 units in the temperature range 20 to 80 °C. The activation energy (19 kJ mol^{-1}) and rate constants at 20 and 230 °C ($3.4^{\bullet}10^7$ and $7.7^{\bullet}10^8$ dm^3 mol^{-1} s^{-1}, respectively) of this reaction were determined by Christensen and Sehested [106]. In the range of 10 to 120 °C, the temperature effect on the reaction of H_2O_2, the dominant oxidative radiolysis product at high LET radiation, with hydrogen radicals was studied by [108, 113, 117, 122]. The rate constant of reaction $H^{\bullet} + H_2O_2 = OH^{\bullet} + H_2O$ increases from $4.4^{\bullet}10^7$ dm^3 mol^{-1} s^{-1} at 10 °C to $1.5^{\bullet}10^8$ dm^3 mol^{-1} s^{-1} at 120 °C. The activation energy was found to be 10.7 kJ mol^{-1} [113]. Kelm and Bohnert [55] determined the production of long-lived radiolysis products at 35 °C and 90 °C in concentrated NaCl solution under γ-irradiation. In contrast to their γ-radiolysis experiments at 35 °C, no significant production of gaseous radiolysis products (H_2, O_2) and strongly inhibited production of ClO_3^- were observed at 90 °C.

Tab. V G-values of primary γ–radiolysis products (molecules/100 eV) and their change with temperature [125].

	25 °C	dG/dT	40 °C	90 °C
H^+, OH^-	0.1	3.27E-03	0.15	0.31
H	3.55	4.62E-03	3.61	3.85
H_2	0.4	5.77E-04	0.41	0.44
OH	2.83	6.54E-03	2.93	3.25
H_2O_2	0.76	-3.85E-04	0.75	0.74
H_2O	-4.45		-4.58	-5.04

3.2.2.2 Temperature dependence of spent nuclear fuel corrosion

In most projects on experimental determination of radionuclide release from spent nuclear fuel and SNF corrosion, the quantitative assessment is limited to room temperature. In particular, in the concepts of the European 5th and 6th FWP projects, influence on SNF behavior at elevated temperatures are considered as less relevant, because groundwater access to the spent nuclear fuel in a "thermal phase" was assumed to be excluded by the stability of the container (e.g. [13]). Thus, documentation and discussion of the temperature dependence of spent nuclear fuel corrosion is very limited because only very few experimental data are available. To our knowledge, all experimental studies on the temperature dependency of UO_2(s) corrosion and spent nuclear fuel corrosion have been conducted solely under oxic or anaerobic conditions (e.g. [9, 33, 126-128]. The temperature effect on the instant / fast release fraction, the UO_2(s) matrix dissolution rate and the consecutive radionuclide release has not yet been properly understood.

Regarding the release of radionuclides from the SNF matrix, a minor influence of temperature on these processes is observed [9]. De Pablo et al. [126, 127] studied the (non-radiolytic) solubility controlled dissolution of UO_2(s) at 10, 25, 45, and 60 °C. They observed an increase in the dissolution rate by almost two orders of magnitude when increasing the temperature from 10 to 60 °C in presence of carbonate and depending on pH. Published studies on corrosion of irradiated UO_2 / spent nuclear fuel show contradictory results of moderate temperature effects [9]. For leaching of CANDU fuel in granite water, an increase in the corrosion rate by a factor of 10 – 20 was observed as the temperature was raised from 25 to 150 °C [9, 129]). However, corrosion of high burn-up spent nuclear fuel in salt brines in the same temperature range even showed a decrease [33, 130]. Using various fuels, Karsten, Loida and co-workers studied SNF corrosion under anaerobic conditions (N_2 atmosphere) in $MgCl_2$-rich solution (Q-brine) at 25, 90, 100 and 150 °C and in concentrated NaCl solution at 100 and 150 °C [130, 131]. Both under strongly acidic conditions and under near neutral pH conditions they determined after several months the lowest FIAP values at 150 °C. This observation is illustrated with a comparison of FIAP values measured in experiments "AL 20/5" conducted at 90 ° C and "AL 23/5" conducted at 150 °C (Fig. 12). In contrast, an increase in initial FIAP values with increasing temperature was determined in corrosion experiments with medium burn-up (36.6 and 50.4 MWd/(kg HM) and high burn-up (52.3 MWd/(kg HM)) in $MgCl_2$-rich and concentrated NaCl solution [130]. For example, the fast / instant release fraction of ^{137}Cs increased by a factor of up to 2.5 when the temperature increased from 100 to 200 °C [132, 133].

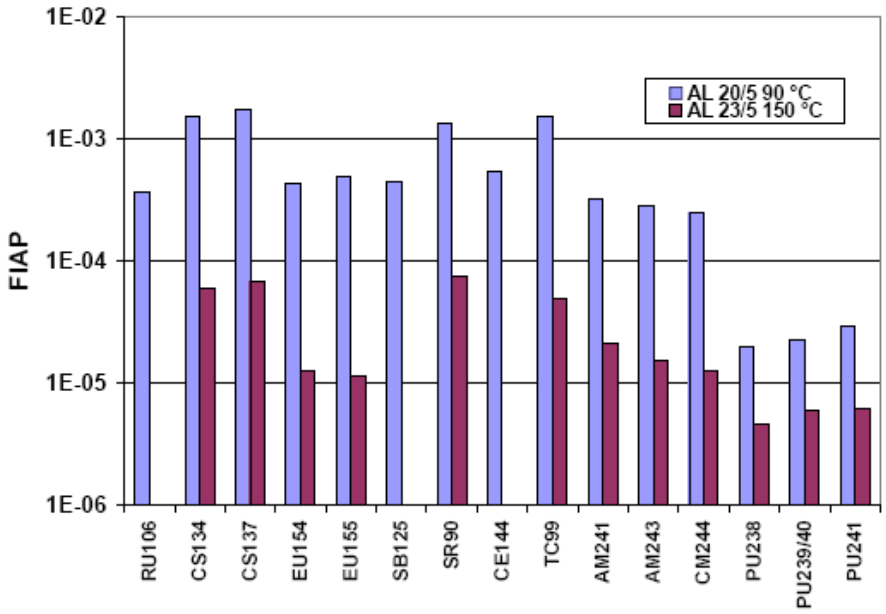

Fig. 12 Effect of temperature on the release of radionuclides from fuel with a 52.3 MWd/(kg HM) burn-up in $MgCl_2$-rich solution at 90 °C (AL 20/5) and 150 °C (AL 23/5) [130]. FIAP values in AL 20/5 were measured after 226 days at pH_{exp} = 6.5 and FIAP values in AL 23/5 were measured after 263 days at pH_{exp} = 5.8.

3.3 Compacted hulls, end pieces and spacers (CSD-C waste)

A survey of properties of the compacted solid radioactive wastes in standard canisters (Colis Standard des Déchets Compactés, CSD-C) and the related radionuclide source term is given in this chapter. CSD-C wastes were produced in the Atelier de Compactage des Coques (ACC) in La Hague, France and will be transferred to Germany. In the present concept, the CSD-C consist of zircaloy rod pieces (hulls) and end pieces from PWR and BWR fuel elements as well as the spacers (Fig. 13). These materials are filled into 90 l cartridges, dried (540 ppmV) with nitrogen at 200 °C to remove all free liquid and supercompacted using a pressure of 200 MPa. The process is described in details by Chotin [134]. Discs are produced by supercompaction, and 5 to 7 of such discs are stored in a standard waste canister. The interior of a simulated test canister is shown in Fig. 14.

Fig. 13 Compaction of hulls and end-caps from spent nuclear fuel assemblies [135]

A list of guaranty parameters is agreed upon by AREVA and Germany:

β/γ - activity	**α - activity**
65 TBq for ^{137}Cs	3.3 TBq for Pu
115 TBq for ^{90}Sr/^{90}Y	2.0 TBq for ^{244}Cm
75 TBq for ^{241}Pu	4.2 TBq for nuclides with half-life > 50 yrs.
β/γ - contamination	**α - contamination**
4.0 Bq cm^{-2}	0.4 Bq cm^{-2}
Other parameters	
Dose rate: < 150 Gy/h	
Thermal power < 90 W	
Weight < 850 kg	

During the operation of the German WAK pilot reprocessing plant, hulls and end pieces were at low priority with respect to conditioning and waste management. In total, 3 publications exist [136-138] on this issue. One publication is available dealing with (super-) compaction of hulls and end pieces [139]. Unpublished reports (so-called Primärberichte) covered the same spectrum of investigations [140-154].

Fig. 14 Supercompacted hull and end pieces discs stored in a standard canister [135].

Disposal concept

In disposal option B1, it is foreseen to dispose of the 4.104 canisters of CSD-C waste in 456 specially-designed POLLUX casks in horizontal galleries. Disposal option B2 considers the disposal of the CSD-C wastes in 114 TGC36 containers.

3.3.1 RN-Inventory and composition of the CSD-C waste forms

Initial composition of the materials

Zircaloy (Zry), a zirconium alloy with various metallic constituents, is commonly used as the fuel rod cladding material. While in BWRs Zircaloy-2 (Zry-2) is the preferred cladding material, PWRs use Zircaloy-4 (Zry-4); the compositions of both alloys are shown in the following Tab. VI. The mass of Zircaloy in German PWRs amounts to about 290 kg/Mg HM (heavy metal), in BWRs to about 320 kg/Mg HM (including the fuel assembly channels) [14].

The structural materials consist of 13 kg/t HM Inconel with 7 - 18 wt. % Fe and < 2000 ppm Co. The end pieces consist also of Inconel with a mass of 42 kg/tHM [15]. Inconel is a trademark and refers to a group of austenitic nickel-chromium-based alloys. Inconel alloys are typically used in high temperature applications. According to [14], different types of Inconel are used, which are separated from the UO_2 fuel and compacted during reprocessing. Their composition is given in Tab. VII.

Tab. VI Composition of Zircaloy [14]

	Zircaloy-2	**Zircaloy-4**	**M5^{TM} [155] [3]**	**Zr-1Nb [155] [3]**
Zn	bal.	bal.	bal.	bal.
Sn	1.2 -1.7 wt. %	1.2 – 1.7 wt. %		< 30 ppm
Nb	-	-	1	1
Fe	0.07 – 0.2 wt. %	0.18 – 0.24 wt. %	237 ppm	570 ppm
Cr	0.05 – 0.15 wt. %	0.07 – 0.13 wt. %	32 ppm	-
Ni	0.03 – 0.08 wt. %	-		
O	0.07 – 0.15 wt. %	0.10 – 0.16 wt. %		
Traces				
Al	75 ppm	75 ppm		
B	0.5 ppm	0.5 ppm		
Cd	0.5 ppm	0.5 ppm		
C	270 ppm	270 ppm		
Co	20 ppm	20 ppm		
Cu	50 ppm	50 ppm		
Hf	100 ppm	100 ppm		
H	25 ppm	25 ppm		
Mg	20 ppm	20 ppm		
Mn	50 ppm	50 ppm		
Mo	50 ppm	50 ppm		
Ni	-	70 ppm		
N	65 ppm	65 ppm		
Si	120 ppm	120 ppm		
S			30 ppm	
Ti	50 ppm	50 ppm		
U	3.5 ppm	3.5 ppm		
W	100 ppm	100 ppm		

[3] The compositions of M5^{TM} and Zr-1Nb are obtained from specific samples, trace element concentrations have not been found.

Tab. VII Composition of Inconel (http://asm.matweb.com)

	Inconel 625	Inconel 718
Nickel	min. 58.00	50.0-55.0
Chromium	20.0 - 23.0	17.0-21.0
Iron	max. 5.00	balance
Molybdenum	8.0 - 10.0	2.8 - 3.3
Niobium	3.15-4.15	4.75 - 5.5
Cobalt	max. 1.00	1.00
Manganese	max. 0.50	max. 0.35
Copper	-	max. 0.3
Aluminum	max. 0.40	0.2 – 0.8
Titanium	max. 0.40	0.65 – 1.15
Silicon	max. 0.50	max. 0.35
Carbon	max. 0.10	max. 0.08
Sulfur	max. 0.015	max. 0.015
Phosphorus	max. 0.015	max. 0.015
Boron	-	max. 0.006
Density	8.44 g cm^{-3}	8.19 g cm^{-3}

In the WWER PWRs, the cladding material Zr-1Nb (Zr 99 %, Nb 1 %) is used [51]. The data listed in Tab. VI and Tab. VII are in agreement with the compositions reported in the WP 3 report [15].

3.3.2 Reactions during neutron irradiation in a nuclear reactor

Activation reactions

The activation of major or trace elements in the irradiated materials can be calculated by the equation of activation [156]:

$$A(t) = \frac{m \cdot H \cdot N_A \cdot \sigma \cdot \Theta}{M} \cdot (1 - e^{-\lambda t}) \qquad \text{eq. 9}$$

A(t):	Activity (Bq)	m:	mass (g)
σ:	cross section (barn = cm^2)	Θ:	neutron flux ($n \cdot cm^{-2} \cdot s^{-1}$)
M:	atomic mass (g)	H:	isotopic abundance (-)
N_A:	Avogadro's number	λ:	decay constant (s^{-1})
t:	irradiation time (s)		

The number of activated atoms is calculated by dividing the activity in eq. 9 by the decay constant. It is obvious from eq. 9 that the number of long-lived activated atoms depends on the cross section for neutron capture, the neutron flux and the irradiation time.

Eq. 9 is applied on the formation of ^{14}C by the reaction ^{14}N (n,p) ^{14}C reaction. The cross section for this reaction is 1.93×10^{-24} cm^2, a typical neutron flux 10^{13} $cm^{-2} \cdot s^{-1}$. Nitrogen concentration of zircaloy amounts to 65 ppm. After 3 years of irradiation in such a neutron flux, the total ^{14}C activity amounts to 2×10^4 Bq/kg .

Alteration of the Zircaloy cladding

During reactor operation, surfaces of the cladding become covered by oxide layers. Onto the inner Zircaloy surface, a layer of ~25µm is formed, which contains up to 0.2 % oxygen compared to about 0.1 % in the Zircaloy bulk material. This oxygen originates from the oxide fuel; however, it does not significantly affect the stoichiometry of the fuel. The inner oxide layer contains fission products transported there mainly due to fission recoil. In addition, interaction zones between the cladding oxide and fuel are observed occasionally which are usually locally limited and tightly adherent to the cladding material.

The cladding is in contact with high-temperature water or steam on the outside. The PWR rods show a rather homogeneous black oxide layer, the thickness of which depends on the period of exposure as well as on the thermo-hydraulic design of the fuel assembly. The maximum thickness is generally observed in the upper third of the fuel rod length, amounting to about 60 to 100 µm. On BWR rods, normally a very thin oxide layer of a few µm only is observed; in addition, nodular corrosion occasionally occurs with zones reaching a thickness up to 100 µm. Additionally, local oxide layers can be present which are generated by chemical action of the coolant and affected by the material properties of Zircaloy-2. At design burn-up, these local oxide layers reach a maximum thickness of about 25 µm (see above) - by change in the fabrication technology of the material their extent has been significantly reduced. Examples of the maximum oxide layer thickness as function of the average fuel burn-up is shown in Fig. 15 for different cladding materials Zyr-4 and M5 [157].

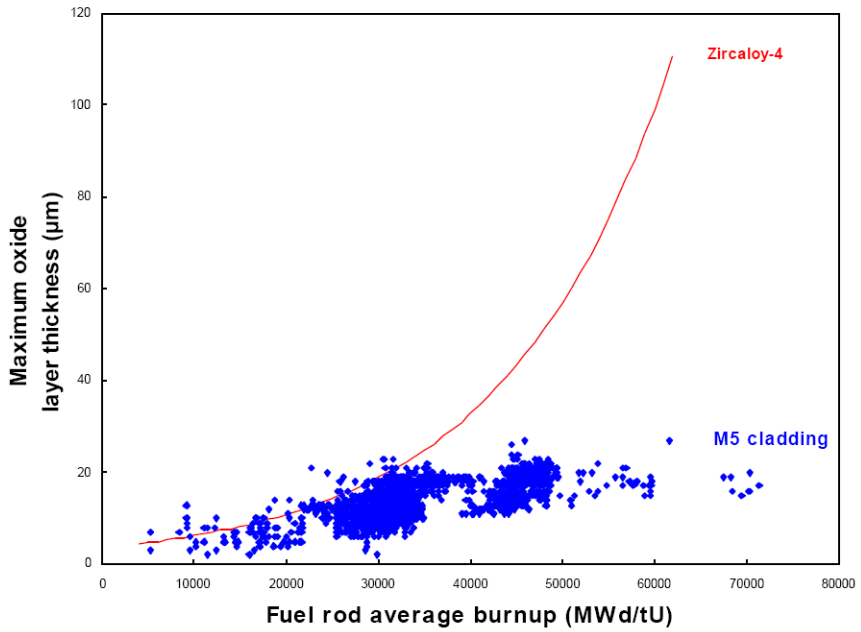

Fig. 15 Maximum oxide layer thickness as function of the average fuel burn-up [157].

Additionally, layers consisting of Fe, Co, Ni corrosion products may be present on the outer surface of the zircaloy rods. Important activation reactions are listed in Tab. VIII.

Tab. VIII Important activation reactions for long-lived RNs

Reaction	Main source
$^{14}N(n,p)\ ^{14}C$	Zircaloy. water, fuel
$^{98}Mo(n,\gamma) \xrightarrow{\beta} {}^{99}Tc$	Steel
$^{94}Zr(n,\gamma)\ ^{95}Zr \xrightarrow{\beta} {}^{95}Nb$	Zircaloy
$^{124}Sn(n,\gamma)\ ^{125}Sn \xrightarrow{\beta} {}^{125}Sb$	Zircaloy

The dominant radioactivity comes from the neutron activation products of the zirconium base material, namely ^{95}Zr and its daughter product ^{95}Nb. Calculated with ORIGEN, Neeb [14] reports ^{95}Zr activity concentration in the claddings (discharge) to about 500 MBq/g. ^{125}Sb is generated with an activity concentration on the order of 5MBq/g from the tin contained in both Zircaloy-2 and -4. However, the calculated values yield ^{125}Sb activity concentrations that are by a factor of 7 to 20 lower than those of investigations in the context of spent nuclear fuel reprocessing. This might be an effect of redeposition of ^{125}Sb during the leaching of the fuel. An essential contribution to the cladding total activity comes from ^{60}Co a neutron activation product of cobalt traces present in the material. According to the trace impurity content of the material, the ^{60}Co activity concentration varies between 0.7 and 15 MBq/g Zry. Frequently, uranium traces contained in Zircaloy trigger the formation of transuranium isotopes in the cladding during reactor operation. Cladding concentrations of ^{239}Pu in the range 20 to 100 Bq/g, in addition to 20 to 50 Bq ^{240}Pu/g, 7 to 10 kBq ^{241}Pu/g and 40 to 120 Bq ^{241}Am/g have been reported from investigations performed in the context of reprocessing [14]. By means of nondestructive determination of residual fuel on leached hulls, Würz [158] measured in 28 batches of PWR hulls the remaining Pu_{tot} in the waste. It could be shown that up to 0.5 % resulting in 37 g Pu_{tot} left on the hulls per ton of reprocessed heavy metal. The mean value was about 0.3 % or about 24 g Pu_{tot}/tHM.

Other effects may also contribute to the total contamination of fuel hulls. Beside diffusion processes from the fuel to the inner rod surfaces, “knock-out” of FPs may occur. The initial kinetic energy of a FP is dissipated by electronic interactions with the material over a distance of approx. 10 µm from the FP's formation. If the fission fragment is created sufficiently close to the fuel surface (i.e. <6 to 7 µm) the fission fragment can be directly released to the surfaces of the UOX/MOX grains [93].

Due to fuel swelling and cladding creep, fuel and cladding come into close contact under the conditions of operating temperature and pressure. Locally, small fuel particles may stick to the cladding material, resulting in fuel residues at the inner cladding surface in post-operational cold conditions. In addition, the inner cladding surface of fuel rods exhibits high linear heat ratings and show layers covering narrowly limited areas across from pellet cracks. They contain uranium, cesium and tellurium.

An estimation of the production of ^{14}C in LWR was presented by Bleier et al., 1987 [159]: In the gas plenum of the studied fuel elements of PWR and BWR a negligible concentration of ^{14}C was found. In BWR waste, the ^{14}C concentration of spent nuclear fuel (22000 MWd/t) was 7000 Bq/g UO_2, and the ^{14}C concentration of the cladding was 22600 Bq/g zircaloy-2. In spent nuclear fuel of a 30000 MWd/t PWR a ^{14}C concentration of 9300 Bq/g UO_2 was determined. PWR cladding was not investigated. A correlation of the ^{14}C production with the burn-up was obtained as 370 - 390 GBq ^{14}C per (GWe yr).

Alteration of the structural materials

According to Neeb [14], the fuel assembly spacer grids are fabricated either of Inconel or of Zircaloy materials, depending on fuel assembly type and manufacturer. While the central grids are located in the region of maximum neutron flux, the upper and the lower grids are in the region of decreasing flux; for this reason, the activity inventories of the individual grids depend on their position in the fuel assembly.

Neeb [14] states: *"The nuclides ^{55}Fe and ^{63}Ni (activation products of the alloy main constituents) predominate, in addition to ^{60}Co resulting from cobalt impurities. At a fuel burnup of 32.7 MWd/kg U, their activity concentrations in the central grids are on the order of 3 GBq/g each, decreasing to about 1 GBq/g in the bottom and top spacer grids. Compared with these nuclides, ^{59}Ni and ^{54}Mn only play a minor role. ^{94}Nb, the (n,γ) activation product of the alloy constituent niobium (nominal value about 4 %), shows activity concentrations in the central grids on the order of 4 MBq/g. It is surpassed by far by ^{93m}Nb, which is generated by an (n,n') reaction produced by fast neutrons (threshold energy 0.5 MeV) from stable ^{93}Nb, mainly because of its much shorter half-life (13.6 yrs. vs. 2×10^4 yrs.). … In Zircaloy spacer grids, ^{55}Fe and ^{125}Sb are the main radionuclides, with ^{125}Sb being produced from the alloy constituent tin (1-2%) by the reaction ^{124}Sn (n,y) $^{125}Sn \xrightarrow{\beta^-} {}^{125}Sb$. After a fuel burnup of 41.8 MWd/kg U, their activity concentrations in the central grids amount to about 0.1 GBq/g each. The other long-lived radionuclides such as ^{60}Co, ^{63}Ni and others show activity concentrations which are lower by two to five orders of magnitude."*

3.3.3 Reactions during head-end treatment of the materials

During reprocessing, the fuel rods are chopped into pieces of ~3-4 cm and then sent to a continuous rotary dissolver with boiling nitric acid. Under these conditions, the fuel and most of the adhering layers are dissolved and sorbed radionuclides are de-sorbed. After reprocessing and dissolution of spent nuclear fuel in concentrated HNO_3 more than 99.0 % of ^{14}C was found in $^{14}CO_2$. The remaining ^{14}C content was bound to various compounds, such as ^{14}CO, $^{14}CH_4$ [14].

3.3.4 Measurements on CSD-C waste

The hull material are parts (~ 35 mm length) from the fuel rods consisting of zircaloy-2 (from BWR) and zircaloy-4 (from PWR). In the final waste form, the radionuclides cannot be determined directly, for this reason γ-activity is measured and the other RN are determined by correlations. Measured isotopes in Fig. 16 are framed in red, while the other nuclides are calculated.

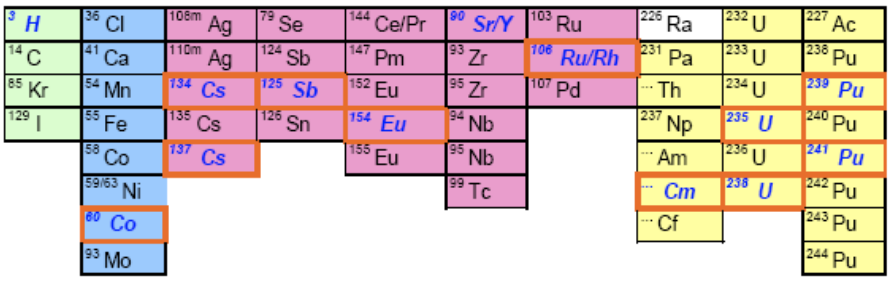

Fig. 16 Relevant radionuclides and determination procedures

Radiolysis

CSD-C waste is contaminated only with small amounts of α-emitters. Radiolytical impact is higher by orders of magnitude during the irradiation in a reactor and/or during the storage of un-reprocessed spent nuclear fuel. For this reason, radiolysis is not expected to cause changes of the material properties.

Mechanical effects

Zircaloy is sensitive against hydrogen embrittlement. Hydrogen may be formed by corrosion of steel canisters. Significant partial pressures can arise (> 10 MPa). Under such conditions, H_2 penetrates into the crystalline structure of zircaloy and changes the ductility of the material. It is unknown whether hydrogen embrittlement results in increased corrosion rates.

4 Boundary Conditions

In the “Preliminary Safety Analyses for Gorleben“, the development of the disposal concept, the FEP catalogue and the related scenario analysis are performed in parallel to this study. Therefore, the radionuclide source term has to cover a wide range of conditions and evolutions which may be narrowed in a final disposal concept and scenario development. For the purpose of this documentation of the present scientific knowledge on the behavior of heat-generating waste under saline conditions, the definition of the scenario and geochemical boundary conditions are highly simplified in this study. Only concentrated NaCl and $MgCl_2$ solutions are considered within this simplified scenario; more complex brine compositions are discussed in [30]. The initial pH_m is in the range $6< pH_m <9$ and the temperature is below 200 °C (temperature maximum at surface between canister and crushed salt backfill [65]).

4.1 High-level waste glass

The considered evolution scenario for HLW-glass is defined as follows:

(1) Dissipation of heat from the waste package to the near field is sufficient to keep the centerline temperature of the vitrified waste below the transformation temperature to avoid changes in the physical and chemical properties of the unaltered glass.
(2) Salt brine contact with the glass will occur when the canister or overpack materials are perforated.
(3) Redox conditions are determined by the absence of air (oxygen) and the presence of hydrogen gas formed by anaerobic steel corrosion.

For modeling of the dissolution of HLW glass as basis for the radionuclide source term, specific data and parameters are listed in the Appendix (Tab. A - 1).

4.2 Spent Nuclear Fuel

Influence of canister corrosion

In case the confinement (thick-walled metallic canister and fuel cladding) loses integrity and brine enters the canister, release of radionuclides from the instant release fraction (IRF), corrosion of the spent nuclear fuel matrix and consecutive release of matrix bound radionuclides need to be considered. Corrosion of canister materials, cladding and spent nuclear fuel is described elsewhere [9, 160]. Canister materials constructed from carbon steel or on cast iron with spherical graphite such as GGG 40.3 show a rather homogeneous general corrosion under the geochemical conditions expected in a deep underground repository. Due to the expected corrosion, a corrosion allowance is taken into account. The actual corrosion rate of the canister depends on the geochemical properties of the attacking solutions, such as concentrations on main and trace components, pH, redox conditions, and ionic strength [161]. Data are presented in Tab. IX.

Tab. IX Corrosion of carbon steel GGG 40.3 and fine mild-steel 1.0566 as function of temperature in $MgCl_2$-rich and in saturated NaCl solution as well as in natural rock salt (in-situ experiment) [161].

T °C	$MgCl_2$ rich solution	NaCl solution	In-situ exp. in natural rock salt (Asse)
90	70 µm/yr.	5 µm/yr.	< 0.1 µm/yr.
170	199 µm/yr.	46 µm/yr.	< 0.1 µm/yr.

Under reducing conditions in near neutral / weakly alkaline systems, observed corrosion products are magnetite (Fe_3O_4) and amorphous iron hydroxides and hydrogen gas. During the corrosion process, dissolved iron reacts with the aqueous medium and forms ferrous hydroxide where iron is divalent (Fe^{II}). At sufficiently low redox potentials (absence of oxygen), $Fe(OH)_2$ is transformed into so-called "green rust" layered double hydroxides, which are stable only in the absence of oxygen. Chloride ions are included in the "green rusts" which consists of both Fe^{II} and trivalent iron (Fe^{III}). The “green rust” end member composition is as following

$[Fe^{II}_3Fe^{III}(OH)_8]^+Cl^-\times H_2O$

and can be formed at $[Cl^-]/[OH^-] > 1$ [162]. Especially in concrete systems, green rust formation is responsible for depassivation of steel. In the presence of $MgCl_2$-rich brines, $(Fe,Mg)(OH)_2$ and $Fe(OH)_2Cl$ compounds were found and characterized [163].

Corrosion of Zircaloy

Corrosion behavior of zircaloy-4 was investigated in saturated NaCl solution, $MgCl_2$-rich brine and bentonite water [164]. Corrosion rates of < 0.1 µm/yr. were measured. However, in the presence of H_2 gas formed by corrosion of steel, Zircaloy-4 shows a strong tendency of embrittlement [165]. ZrH_2 is formed rapidly onto the grain boundaries and influences the mechanical properties of the zircaloy negatively. In spite of the low corrosion rate of zircaloy, it can be expected that shortly after the formation of a H_2 gas pressure, the zircaloy hulls will degrade.

Control rods which may be disposed of together with the spent nuclear fuel rods are composed of different materials, such as silver–indium–cadmium alloys [166], hafnium or boron carbide. The behavior of these materials in disposal relevant systems is not sufficiently investigated.

The considered evolution scenario for spent nuclear fuel is defined as follows:

(1) Contact of salt brine with the fuel will occur only when the overpack materials are perforated. Most of safety analyses do not attribute any safety function to the cladding. At the time when perforation will occur, β- and γ-dose rates at the spent nuclear fuel surface are expected to be lower compared to α-dose rate (see Fig. 7).
(2) Dissipation of heat from the waste package to the near field is sufficient to avoid unpredictable changes in the physical and chemical properties of the fuel prior to water access.
(3) The H_2 formed by the anoxic corrosion of iron from the container and potential metallic overpacks and by radiolysis accumulates near the spent nuclear fuel. H_2 remains dissolved according to Henry`s law. Due to corrosion of the canister the maximal H_2 production is calculated to be 32100 $Nm^3(H_2)$ per Pollux canister and a H_2 partial pressure of 20 MPa is expected [167].

From the geometries given in work package 5 [65] the mol ratios of UO_2 to water and iron to water were calculated as 1.6/1.7 and 73.0 for the POLLUX disposal concept and as 80.4/83.2 and 610.9 for the BSK 3 concept. With increasing convergence of the backfill, the ratios will continue to increase. (For complete Fe corrosion the mol ratio of iron to water needs to be 0.75 maximum.) The simplified boundary conditions taken into account for the considered evolution scenario are given in Tab. X).

Tab. X Geochemical boundary conditions for the considered evolution scenario

		POLLUX concept	**BSK 3 concept**
		PWR / BWR	PWR / BWR
mol ratios of inventory in mol/L	U / water	1.6 / 1.7	80.4 / 83.2
(cf. Tab. IV)	Fe / water	73.0	610.9
pH_m of the solution	NaCl solution	7 – 9	7 – 9
	$MgCl_2$ rich solution	6 -9	6 -9
Gas atmosphere	pH_2	<20 MPa	<20 MPa
Redox condition		reducing	reducing

4.3 CSD-C waste

No specific boundary conditions can be derived for the considered evolution scenario.

4.4 Human intrusion scenarios

Human intrusion scenarios are not in the focus of the present study. However, to demonstrate the effect on the geochemical boundary conditions, an example is given:

One possible human intrusion scenario is a drilling into the disposal level of the Gorleben salt dome and subsequent leaching of a storage cavern having a volume of ~100 000 m^3. Independent if the drill hits one or more waste packages (which may increase the surface area of the exposed waste form), changes in the geochemical conditions compared to the considered scenario without human intrusion have to be accounted for:

(1) It is assumed that human intrusion occurs, when a homogeneous temperature field has formed over the area of solution mining.
(2) Due to the leaching process, only NaCl solution has to be considered. The volume is in the range of 10^5 m^3.
(3) Caused by drilling, hydrogen escapes and furthermore, the solution is saturated with respect to oxygen

Tab. XI Geochemical boundary conditions for the human intrusion scenarios.

		Value
pH_m of the solution	NaCl solution	7 – 9
Gas atmosphere	pH_2	0 MPa
Redox condition		O_2(g) saturated
Carbonate		pCO_2 of air

5 Radionuclide source term

The definition of geochemical boundary conditions within this study is highly simplified, also due to the preliminary and rough definition of the near-field constituents. As a consequence from these simplifications, the radionuclide source term has explicitly a preliminary and orienting character. It does not supersede the development of a site-specific radionuclide source term in a Safety Case for a potential repository in the Gorleben salt dome.

5.1 Kinetically controlled radionuclide mobilization

5.1.1 HAW glass

Grambow [2] described the kinetically controlled barrier function of HLW glass in an integrated near field. In this report, a calculation method is given to estimate the short term Si mobilization depending on the disposal conditions, such as temperature, gap volume between canisters and salt rock, backfill concepts, and solution exchange rates. This information allows determination of the transition between the short term dissolution rate and the long term rate and is illustrated with an example:

Brine comes into contact with the HLW glass after 500 years. At this time, the temperature is 150 °C, decreasing until 1000 years to 100 °C and to 50 °C after 2000 yrs. The void volume per canister is constant (100 L per canister). The leachable surface of the glass block is in the range of 1 m^2. In this case, Si saturation is reached within a few hours/days.

Radionuclide release from HLW glass is described by eq. 10 (for details on the determination of short and long-term rate see Section 3.1.2):

$$c_{RN}^{dissolved}(t) = f_{RN}^{glass} \cdot \frac{1}{void\ volume} \cdot \left(\int_0^{\tau} r_{short}(\tau) \cdot dt + \int_{\tau}^{t} r_{long}(t) \cdot dt \right) \qquad \text{eq. 10}$$

τ indicating the leaching duration when the transition between short term and long term rate of glass dissolution is defined:

$$c_{Si}^{dissolved}(\tau) = c_{Si}^{saturated} \qquad \text{eq. 11}$$

Direct disposal of glass canisters in deep boreholes is characterized by the table “Specific data for modelling the HLW glass dissolution” in the Appendix. Listed data can be used for calculating τ and the released radionuclide mass as function of time.

5.1.2 Spent nuclear fuel

5.1.2.1 Fast / instant release fraction

Based on experimental studies in low ionic strength systems at ambient temperatures and theoretical considerations [67, 68] estimated the radionuclide inventory that is present within gap, the grain boundaries, the high burn-up structures of the fuel and the cladding which may be rapidly released when the canister and cladding is breached. IRF estimates for various fission products and activation

products for UOX fuel from pressurized water reactors are given in Tab. XII (compilation of [68]). IRF values for MOX fuel are significantly higher than for UOX fuel due to the large contribution of Pu-rich agglomerates. For MOX fuel with burn-up of 40 to 60 GWd /(t HM), [168] presented IRF values for fission gases released from the gap in the range of 3.8 to 16.6 % and for fission gas released from Pu-rich agglomerates of 50 %.

In their review, Loida et al. [130] reported ^{137}Cs IRF from fuel samples measured in $MgCl_2$-rich and concentrated NaCl solutions at 25, 90, 100, 150 and 200 °C (Fig. 17). Most of these ^{137}Cs IRF are below or in the range of the pessimistic values compiled by [68]. An IRF of 3.7 % of the total ^{137}Cs was measured in a leaching experiment with a spent nuclear fuel sample from the NPP Biblis (KWB, discharged June 1979; burnup of 36.6 GWd /(t HM)) in concentrated NaCl solution at 200 °C. This value is slightly higher than the pessimistic ^{137}Cs IRF estimate for fuel with a burn-up of 41 GWd /(t HM).

Tab. XII Best estimate values of IRF (% of total inventory) for various radionuclides for PWR UO_2 fuel (Pessimistic estimate values in brackets [67]).

Burn-up (GWd/t HM)	41	48	60	75
fission gas	1 (2)	2 (4)	4 (8)	8 (16)
^{14}C	10	10	10	10
^{36}Cl	5	10	16	28
^{90}Sr	1 (2)	1 (3)	1 (5)	1 (9)
^{99}Tc, ^{107}Pd	0.1 (1)	0.1 (3)	0.1 (5)	0.1 (9)
^{129}I, ^{135}Cs, ^{137}Cs	1 (3)	2 (4)	4 (8)	8 (16)

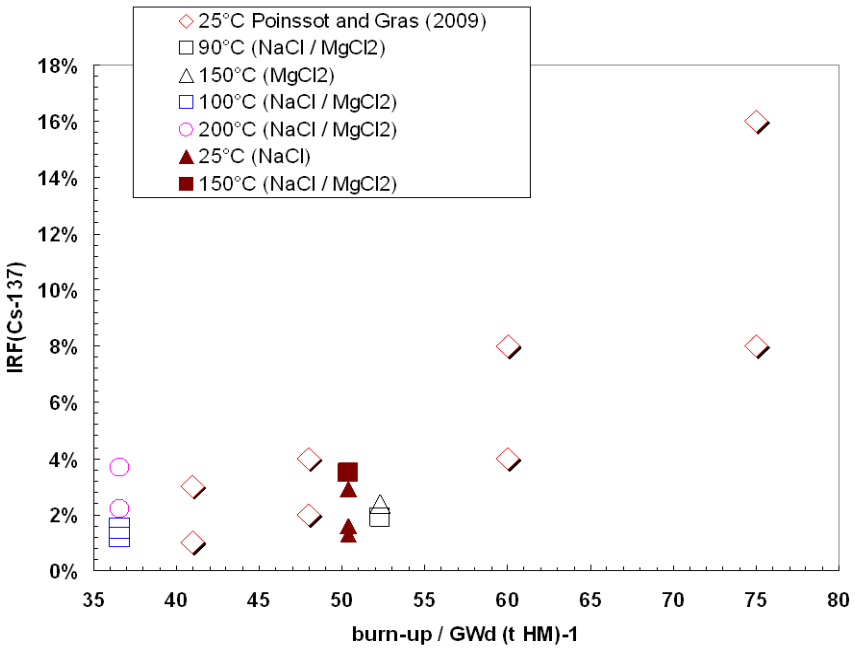

Fig. 17 ^{137}Cs IRF estimates (data from [67, 68]) and ^{137}Cs IRF measured in $MgCl_2$-rich and concentrated NaCl solutions at 25, 90, 100, 150 and 200 °C (data from [130]).

5.1.2.2 Kinetically controlled radionuclide mobilization

The release rate of ^{90}Sr is used as a proxy to assess the rate of the UO_2 matrix dissolution rate. A comparison of results of several Canadian, European, German, Swedish and US-American research programs on spent nuclear fuel corrosion in various synthetic groundwater shows that ^{90}Sr release rates (measured after 100 days) scatter between 10^{-5} and 10^{-7} (FIAP(^{90}Sr)/d) (Fig. 18). Most ^{90}Sr release rates were measured under weakly reducing / anoxic conditions. Under strongly reducing conditions and an elevated hydrogen partial pressure (pH_2 > 2 bar), relatively low release rates of < 10^{-8} (FIAP(^{90}Sr)/d) were measured in bromide-free NaCl brine [85]. Release rates of about 10^{-6} (FIAP(^{90}Sr)/d) were measured in a brine sampled from the Gorleben site ("Gorleben Einschlusslauge") in presence and absence of iron powder [11].

A similar ^{90}Sr release rate was observed in bromide-free NaCl brine at pH_2 = 0.2 bar [85]. When the hydrogen partial pressure is increased from 0.0003 to 3 bar, the ^{90}Sr release rate in bromide-free NaCl brine decreases by almost two orders of magnitude (Fig. 19). However ^{90}Sr release rate was significantly increased (up to 10^{-5} (FIAP(^{90}Sr)/d) in the presence of 10^{-4} and 10^{-3} mol $(kgH_2O)^{-1}$ bromide. Results of the complementary spent nuclear fuel corrosion and γ-radiolysis experiments allow the conclusion that Br^- traces reduce significantly the protective hydrogen effect with respect to the release of certain radionuclides (Fig. 19). In the spent nuclear fuel experiments with 10^{-4} and 10^{-3} mol $(kgH_2O)^{-1}$, low concentrations of actinides and Tc are observed. Unlike the kinetically controlled Sr release, retention processes such as precipitation of secondary phases control the release of the redox-sensitive radionuclides, i.e. actinides and Tc [57].

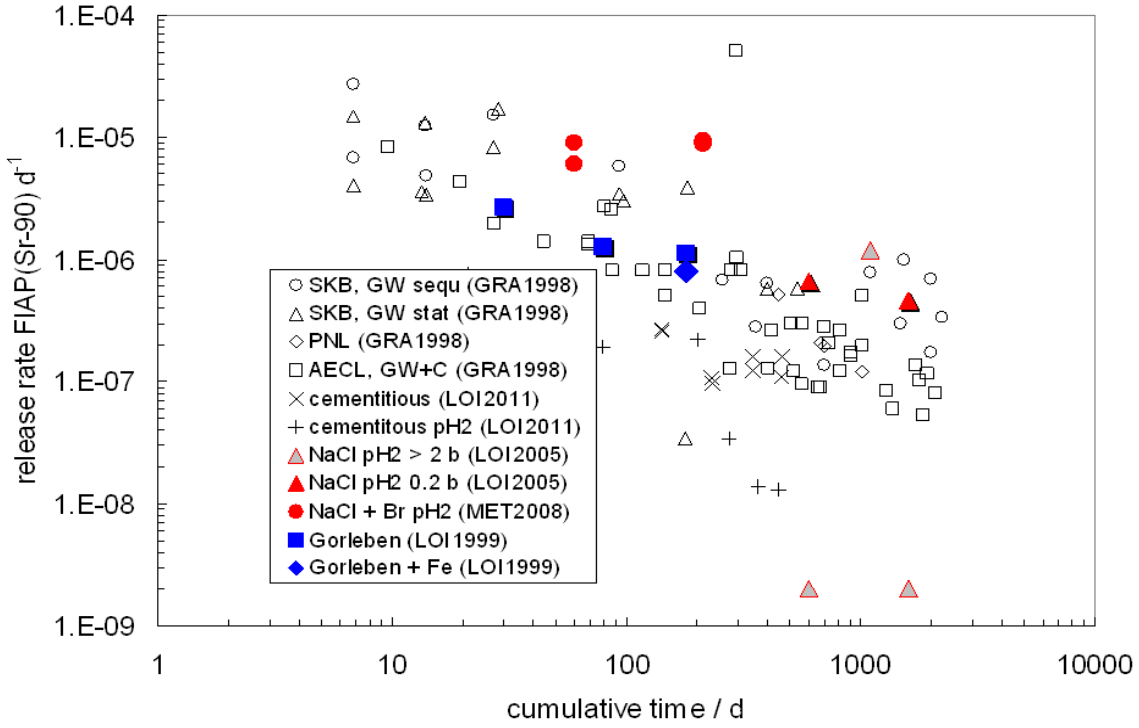

Fig. 18 Comparison of ^{90}Sr release rates (in terms of FIAP per day) measured in SNF corrosion experiments in Gorleben brine, concentrated NaCl solution and low ionic strength groundwater simulates, obtained from various international research programs. Open circles and triangles denote data from Swedish programs, open diamonds denote data from US-American programs and open squares denote data from Canadian programs (taken from [10]. X denote data from experiments in cementitious solution and + data from experiments in cementitious solution at pH_2 > 2 bar (Loida et al.

[169]). Grey triangles and red triangles denote data from experiments in concentrated NaCl solution at pH_2 > 2 bar and at pH_2 = 0.2 bar, respectively [85]. Red circles denote experiments in concentrated NaCl solution at pH_2 > 2 bar in presence of 10^{-4} – 10^{-3} mol L^{-1} Br^- [57]. Blue squares and blue diamonds denote experiments in Gorleben brine under anaerobic conditions without and with Fe, respectively [11].

Considering the effect of small concentrations of Br^- on the ^{90}Sr release rate used as a proxy for the UO_2 matrix dissolution, it is recommended to use a corrosion rate of 10^{-5} FIAP day^{-1} for spent nuclear fuel dissolution in concentrated NaCl and $MgCl_2$ brine at strongly reducing conditions. This rate is about one order of magnitude faster than the ^{90}Sr release rate measured for spent nuclear fuel corrosion in Gorleben Einschlusslauge under anoxic and reducing conditions. The studied Gorleben Einschlusslauge contained about 10 mM bromide.

For calculation of the reacted amount of spent nuclear fuel, the FIAP has to be calibrated with respect to the mass / volume ratio defined by the disposal conditions.

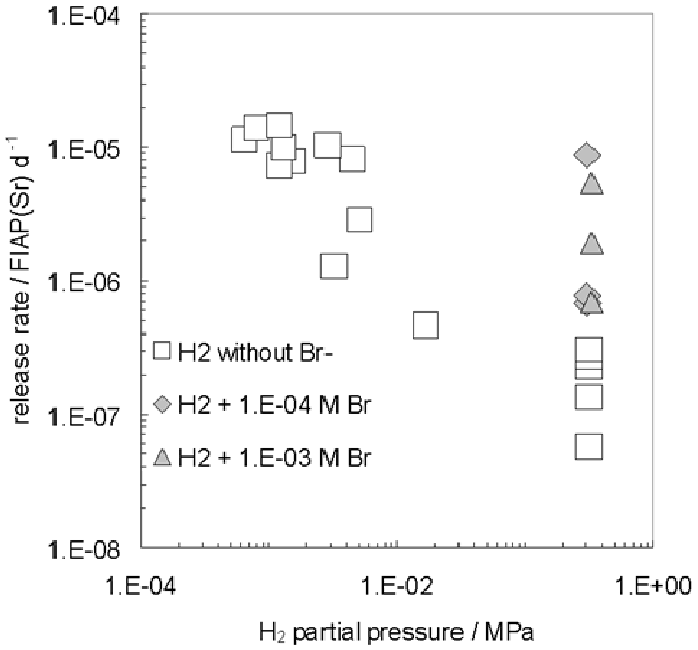

Fig. 19 Variation of Sr release rates (in terms of FIAP per day) as function of hydrogen partial pressure $P(H_2)$ in SNF corrosion experiments in NaCl brine. Squares denote results of experiments in pure NaCl brine, derived from Loida et al. (ref. [85]), diamonds and triangles denote those of experiments in NaCl brine containing 10^{-4} to 10^{-3} mol Br^- (kg H_2O)$^{-1}$, respectively.

5.1.3 CSD-C waste

Corrosion behavior of zircaloy-4 was investigated in saturated NaCl solution, $MgCl_2$-rich brine and bentonite water [164]. Corrosion rates of < 0.1 µm/yr were measured. In the presence of H_2 gas formed by corrosion of steel, Zircaloy-4 shows a strong tendency of embrittlement [165]. ZrH_2 is formed rapidly onto the grain boundaries and influences the mechanical properties of the zircaloy negatively. In spite of the low corrosion rate of zircaloy, it can be expected that shortly after the formation of a H_2 gas pressure, the zircaloy hulls will degrade.

In 1987 irradiated Zircaloy from PWR MOX fuel used in the Kernkraftwerk Obrigheim (KWO) and from BWR fuel used in Kernkraftwerk Isar (KKI-1) was investigated by Kraftwerk Union (KWU) [170]. The characteristic data of these materials are shown in Tab. XIII.

Tab. XIII Characteristics of the analyzed Zircaloy from exemplary German SWR and BWR

	PWR (KWO)	**BWR (KKI-1)**
Material	Zircaloy-4	Zircaloy-2
Initial N content (cladding)	46 ppm	
Initial enrichment	3.2 wt. % ^{239}Pu	1.99 wt. % ^{235}U
Operation under full load	882 days	804 days
Burn-up average	35700 MWd/t_{HM}	22435 MWd/t_{HM}
local burn-up	40.3 MWd/kg_{HM}	24.6 – 28.0 MWd/kg_{HM}
Linear power	229 W/cm	214 W/cm
No. of cycles	3	2

The samples were prepared by (i) cutting the rod segments (hulls and fuel), (ii) removing the fuel mechanically, and to simulate the procedure in a reprocessing plant, (iii) the hull pieces were treated in boiling HNO_3 for 1 hour. The initial ^{14}C inventory was 1.9×10^4 Bq/g for the PWR and 2.4×10^4 Bq/g for the BWR material.

The cladding material was exposed to a saturated NaCl solution for 83 days at 200 °C in order to gain basic data on ^{14}C behavior after water ingress into a sealed repository. Cladding corrosion was initiated only after 100 ppm fluoride was added to the leaching medium. The observed mass loss after 83 days was 0.087 g (2.4 %) for the PWR and 0.059 (1-2 %) g for the BWR materials. The ^{14}C results obtained under these conditions indicated that cladding corrosion mobilizes about 50 % of the ^{14}C in PWR hulls and about 90 % of the ^{14}C in BWR hulls. The mobilized ^{14}C was found ~95 % in the $^{14}CO/^{14}CH_4$ fraction, whereas $^{14}CO_2$ at ~ 5 % represented a minor part. Dissolving hulls in diluted hydrofluoric acid showed similar ^{14}C species distribution. This is shown in Tab. XIV .

Tab. XIV Measured speciation of ^{14}C leached from zircaloy in saturated NaCl at 200 °C

	PWR (Bq/g)		**BWR (Bq/g)**	
	$^{14}CO_2$	**$^{14}CO/^{14}CH_4$**	**$^{14}CO_2$**	**$^{14}CO/^{14}CH_4$**
Gas phase	2.8×10^1	1.0×10^4	7.8×10^1	2.4×10^4
solution	3.5×10^2	1.6×10^1	2.5×10^2	$< 1.9\times10^1$
solid	9.8×10^1	$< 1.4\times10^1$	$< 1.0\times10^2$	$< 5.0\times10^1$
Sum	**4.8×10^2**	**1.0×10^4**	**4.2×10^2**	**2.4×10^4**

Kaneko et al. [171] performed a study on the chemical speciation of ^{14}C leached from simulated hull waste under disposal conditions. The chemical speciation of carbon leached from carbon-containing Zr and Fe-based metallic materials were investigated. Both organic and inorganic carbon were identified in the leaching solution, and the concentrations of total carbon (organic plus inorganic) in the leaching solutions increased with time. The carbon concentrations in the leaching solution for both metallic samples were higher at higher pH. With High Performance Liquid Chromatography (HPLC), organic carbon was identified to be low-molecular weight alcohols, carboxylic acids and aldehydes. To explore the chemical state of carbon in the matrix materials, the leaching experiments were car-

ried out also for ZrC, Fe_3C, powder mixtures of carbon and zirconium, and of carbon and iron. The low-molecular weight organic carbon was detected only in the case of the carbides ZrC and Fe_3C. The result suggests that the chemical speciation of carbon in zirconium or iron is mainly carbide.

Agarwala et al. [172] determined the diffusion of carbon in zirconium, and zircaloy-2 in the temperature range 873–1523 K, using the residual activity technique. The diffusivities (in m^2/s) in the α and β phases could be represented by

$D_{\alpha\text{-}Zr}(873\text{-}1123\ K) = (2.00 \pm 0.37) \times 10^{-7} \times \exp[-(151.59 \pm 2.51)/RT]$

$D_{\alpha\text{-}Zyr\text{-}2r}(873\text{-}1043\ K) = (1.41 \pm 0.32) \times 10^{-7} \times \exp[-(158.99 \pm 3.14)/RT]$

$D_{\beta\text{-}Zr}(1143\text{-}1523\ K) = (8.90 \pm 1.60) \times 10^{-6} \times \exp[-(133.05 \pm 1.46)/RT]$

$D_{\beta\text{-}Zyr\text{-}2r}(1263\text{-}1523\ K) = (2.45 \pm 0.61) \times 10^{-5} \times \exp[-(150.29 \pm 1.72)/RT]$

The activation energies are given in kJ/mol. In the phase transition region, the diffusivities could be represented by the empirical relation: $D = D_\alpha^{C\alpha} \cdot D_\beta^{C\beta}$, where C_α, C_β are the concentrations of the two phases in the alloy and D_α, D_β are the extrapolated values of diffusion coefficients in the α and β phases respectively.

In 2007, H. Tanabe [173] presented a study on the "characterization of hull waste in underground condition". In the Japanese safety assessment for an underground disposal, ^{14}C from zircaloy wastes is the key radionuclide. Therefore, the study included irradiated Zircaloy (Zry) tubes of PWR and BWR. Key parameters which are evaluated are the inventory of ^{14}C in Zry metal and Zry oxide film, the release properties from metal and oxide films, the chemical form of ^{14}C in the presence of groundwater, and finally the distribution coefficient to various cements. The samples were obtained from PWR spent nuclear fuel with a burn-up of 47.9 GWd/t) and from BWR spent nuclear fuel with a burn-up of 39.4 GWd/t). The initial nitrogen concentration was 47 ppm in the case of the PWR and 34 ppm for the BWR. The reported inventory and ^{14}C distribution is shown in the following table (Tab. XV).

Tab. XV Characteristics of the analyzed zircaloy and oxide layers [173]

	thickness, µm		weight, %		activity, 10^4 Bq/g			C-14 distribution, %		note
	Zry metal	oxide layer	Zry metal	oxide layer	Zry metal	oxide layer	oxide/ metal	Zry metal	oxide layer	oxide layer
PWR 47.9 GWd/t N: 47 ppm	-	-	-	-	3.0	4.4 (5.9)*	1.5 (2.0)*	83	17	inner + outer
BWR 39.4 GWd/t N: 34 ppm	752	20 outer thin inner	97.8	2.2	1.9	3.3 (4.4)*	1.7 (2.3)*	96	4	outer

* in terms of metal weight

^{14}C concentrations were found by a factor 1.3 to 2.3 lower in the experiments of Tanabe et al. [173] than calculated. Leach test have been performed between 3 and 5.5 months. ^{14}C leach rates were in the range between 2 - 2.3×10^{-3} yr^{-1} for the oxide layer covering the Zircaloy and in the range between 2.9 and $4.6 \times 10^{-5}/yr^{-1}$ for Zyr metal.

The speciation of ^{14}C was already presented above (Kaneko [171]).

The Japanese and German experiments revealed the comparable ^{14}C concentrations in the Zircaloy material. Meanwhile, for high burn-up fuel rods, zircaloy-4 is partly replaced by the tenary Zr-1%Nb alloy M5 with a slightly lower nitrogen concentration (0.002 wt. %). However, radionuclide release data under disposal conditions are not available in literature.

5.2 Thermodynamically Controlled Radionuclide Mobilization

The simplified scenario, which is defined in Chapter 1 is the basis for the thermodynamically determined source term. An overview on the essential criteria for the reference systems is given in Tab. XVI. The scenario "human intrusion" is additionally included in the table to represent a system with different redox conditions and, consequently, partly different dominating actinide oxidation states.

Tab. XVI Summary of the essential criteria of considered NaCl and $MgCl_2$ dominated systems and expected dominating radionuclide oxidation states.

	NaCl system	**$MgCl_2$ system**	**human intrusion scenario**
Reference system	5.6 m NaCl	> 4.0 m $MgCl_2$	5.6 m NaCl
Carbonate	scenario dependent	scenario dependent	carbonate present
pH_m	$6 < pH_m < 9$	$6 < pH_m < 9$	$6 < pH_m < 9$
Redox state	reducing	reducing	oxidizing
Radionuclide oxidation state			
Americium	Am(III)	Am(III)	Am(III)
Thorium	Th(IV)	Th(IV)	Th(IV)
Uranium	U(IV), U(VI)	U(IV), U(VI)	U(VI)
Neptunium	Np(IV)	Np(IV)	Np(V)
Plutonium	Pu (III), Pu(IV)	Pu (III), Pu(IV)	Pu(IV), Pu(V)
Technetium	Tc(IV)	Tc(IV)	Tc(VII)
Zirconium	Zr(IV)	Zr (IV)	Zr (IV)

5.3 Effect of temperature on radionuclide solubility

As the temperature ranges for the scenario considered within this study also include elevated temperature conditions, it needs to be discussed how well the predictions made for room temperature can be transferred to the systems at higher temperatures potentially relevant. The following paragraphs are intending to outline the basic assumptions and problems related to this aspect. It is not meant to provide a comprehensive review of elevated temperature effects, but to give an overview on the potential impact of temperature.

5.3.1 Temperature dependence of thermodynamic properties in the aquatic system

Modeling of the aqueous chemistry at elevated temperatures requires knowledge of the stability and solubility products of solubility limiting solid phases, the effect of temperature on complex formation constants and finally ion-interaction parameters for all species involved (SIT, Pitzer). At present, no comprehensive thermodynamic model covering elevated temperature conditions is available. Experimental work on aqueous actinide chemistry at higher temperature is rather limited and does not cover all relevant systems. On the other hand, thermodynamic data for the main components of the solution matrix are often available with adequate precision.

Thermodynamic data used to predict the chemical speciation of contaminants in the environment rely on data measured at 20 °C or 25 °C. In the waste package and disturbed zone of the repository where elevated temperatures will exist, the calculated speciation can dramatically differ from the speciation at 20 - 25 °C. For instance, up to three orders of magnitude difference in the extrapolated and actual stability constants has been observed. Typical mathematical extrapolation techniques, such as the van't-Hoff or Helgeson-Kirkham-Flowers equations, cannot be assumed to predict the chemical systems at higher temperatures with the required precision.

As a recent case study, the carbonate complexation of Cm(III) in aqueous solutions with high ionic strength was investigated below solubility limits in the 10-70 °C temperature range using time-resolved laser-induced fluorescence spectroscopy (TRLFS) [174]. The equilibrium constant, K_3, for the formation reaction $Cm(CO_3)_2^- + CO_3^{2-} \rightleftharpoons Cm(CO_3)_3^{3-}$ was determined ($\log K_3 = 2.01 \pm 0.05$ at 25 °C, I = 3 M ($NaClO_4$)). The $\log K_3$ value for Cm(III) was found to increase linearly with 1/T, reflecting a negligible temperature influence on the corresponding molar enthalpy change, $\Delta_r H_3 = 12.2 \pm 4.4$ kJ mol^{-1}, and molar entropy change, $\Delta_r S_3 = 79 \pm 16$ J mol^{-1} K^{-1}. These values were extrapolated to I = 0 with the SIT formula. Virtually the same values were obtained from the solubility data for the analogous Am(III) complexes, which were reinterpreted considering the transformation of the solubility-controlling solid. The reaction studied was found to be driven by the entropy. This was interpreted as a result of hydration changes. As expected, excess energy changes of the reaction showed that the ionic strength had a greater influence on $\Delta_r S_3$ than it did on $\Delta_r H_3$.

Skerencak et al. [175, 176] have also investigated Cm(III)-nitrate and Cm(III)-fluoride complexation at elevated temperatures. Nitrate complexation was studied at strongly acidic conditions up to 200 °C, the fluoride system up to 90 °C. For both ligands the tendency towards complex formation with Cm(III) increases with increasing temperature. In the nitrate system, the mono-nitrato complex is dominant up to 160 °C, above this temperature the di-nitrato complex dominates speciation. The fluoride system studies show an analogous inversion of species distribution between the mono- and di-ligand complex even at temperatures below 90 °C. Although the experimental boundary conditions in these studies are not relevant for waste disposal scenarios, a strong influence of temperature upon actinide speciation was shown.

Fig. 20 shows the stability constant for neutral complexes ($y \leq z$) as function of the temperature [177]. In the cases of divalent metals, the complexation constant increases only by about one order of magnitude between 25 °C and 350 °C. Only very few Me(II) hydroxides show a higher increase in the temperature range considered.

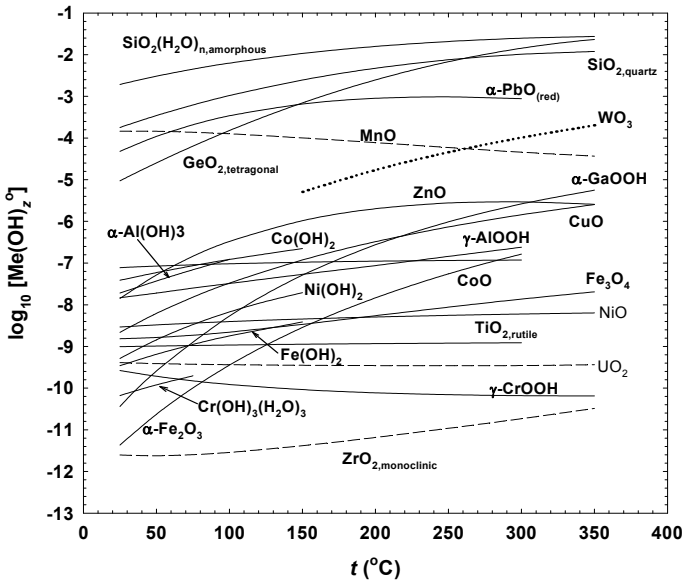

Fig. 20 Solubility of metal oxides as function of temperature [177].

The temperature dependence of complex formation constants has only been investigated for a limited number of ligands and actinides. The situation regarding the ion-interaction parameters, required to calculate activity coefficients for the different aquatic species included in a chemical model is equally problematic.

At present, no detailed model prediction of complex formation at higher temperatures can be made and no adequate description of actinide trace activity coefficients at elevated temperatures is available. It is, however, possible is to give trends in order to estimate solubility data development as a function of T, which in turn can be extremely valuable for safety case considerations.

5.3.2 Temperature dependence of the solubility of solid phases

The stability and solubility product of the solubility limiting solid phases must be evaluated for elevated temperature conditions. Nickel and zinc solubility and speciation have been investigated for PWR primary circuits [178]. Experimental results on the solubility of nickel oxide and hydroxide are determined as functions of temperature and pH. The former was studied from 0 to 350 °C, whereas the hydroxide was investigated from 0 to 200 °C, at pressures exceeding the saturation vapor pressure. These experiments were carried out in either flow-through cells or a hydrogen-electrode concentration cell for mildly acidic solutions. The results of these experiments were treated with a thermodynamic model involving two aqueous nickel species whose solubility constants were then fitted as functions of temperature, to cover the range of operation of the primary circuit of a PWR. The solubility of NiO and ZnO at 100, 200 and 300 °C shown in Fig. 21 are taken from [179]. Fig. 21 indicates the tendency of both metal oxides to precipitate at lower pH for increasing temperature at $pH_m < 7$.

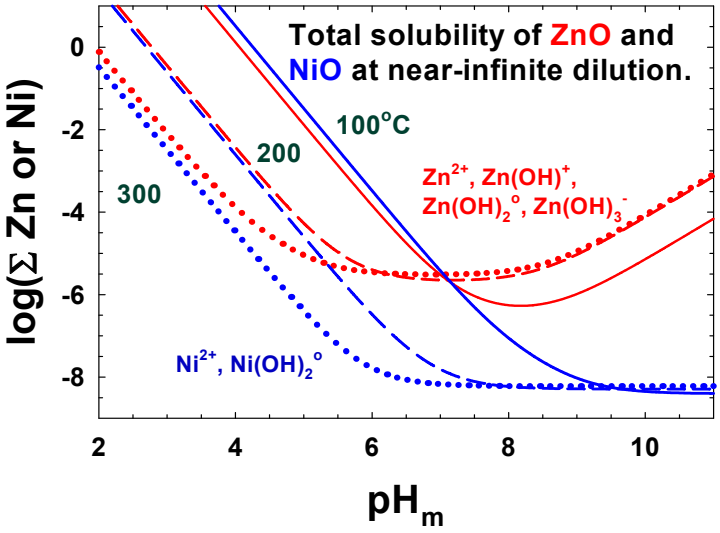

Fig. 21 Total solubility of NiO and ZnO at 100, 200 and 300 °C.

In the case of lanthanide/actinide elements, only a few measurements are published and therefore only a preliminary and cautious evaluation of temperature effects can be attempted here. Rao [180] investigated the solubility of $Nd(OH)_3$ in 0.1 M NaCl solution between 25 °C and 90 °C. Within the scatter of experimental data, no significant temperature effect was found. Giffaut analyzed the solubility of Am(III) in NaCl-$NaHCO_3$-Na_2CO_3 systems. between 20 °C and 70 °C [181]. The variation of the dissolved Am concentration in the temperature range under investigation was less than a factor of 5. Unfortunately the solubility controlling solids could not be identified.

For ThO_2(cr) and UO_2(cr), the crystallinity increased with increasing temperatures [182]. The rather fast transformation into the thermodynamically stable solid phases seems to be a general trend increasing with higher temperatures. Obviously the tendency towards formation of metastable solids that often affects experimental work at room temperature is overcome by the much faster kinetics at increased temperature conditions. The elevated temperature conditions seem to favor the transformation into more stable (less soluble) phases. Experiments by Parks and Pohl [183] showed no temperature dependence of the solubility of UO_2(cr) up to 300 °C. Also no temperature effect was found for Np(V) solubility at pH = 6 [184]. However, at 7 ≤pH ≤ 8.5 the solubility dropped by 0.5 orders of magnitude. The measured Pu concentration in presence of PuO_2(am,hyd) decreased slightly log[Pu]= -7.7 (25 °C), -8.5(60 °C) to -8.4(90 °C) with mainly colloidal species being dominant in solution.

From these studies, one can conclude that temperature changes between room temperature and 90 °C have no significant effect on the actinide solubility of the systems investigated so far. In this context, the counteracting effects of temperature on the solubility product and the complex formation should be recalled. It should be understood, that the assumption of only moderate effects of temperature on total solubility is a strong simplification and needs to be validated in order to decrease the uncertainties associated with this approach.

5.4 Relevance of carbonate in the high-level waste disposal

Carbonates are not expected to be present at relevant concentrations in the disposal galleries in the Gorleben salt dome. However, it might be assumed that carbonates can form by degradation of plastic materials which are present in the containers / overpacks for neutron moderation / shielding. A list of the mass of plastic in the containers is given in Tab. XVII.

Tab. XVII Plastic materials in containers / overpacks for neutron moderation / shielding [185].

	Pollux-10 cask	**BSK3 cask**
HM load per canister in kg (DWR / SWR)	5420 / 5610	1626 / 1683
Polyethylene per canister in kg	total 1540	total 7
Carbon (C_2H_4) in mol	total 5.5×10^4 (2.4 C /U)	total 250 (0.04 C/U)

Another source of carbonates in the near-field environment is correlated with the presence of hydrocarbons in the Gorleben salt formation. At elevated temperatures, the hydrocarbons may undergo a thermochemical sulfate reduction [186]. Most of the papers published on sulfate reduction imply the presence of bacteria (e.g. [187, 188]). According to [189], one can separate two different processes, the bacterial sulfate reduction (BSR), which occurs at temperatures below 80 °C and the thermochemical sulfate reduction (TSR), which has been observed at temperatures higher than 100 - 140 °C. While BSR seems to occur instantaneously, TSR is a kinetically-driven process. Detailed investigations have been performed using CH_4 to C_3H_8 hydrocarbons and pure calcium sulfate [190]. Though dissolved SO_4^{2-} is in fact required for thermochemical sulfate reduction, the simplified overall reaction can be written as

$$CaSO_4 + CH_4 \rightarrow CaCO_3 + H_2S + H_2O \qquad \text{eq. 12}$$

It is assumed that the number of carbon atoms per hydrocarbon molecules in the Gorleben rock salt is 6 to 16, mostly being ≤ 10 [186]. In the case of a hydrocarbon C_8H_{18}, eq. 12 changes to

$$8CaSO_4 + C_8H_{18} \rightarrow 8CaCO_3 + 8H_2S + H_2O + \text{oxidized species} \qquad \text{eq. 13}$$

A complete reaction scheme for the C_1 to C_3 compounds is given in [190]. The outcome of this work on the thermodynamics and kinetics of reactions between C1–C3 hydrocarbons and calcium sulfate in deep carbonate reservoirs revealed measured date and a model to estimate the reaction rates based on spontaneous reaction experiments. The processes simulated by these experiments are close to the situation to be expected in the disposal galleries. The authors calculated time periods which are required to transform sulfate into sulfide. It was shown that the reaction between CH_4 and $CaSO_4$ had the highest activation energy while that between C_3H_8 and $CaSO_4$ had the lowest activation energy. When extrapolated to the temperature of the geological environment, the time needed to reach 50 % conversion at a temperature of 200 °C is 1.44 million years for CH_4 (7790 years for C_3H_8 at 200 °C). At 100°C the time period required for the 50 % conversion was calculated to be 4.8×10^{10} years (2.88×10^7 years for C_3H_8 at 100 °C) [190].

Equations 12 and 13 show that one carbonate molecule is formed per sulfate molecule. Assuming a typical sulfate concentration of a saturated NaCl solution in contact with polyhalite, the sulfate concentration is 0.1 mol/l. For this case, Fig. 22 shows the areas of predominance for the species sulfate – sulfide (red lines) and carbonate (CO_2(g), HCO_3^-, and CO_3^{2-}) – CH_4 (blue dotted lines). The figure shows a very small area (between the red and blue lines), where the reaction is possible in a closed system which means that H_2S or HS^- and carbonate species can co-exist.

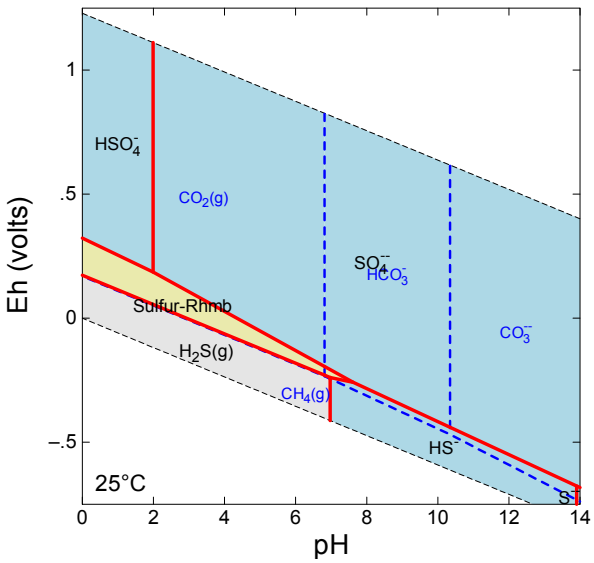

T = 25 °C
p = 1.013 bar
a_{HCO3} = a_{SO4} = 0.1

Fig. 22 Areas of predominance of sulfate – sulfide species and carbonate species – CH_4.

Fig. 22 only serves as a rough estimation as it is calculated for 25 °C while thermochemical sulfate reaction occurs at temperatures higher than 100 °C. In addition, predicted and actual redox conditions often differ due to the slow kinetics of oxidation/reduction processes. With increasing temperatures, however, reaction rates tend to increase and TSR can be accelerated due to alteration of the hydrocarbons and changes in their redox potential.

6 Radionuclide solubility

Analyzing the waste form behavior under the considered evolution scenario, a list of elements is identified for which the maximum dissolved concentrations can be expected to be controlled by the solubility of solid phases. The following solubility limits are derived for a scenario without carbonate and other complexing ligands for 25 °C.

Within safety assessment modeling, the reported data can be used as an upper limit for the radionuclide concentrations expected for the boundary conditions and disposal concept defined above. Subsequent sorption processes are not included. However, it should be clearly noted that this constitutes a simplified approach of orientating character valid only for the considered scenarios. Both the analysis of the geochemical boundary conditions and the subsequent source term estimation need to be systematically extended, improved and validated in order to reduce the presently related large uncertainties in the reported solubility limits. Uncertainties are not explicitly quantified within this study.

6.1 Americium

The concentration of Americium in spent nuclear fuel is ~1000 g / tHM after 500 years. Americium exists only in the trivalent oxidation state Am(III) in disposal relevant conditions. A summary of the literature on Am including a detailed discussion of the proposed thermodynamic data is presented in a NEA book [17]. Thermodynamic data and solubility investigations have been performed directly with Am. Due to radiation protection issues and its spectroscopic properties, analogues are also applied, especially Cm(III) which is a perfect analogue with excellent spectroscopic properties. Solubility studies have been performed with Nd(III). All in all, a well advanced thermodynamic database exists for Am(III) in dilute to concentrated carbonate free NaCl, $MgCl_2$ and $CaCl_2$ solutions. Thermodynamic data of Am(III) in carbonate containing $MgCl_2$ solutions are still missing.

NaCl system

Thermodynamic data of Am(III) in the NaCl system was developed by Neck [191] and the solubility curve derived from Nd and Cm is shown in Fig. 23. Under highly alkaline conditions, the solubility of neodymium, which is taken as analogue for Am, is in the range of 10^{-8} M. In the relevant pH_m range solubility is above 10^{-1} M at pH_m = 6 and 10^{-5} M for pH_m = 9.

$MgCl_2$ system

The behavior of americium in $MgCl_2$ solution was also investigated by Neck et al. [191]. Their paper describes the carbonate free system relevant for the present work. In Fig. 24 the investigations for 3.5 M $MgCl_2$ solution are summarized. The solubility of neodymium (analogue for Am) at pH_m 9 is $10^{-4.5}$ M. The effect of carbonate was investigated [192]. No increase of the solubility in comparison to the carbonate free system in $MgCl_2$ solution was found. In contrast, at $-\log [H^+] \sim 8.4$ the measured solubility was by one order of magnitude lower as in the carbonate free system at the same pH_m.

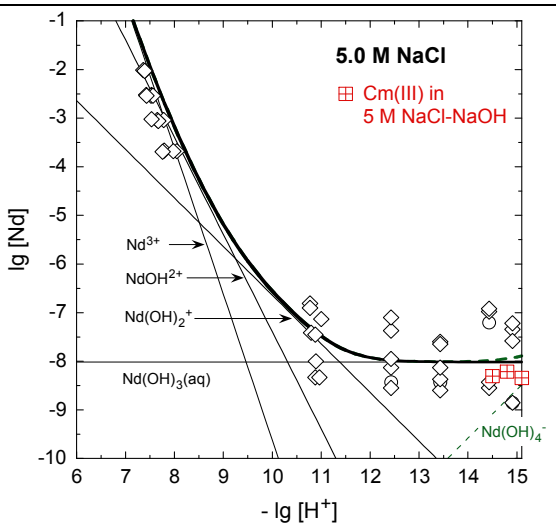

Fig. 23 Solubility of $Nd(OH)_3$(am) and Cm(III) [191]

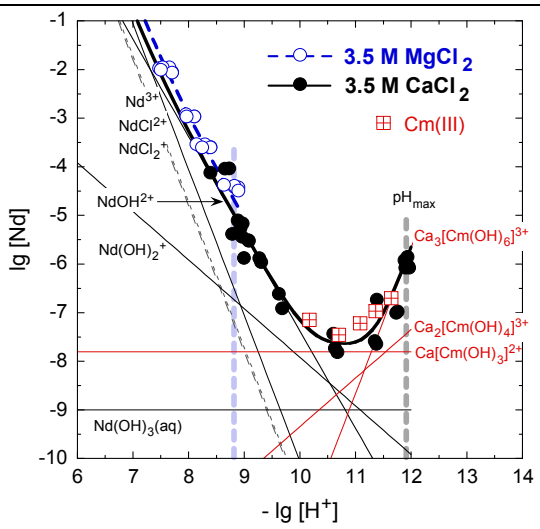

Fig. 24 Solubility of $Nd(OH)_3$(am) in carbonate free 3.5 M $MgCl_2$ solution [191, 192]

6.2 Thorium

In aqueous solutions, thorium exists only in the tetravalent oxidation state. It represents a good analogue for other tetravalent actinides; it is certainly the most investigated tetravalent actinide. A recent publication by OECD-NEA provides a comprehensive description of the present knowledge on its thermodynamic data and solubility [21].

NaCl system

The thorium concentration in NaCl solution is derived from [193]. Fig. 25 shows the solubility of amorphous thorium hydroxide ThO_2xH_2O(am) in NaCl solution. After removal of colloids solubility was found in a concentration range of 10^{-8} M for the whole relevant pH_m range, largely independent of ionic strength. Without phase separation, the thorium concentration is dominated by colloidal or polymeric Th(IV) species and ranges at 10^{-6} M. The colloid effect was corroborated by data from Nabivanets et al. [194] at low ionic strengths (Fig. 26). The concentrations of both ionic species and colloidal fractions are independent of pH_m for $pH_m > 6$.

$MgCl_2$ system

Fig. 25 shows the solubility of thorium hydroxide ThO_2xH_2O(am) in concentrated $MgCl_2$ solutions. As described in [193] and [29], the presence of colloidal Th(IV) phases are assumed from the high Th concentrations even after ultra-centrifugation. The observed concentration is ~10^{-6} M over the whole investigated pH_m range. The elevated Thorium concentration in 4.5 M $MgCl_2$ solution could be correlated with experimental artifacts and is irrelevant for source term considerations. Investigations of the carbonate complexation of Th in NaCl media [195, 196] showed that due to the low expected carbonate concentrations in the repository, the Th solubility remains in the range of 10^{-6} M.

The maximum thorium concentration in the NaCl and the $MgCl_2$ solution is estimated to 10^{-6} M.

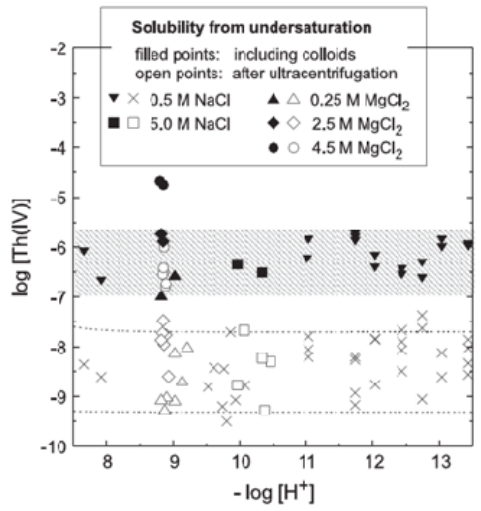

Fig. 25 Solubility of thorium hydroxide ThO_2xH_2O(am) in NaCl and $MgCl_2$ solutions [193].

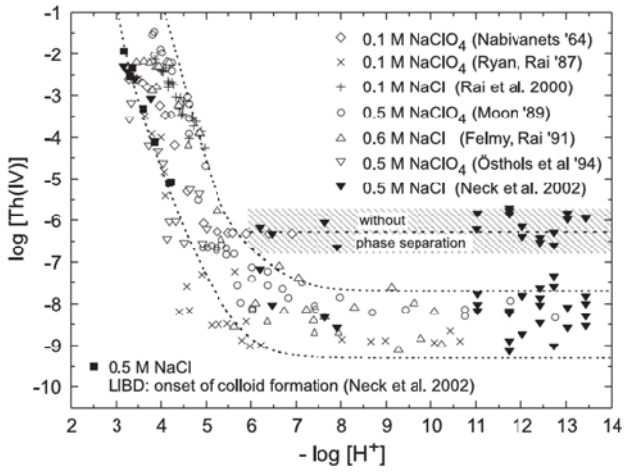

Fig. 26 Solubility of thorium hydroxide ThO_2xH_2O(am) in NaCl and $NaClO_4$ solutions [193].

6.3 Uranium

Under oxidizing or redox neutral conditions, uranium is present in the hexavalent redox state as uranyl UO_2^{2+} moiety. Under reducing conditions the tetravalent oxidation state is preferred. Under the reducing conditions in a repository, uranium will be predominantly present as U(IV). However, it is not confirmed that U(VI) species released e.g. from spent nuclear fuel are quantitatively removed. Consequently, we consider both solubility limits for U(IV) and U(VI). A similar approach has been taken by the WIPP project. Solubility data and thermodynamics of uranium are reported and reviewed in two OECD-NEA books [17, 197].

NaCl system

Under oxidizing or redox neutral conditions in a NaCl solutions (e.g. in the case of human intrusion) the uranium concentration is controlled by hexavalent U(VI) solids (see Fig. 27). Investigations for these conditions have been performed by KIT-INE [29, 198].

U(VI) concentrations in the NaCl system under oxidizing conditions are estimated between $10^{-4.5}$ M for pH_m 6 and $10^{-6.5}$ M at pH_m 9. Under reducing conditions U(IV) behaves similar to thorium and should exhibit the same tendency towards colloid formation. The solubility will be then controlled by a solid UO_2xH_2O(am) phase. In [29, 193] an approach was presented, which allows for quantification of An(IV) eigen-colloids.

Experimental investigations show that stable An(IV) colloids can be described according to the following equilibrium:

$An(OH)_4(aq) \leftrightarrow An(OH)_4(coll)$

With $\log K_{coll} = 2.5 \pm 0.8$ and: $An(OH)_4(am) \leftrightarrow An(OH)_4(aq)$

The concentration level of the tetra hydroxide complexes can be calculated as sum of the solubility products of the related actinide hydroxide solids (log $K°_{sp}(AnO_2xH_2O(am))$ and the complexation constants of this species (log $\beta_{1,4}$). An effect of ionic strength was not found (see also Fig. 25).

Using log $K°_{sp}(UO_2xH_2O)$ = -54.5 and log β_{14} = 46.0 [17] the concentration of $U(OH)_4(aq)$ results to $10^{-8.5}$ M. In combination with the colloid formation constant (log $K_{(coll)}$ = 2.5) a concentration of U(IV) colloids of 10^{-6} M is calculated. The U(IV) solubility in NaCl solutions above pH_m = 6 is estimated in the range of 10^{-6} M.

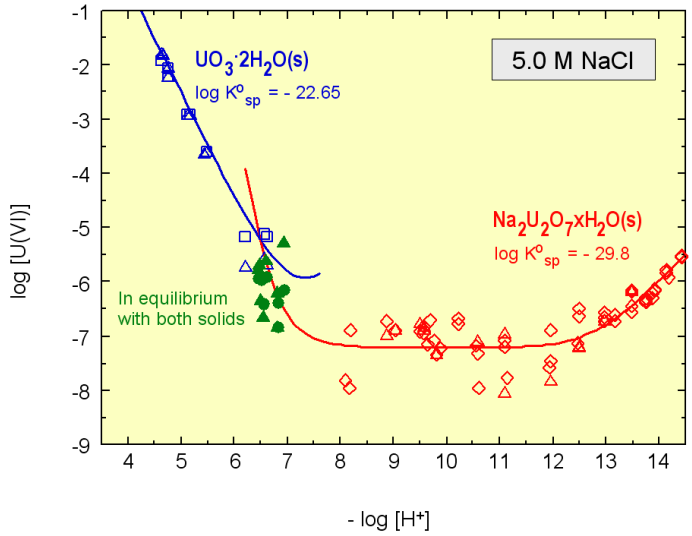

Fig. 27 Solubility of U(VI) in 5 M NaCl solution [199].

$MgCl_2$ solution

In a recent study by KIT-INE [200], the U(VI) solubility was investigated in dilute to concentrated $MgCl_2$ systems from slightly acidic conditions to pH_m fixed by magnesium-hydroxide or magnesium-oxy-hydroxides. Under these conditions, the solubility is controlled by the meta-schoepite solid phase and shows a pronounced effect of ionic strength on solubility.

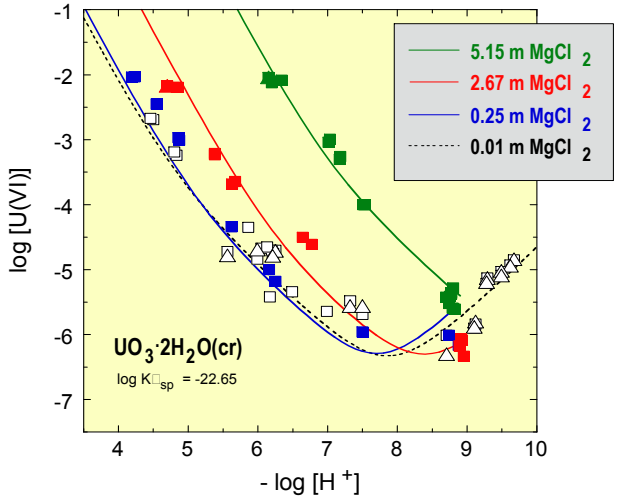

Fig. 28 Solubility of U(VI) in various $MgCl_2$ solutions

The U(VI) concentration in $MgCl_2$ solutions is estimated to $10^{-5.5}$ M at pH_m 9 and 10^{-2} M for pH_m 6.

The U(IV) concentration in $MgCl_2$ solutions is estimated to 10^{-6} M in analogy to the Th(IV) system discussed above.

6.4 Neptunium

Under oxidizing or redox neutral conditions neptunium exists in the pentavalent state Np(V), under reducing conditions in the tetravalent state Np(IV). Thermodynamic data and a detailed evaluation of various solubility test are reported in [17, 18].

NaCl system

The solubility of Np(V) was investigated experimentally in 5 M NaCl solution [29].

Fig. 29 shows that the initially precipitating $NpO_2OH(am)$ solid changes slowly into an aged solid $NpO_2OH(aged)$ having a lower solubility by 0.5 orders of magnitude.

The Np(V) concentration in the pH_m range $6 \leq pH_m \leq 9$ in NaCl solutions is below $10^{-3.5}$ M.

The solubility of Np(IV) is treated like the Th(IV) analogue. As elaborated for U(IV), the solubility is estimated by application of the thermodynamic scheme of Th(IV) [17] for Np(IV). The Np(IV) concentration is controlled by the tetra hydroxo complex $Np(OH)_4(aq)$ which is in the range of 10^{-9} M. The contribution of eigencolloids (log $K_{(coll)}$ = 2.5), reveals a concentration of Np(IV) colloids in the range of 10^{-6} M. This number is taken as upper limit of the Np(IV) concentration for NaCl and $MgCl_2$ systems.

The Neptunium(IV) concentration in NaCl and $MgCl_2$ systems is estimated to 10^{-6} M.

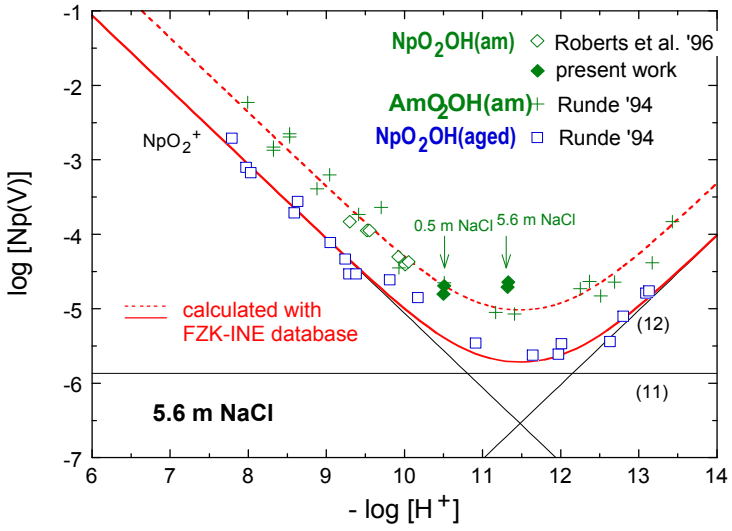

Fig. 29 Solubility of $NpO_2OH(am)$, $AmO_2OH(am)$ und $NpO_2OH(aged)$ in carbonate free 5 M NaCl/NaOH solution [29].

6.5 Plutonium

The aqueous chemistry of plutonium is very complex due to the different oxidation states Pu(III, IV, V, VI) which may even co-exist under many geochemical conditions. Under reducing conditions the tri- and tetravalent oxidation states are relevant, under redox neutral and slightly oxidizing conditions the tetra- and pentavalent states, and with further increasing redox potential and strongly oxi-

dizing conditions, even the hexavalent state may become relevant. Fundamental investigations on the plutonium solubility and speciation were performed at KIT-INE in the recent years [201-204] including highly saline solutions. OECD-NEA published a comprehensive data base of thermodynamic data on plutonium [17, 18].

Pu(III) solubility in NaCl solutions

Thermodynamic calculations and experimental data show that $Pu(OH)_3(s)$ is not stable in systems without strongly complexing ligands. Under reducing conditions in the stability field of water it converts into a thermodynamically more stable tetravalent $PuO_2(s,hyd)$. The solubility is given by the equilibrium concentrations of aqueous Pu(III) and Pu(IV) species following a reductive dissolution mechanism. In the absence of reducing and oxidizing chemical agents but in the presence of traces of $O_2(g)$, the total Pu concentration at $pH_m > 3$ is dominated by aqueous Pu(V) species and the solubility is controlled by $PuO_{2+x}(s,hyd)$, a mixed valent $(Pu^{V})_{2x}(Pu^{IV})_{1-2x}O_{2+x}(s,hyd)$. Small Pu(IV) colloids/ polymers present in neutral to alkaline solutions at a constant level of $\log[Pu(IV)]_{coll} = 8.3 \pm 1.0$ play an important role for the redox potentials in these systems and contribute to the total dissolved Pu [203].

The Pu(III) concentration in reducing NaCl systems in the range $6 \leq pH_m \leq 9$ is well established for diluted solutions. For saturated NaCl solutions, in the relevant pH_m range from $6 \leq pH_m \leq 9$, solubility of a Pu(III) hydroxide phase (analogue to $Am(OH)_3(am)$) would be partly above 10^{-4} M. However, as seen in Fig. 30 and Fig. 31 for dilute systems solid Pu(III) phases are transformed to Pu(IV) with a solubility of 10^{-6} at pH_m 6 to $10^{-8.3}$ M at pH_m 9.

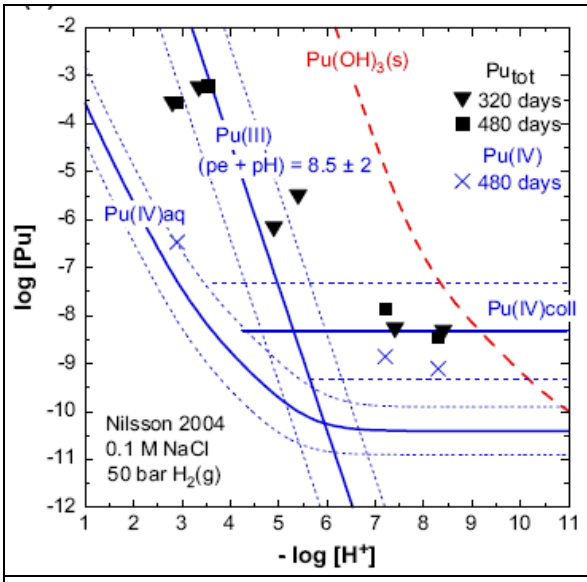

Fig. 30 Solubility of Pu(IV) hydrous oxide determined by Nilsson [205] after 320 and 480 days in 0.1 M NaCl solutions under a pressure of 50 bar $H_2(g)$ after the transformation of the initial Pu(III) hydroxide precipitate [203].

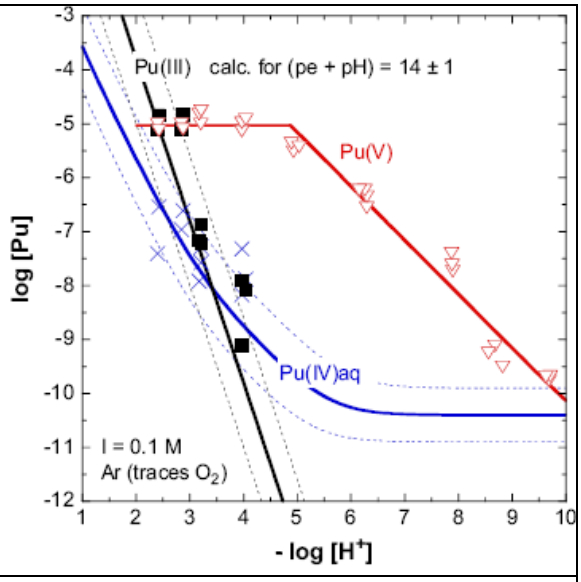

Fig. 31 Experimental results from a solubility study with Pu(IV) hydrous oxide under Ar (<10 ppm O_2) at 22 °C in 0.1 M NaCl [203]. Pu(IV) (crosses), Pu(III) (filled squares), Pu(V) (triangles)

Pu(IV) solubility in NaCl solutions

The solubility of Pu(IV) and the formation of Pu(IV) colloids was investigated experimentally by KIT-INE Neck et al. [201]. The solubility of solid PuO_{2+x}(s,hyd) is shown in Fig. 32 for a 0.1 M NaCl solution. The figure reveals the solubility of Pu(IV), Pu(V) and of Pu(IV) colloids.

Pu(IV) species in contact with a Pu(IV) solid are expected in the range $6 \leq pH_m \leq 9$. Pu(IV) in solution will be dominated by Pu(IV) intrinsic colloids at a concentration below 10^{-8} M, largely independent on the ionic strength and pH_m.

Pu(V) solubility in NaCl solutions

Fig. 32 shows also that in the relevant pH_m range, pentavalent PuO_2^+ dominates the aquatic Pu speciation whereas PuO_{2+x}(s,hyd) is the solubility limiting solid phase. In the range $6 \leq pH_m \leq 9$, the concentration of Pu(V) is between $10^{-5.5}$ (pH_m 6) and 10^{-8} M (pH_m 9). Solubility experiments by Rai et al. [206] using PuO_2(am, hyd) in 0.4 und 4.4 m NaCl in the range pH_m 5 to 8 showed only a slight dependence on the ionic strength.

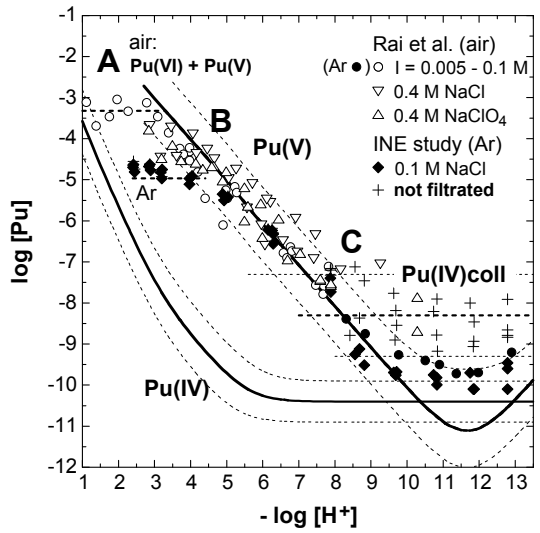

Fig. 32 Solubility of PuO_{2+x}(s,hyd) in 0.1 M NaCl [201].

$MgCl_2$ system

Only tri- and tetravalent plutonium compounds are expected under reducing conditions in $MgCl_2$ solutions reflecting the respective formation conditions.

Pu(III) solubility in $MgCl_2$ systems

For carbonate free 3.5 M $MgCl_2$ solution it was shown that under strongly reducing conditions (presence of corroding Fe powder) the sparingly soluble PuO_2(am) solid was formed in systems without strongly complexing ligands. Reductive dissolution of this phase produces dissolved Pu(III) concentrations from above 10^{-3} M at pH_m 6 and $10^{-7.5}$ M at pH_m 9. [204]. Experiments starting from oversaturation of Pu(III) show a strong decrease of the solubility to the level obtained by starting with the solid PuO_2(am), see Fig. 33.

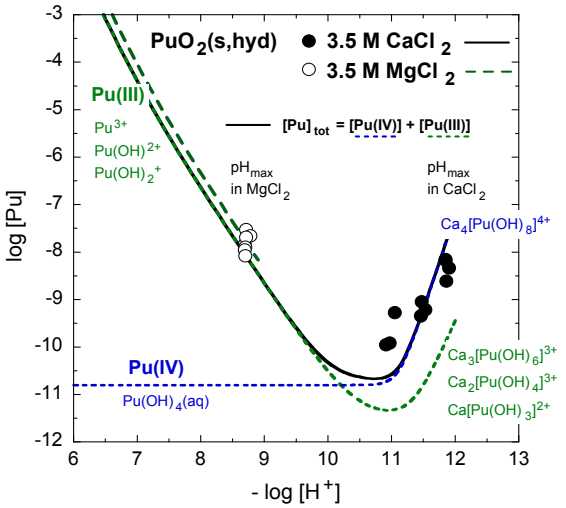

Fig. 33 Solubility of PuO_2(am) in a carbonate free 3.5 M $MgCl_2$ solution under strongly reducing conditions [204].

The solubility of Pu was also investigated in presence of carbonate which is controlled by the formation of meta-stable solids, such as Hydromagnesite / dypingite or chlorartinite. The experiments were performed in both procedures from undersaturation using PuO_{2+x}(am) solid and from oversaturation of dissolved Pu(III) [192]. The concentrations obtained from undersaturation didn't show any deviation to the carbonate free experiments. The experiments using oversaturated Pu(III) solution showed a certain decrease over 1 year, but didn't come to the lower concentration level of the undersaturation experiments. Pu concentrations remained at $10^{-5.5}$ M at pH_m 8.5. The reason is not yet clear, EXAFS investigations [207] revealed Pu(III) solids which are not yet characterized.

The Pu(III) concentration in the carbonate free $MgCl_2$ system ranges from above 10^{-3} M at pH_m 6 to $10^{-7.5}$ M at pH_m 9 in 3.5 M $MgCl_2$ brines. Considering a potential ionic strength effect for 4.5 M $MgCl_2$ solution, the Pu concentration could be higher by 0.5 log units.

Pu(IV) solubility in the $MgCl_2$ system

The estimation of Pu(IV) solubility corresponds to the considerations for Pu(IV) in NaCl solution and for the analogues Np(IV) and U(IV). The solubility is dominated by intrinsic Pu(IV) colloids which are expected to exist largely independent on pH_m and ionic strength above pH_m 6. According to the Th(IV) system [195, 196] supplemented by Pu(IV) measurements [208] [209], an increase of Pu(IV) concentrations above the values given for the NaCl system are not expected.

In the range $6 \leq pH_m \leq 9$, the concentration of tetravalent Pu(IV) species in contact with a Pu(IV) solid is estimated to 10^{-8} M.

Pu(V) solubility in the $MgCl_2$ system

The estimation of the Pu(V) solubility in 4.5 M $MgCl_2$ solution is following [204]. The Pu solubility is $10^{-5.5}$ M at pHm 6 and 10^{-8} M at pHm 9, respectively.

6.6 Technetium

Under oxidizing or redox neutral conditions technetium exists as anionic pertechnetate TcO_4^- species in aquatic solutions. In the case of a reducing chemical environment, Tc is reduced and transforms into the tetravalent oxidation state. In the scope of the OECD-NEA Thermodynamic Database Project thermodynamic data and solubility data have been reviewed [19].

NaCl and $MgCl_2$ systems

According to the present knowledge, TcO_4^- solubility is not controlled by a solid phase in NaCl and $MgCl_2$ solutions under oxidizing conditions. Therefore, no solubility limit can be derived. Under reducing conditions, a solid TcO_2xH_2O(am) phase exists. Investigations by Meyer et al. [210] and Eriksen et al. [211] on the solubility of TcO_2xH_2O(am) are discussed in [212]. Similar to the behavior of thorium, Tc(IV) shows a concentration plateau at 10^{-8} M in the pH_m range between 3 and 10. This plateau is controlled by uncharged $Tc(IV)(OH)_4$(aq) complexes subject to only weak ion-interaction processes and showing a tendency to form intrinsic colloids. The concentration of such colloids would be around 10^{-6} M in analogy to the well-investigated Th(IV) system. The Tc(VII) concentration in both carbonate free NaCl and $MgCl_2$ solutions is not limited by solubility. Tc(IV) solubility is estimated in the range of 10^{-6} M.

6.7 Selenium

Selenium is very redox sensitive element. It can exist in aquatic solutions in four different redox states, such as hexavalent selenate (SeO_4^{2-}), tetravalent selenite (SeO_3^{2-}), selenide (Se^{2-}), and in metallic form (zero valent Se°). A full review of the chemical thermodynamics of selenium in aqueous/solid systems has recently been presented by the NEA-TDB project [213].

Investigations of the behavior of Se in saline systems are currently being performed within the VESPA project. Solubility limits are not estimated for saline systems, at present.

6.8 Zirconium

In aqueous solution, Zr exists in the tetravalent oxidation state. Zr(IV) concentrations are estimated to be similar to analogous Th(IV) data, as similar solid oxy-hydroxide phases ($Zr(OH)_4$(am)) precipitate from solution and also the aqueous speciation under the given conditions will be dominated by similar charge-neutral aqueous tetrahydroxide species. Consequently, the estimated Zr concentrations for the given boundary conditions are at 10^{-6} M.

6.9 Rare earth elements

Rare earth elements (REE) are present in the radioactive waste either as fission products or in the case of gadolinium as component of the control rods or as homogeneous neutron poisons. The REE (lanthanides) exist mainly in the trivalent oxidation state and have comparable solubility and aquatic speciation as Am and Cm. The REE Nd is used as analogue for Am and has been studied extensively also at high ionic strength conditions. From this analogy, the solubility of REE can be estimated under the assumption that only trivalent ions are present.

It should be noted, that the different trivalent rare earth elements and trivalent actinides are treated separately with each element contributing fully to its respective source term. However, if these elements will in fact exhibit nearly identical solubility behavior and solid phase characteristics, it can be imagined that the solubility limitation refers to the sum of these elements. In this case, the individual concentrations of the REE(III) and An(III) source term concentrations would be lower than the overall solubility limit, according to their relative abundance.

6.10 Summary of the solubility data

In the previous chapters, thermodynamic solubility of some elements is reported as shown in Tab. XVIII for the pH_m range $6 \leq pH_m \leq 9$. These data are relevant for pure radionuclide solution systems. In the case of the presence of solid materials, sorption processes will take place and change the observed concentrations to lower values under many conditions. As soon as radionuclides are transported away from the source, they certainly will undergo sorption to surfaces of container corrosion product, backfill material etc., which will decrease their concentrations in the near field and lower radionuclide transport. It should be emphasized, that the radionuclide concentrations given below are only relevant for the scenario detailed above. The concentrations depend on the geochemical boundary conditions and cannot be generalized independent of the geochemical conditions.

Tab. XVIII Solubility controlled element concentrations in the relevant pH_m range.

	5 M NaCl pH_m 6, (M)	5 M NaCl pH_m 9, (M)	4.5 M $MgCl_2$ pH_m 6, (M)	4.5 M $MgCl_2$ pH_m 9 (M)
Am(III)	$>10^{-1}$	10^{-5}	$>10^{-1}$	$10^{-4.5}$
Th(IV)	10^{-6}	10^{-6}	10^{-6}	10^{-6}
U(IV)	10^{-6}	10^{-6}	10^{-6}	10^{-6}
U(VI)	$10^{-4.5}$	$10^{-6.5}$	$>10^{-2}$	$10^{-5.5}$
Np(IV)	$10^{-6.5}$	$10^{-6.5}$	$10^{-6.5}$	$10^{-6.5}$
Np(V)	$>10^{-1}$	$10^{-3.5}$	$>10^{-1}$	10^{-3}
Pu(III)	$>10^{-4}$	10^{-8}	$>10^{-2.5}$	10^{-8}
Pu(IV)	10^{-8}	10^{-8}	10^{-8}	10^{-8}
Pu(V)	$10^{-5.5}$	10^{-8}	$10^{-5.5}$	10^{-8}
Zr(IV)	10^{-6}	10^{-6}	10^{-6}	10^{-6}
Tc(IV)	10^{-6}	10^{-6}	10^{-6}	10^{-6}
Tc(VII)	$>10^{-1}$	$>10^{-1}$	$>10^{-1}$	$>10^{-1}$
Se	solubility not estimated			

- The solubility of Am(III) is above $10^{-4.5}$ M for $pH_m < 9$.
- The U(VI) concentration in the NaCl System under oxidizing conditions is estimated between $10^{-4.5}$ M for pH_m 6 and $10^{-6.5}$ M at pH_m 9. Under reducing conditions U(IV) behaves similar to thorium. The solubility will be controlled by a solid UO_2xH_2O(am) phase. The U(IV) solubility in NaCl and $MgCl_2$ solutions is estimated in the range of 10^{-6} M.

- The Np(V) concentration in the pH_m range < 9 in NaCl solutions is above $10^{-3.5}$ M. The Np(IV) concentration in NaCl and $MgCl_2$ systems is estimated to $10^{-6.5}$ M.
- The Pu(III) concentration in NaCl system in the range $6 \leq pH_m \leq 9$ is well established for diluted solutions. For saturated NaCl solutions, in the relevant pH_m range from $6 \leq pH_m \leq 9$, solubility of Pu(III) would be between 10^{-4} M and 10^{-8} M. However, solid Pu(III) is transformed to Pu(IV) with a solubility of 10^{-8} M in the relevant pH range. The Pu(III) concentration in the carbonate free $MgCl_2$ system ranges from above $10^{-2.5}$ M at pH_m 6 and 10^{-8} M at pH_m 9. The concentration of Pu in contact with a Pu(IV) solid is estimated at 10^{-8} over the considered pH range.
- The Tc(VII) concentration in both solutions is not limited by solubility. Tc(IV) solubility is estimated in the range of 10^{-6} M.

6.11 Application to the preliminary safety analysis for Gorleben

The void volume of the disposal drifts per canister is required to estimate the maximum concentrations of each radionuclide given by the inventory. An average cross section of 17 m^2 is assumed for these drifts. Depending on the degree of backfill compaction, different volumes of brine may interact with the canister material or with the wastes. Based on disposal concept B1 (Pollux-10) [65], expected void volumes are calculated and compared to the inventory of heavy metal and steel (see Tab. XIX). The internal void volume of the canisters is taken into account. The average void volume in SNF disposal drifts is given in Tab. XIX for two degrees of backfill compaction.

Tab. XIX Average void volume in spent nuclear fuel disposal drifts for two degrees of backfill compaction, calculated from data of WP 5 [65].

	Initial state	Final state	Units
Porosity of backfill	35	1	%
Void volume per canister	45.5	2.0	m^3
Ratio $\frac{mass\ of\ heavy\ metal}{void\ volume}$	0.12	2.67	kg dm^{-3}
Ratio $\frac{mass\ of\ steel\ (Fe)}{void\ volume}$	1.30	28.4	kg dm^{-3}
Mass of heavy metal (U)	5610 (BWR) 5420 (PWR)		kg
Mass of steel (Fe)	57560		kg

According to the "Safety Requirements Governing the Final Disposal of Heat-Generating Radioactive Waste", manageability of the waste containers must be guaranteed for a period of 500 years [1] which implies a "lifetime" of the containers of 500 years. The crushed salt backfill will be compacted significantly within this time period and a porosity of the crushed salt of 1 vol.% (final state) is assumed. Under this assumption, the maximum total void volume is 2 m^3 per Pollux canister. Using the calculated yields of fission products and actinides in spent nuclear fuel, the load of a canister (mass of heavy metal) and the void volume per canister, a maximum "inventory controlled" concentration (assuming complete dissolution of the inventory) can be calculated (Tab. XX). This concentration is then compared to the solubility limits to assess whether final concentrations will be controlled by the RN-inventory or by solubility limits. Water will also be consumed by iron corrosion processes; however, this is not taken into account in Tab. XX.

Tab. XX Concentrations based on the inventory and the void volume in a disposal drift for SNF.

●: Thermodynamic solubility < inventory controlled concentration
○: Thermodynamic solubility > inventory controlled concentration or no data available

Element	**mass in SNF**	**mass per canister**	**inventory controlled conc. (max)**	**NaCl pH_m = 6**	**NaCl pH_m = 9**	**MgCl2 pH_m = 6**	**MgCl2 pH_m = 9**
	mol/t	mol	mol dm^{-3}	mol	mol	mol	mol
He				gas	gas	gas	gas
C				-	-	-	-
Fe*				●	●	●	●
Co*				○	○	○	○
Ni*				○	○	○	○
Se	0.920	5.16E+00	2.58E-03	○	○	○	○
Rb	6.127	3.44E+01	1.72E-02	○	○	○	○
Sr	5.495	3.08E+01	1.54E-02	○	○	○	○
Y	7.335	4.11E+01	2.06E-02	○	●	○	●
Zr	64.130	3.60E+02	1.80E-01	●	●	●	●
Nb	0.0025	1.42E-02	7.11E-06	○	○	○	○
Mo	50.581	2.84E+02	1.42E-01	●	●	●	●
Tc	11.500	6.45E+01	3.23E-02	●	●	●	●
Ru	30.609	1.72E+02	8.59E-02	○	○	○	○
Rh	6.011	3.37E+01	1.69E-02	○	○	○	○
Pd	11.334	6.36E+01	3.18E-02	○	○	○	○
Ag	0.627	3.52E+00	1.76E-03	○	○	○	○
Cd	1.009	5.66E+00	2.83E-03	○	○	○	○
In	0.0255	1.43E-01	7.15E-05	○	○	○	○
Sn	0.763	4.28E+00	2.14E-03	○	○	○	○
Sb	0.148	8.30E-01	4.15E-04	○	○	○	○
Te	3.247	1.82E+01	9.11E-03	○	○	○	○
I	2.391	1.34E+01	6.71E-03	○	○	○	○
Xe	56.911	3.19E+02	1.60E-01	gas	gas	gas	gas
Cs	16.283	9.13E+01	4.57E-02	○	○	○	○
Ba	30.344	1.70E+02	8.51E-02	○	○	○	○
La	12.890	7.23E+01	3.62E-02	○	●	○	●
Ce	25.220	1.41E+02	7.07E-02	○	●	○	●
Pr	11.790	6.61E+01	3.31E-02	○	●	○	●
Nd	39.447	2.21E+02	1.11E-01	○	●	○	●
Sm	8.216	4.61E+01	2.30E-02	○	●	○	●
Eu	1.395	7.82E+00	3.91E-03	○	●	○	●
Gd	1.754	9.84E+00	4.92E-03	○	●	○	●
Ra	5.75E-04	3.22E-03	1.61E-06	○	○	○	○
Ac				○	○	○	○

Element	mass in SNF	mass per canister	inventory controlled conc. (max)	NaCl $pH_m = 6$	NaCl $pH_m = 9$	MgCl2 $pH_m = 6$	MgCl2 $pH_m = 9$
	mol/t	mol	mol dm^{-3}	mol	mol	mol	mol
Th	0.0457	2.56E-01	1.28E-04	●	●	●	●
Pa	1.88E-04	1.05E-03	5.25E-07	○	○	○	○
U	3916.086	2.20E+04	1.10E+01	●	●	●	●
Np	10.190	5.72E+01	2.86E-02	●	●	●	●
Pu	38.372	2.15E+02	1.08E-01	●	●	●	●
Am	4.157	2.33E+01	1.17E-02	○	●	○	●
Cm	0.0144	8.06E-02	4.03E-05	○	●	○	○

* inventory in canister material

7 Radionuclide retention by sorption

The radionuclide concentrations listed in Tab. XVIII or calculated from the total inventory divided by the relevant brine volume represent upper limits of radionuclide concentrations. During the interactions of solutions with the waste forms, a multitude of coupled geochemical reactions take place. These reactions are complex, but by application of chemical principles, they can be reduced to few basic processes.

- The radionuclide concentrations are the highest directly in the waste containers. Mobilization will always lead to a dilution.
- The primarily released radionuclides from the waste forms undergo various reactions depending on the geochemical environment. These reactions include hydrolysis, redox and complexation reactions as well as the formation of eigen-colloids or the attachment to pseudo colloids. The radionuclides are present as ions, complexes or colloidal species. They may react with solid surfaces by adsorption, chemical sorption, ionic exchange, or by incorporation in newly formed solids in the case of super saturation. Simultaneously corrosion of waste forms and re-mineralization reactions occur, which influence the geochemical environment and consequently effect the solubility and sorption of radionuclides.
- Sorption reactions are considered in competition with dissolution/precipitation reactions. By the different reactions, a geochemical system will always tend to approach an energetically favored state in the long term. This may lead to dissolution of primary solids and transfer the radionuclides in more stable sorption phases. Dissolution/precipitation reactions can be described by thermodynamic / geochemical modeling. For sorption processes, especially in highly saline solutions, neither sorption models nor the required data bases exist presently. For this reason, it is assumed that either a thermodynamically well defined solid is formed or that sorption phases control the concentration of the element under consideration. For source term considerations, this statement is relevant for elements/radionuclides of high abundance: If radionuclide bearing solids can be formed, the concentrations are defined by the solubility of the solids, whereas otherwise, the concentrations are controlled by sorption onto the available surfaces.

Various solid phases with different surface sizes and properties are present in the near-field. Prominent solids are the corrosion products of the waste forms, the corrosion products of the canisters, backfill materials and the natural rock salt. Sorption coefficients Rs are used frequently within source term modeling to assess the influence of sorption processes.

$$Rs = \frac{concentration\ of\ the\ element\ in\ the\ solid\ phase}{concentration\ of\ the\ element\ in\ the\ solution} \qquad \text{eq. 14}$$

Very few data exist, showing sorption onto natural rock salt. Tab. XXI shows unpublished data measured at INE [214].

Tab. XXI Sorption coefficient of some fission products onto solid NaCl in contact with saturated NaCl and Q-brine [214].

	Rs / cm³·g⁻¹	
Isotope	**sat. NaCl**	**Q brine**
^{85}Sr	0.15	0.17
^{99}Tc	0.1	0.2
^{137}Cs	0.2	0.2

The sorption coefficients onto ERAM rock salt were measured for some of the actinides [215].

Tab. XXII Sorption coefficient of actinides onto solid NaCl from ERAM in contact with saturated NaCl and Q-brine [215]

	Rs / cm³·g⁻¹	
Isotope	**sat. NaCl**	**Q brine**
Pu	301	20
Th	85	135
Np	71	0.2
U		0.4

The salt samples used in Tab. XXI and Tab. XXII may be different from the rock salt at the Gorleben salt dome. Therefore the sorption properties need to be rechecked. If other backfill materials or additions to the backfill materials are considered, the sorption coefficients of these materials have to be determined.

8 Summary and outlook

A radionuclide source term for HLW glass, spent nuclear fuel and CSD-C waste has been derived in this study. The study outlines that it is possible to derive a radionuclide source term for geochemical systems of interest as long as the fundamental geochemical processes are understood, the properties of HLW and other near-field components are sufficiently characterized and the knowledge on the specific properties of relevant radionuclide species are known. As has been described explicitly in the above text, the preliminary and rough definition of the envisioned waste inventory and other near-field constituents lead to simplifications and model assumptions relevant for the source term. These simplifications and assumptions were made to derive a source term for the scenarios considered in this study. As a consequence, the source term needs refinements for a future safety analysis.

The radionuclide source term (dissolution of waste forms, solubilities, etc.) is significantly influenced by **geochemical boundary conditions**, such as brine composition, pH, redox species, temperature and relevant minor components of the system. Better information on the disposal concept (inventories and temporal evolution), will help to establish a more comprehensive definition of the geochemical boundary conditions. The robustness of the geochemical conditions can be optimized by applying tailored engineered barrier materials buffering the pH. Especially for the low pH range pH_m ~ 6, there is almost no effective solubility limitation. As a consequence, it would be beneficial for safety considerations, to buffer the pH_m in a neutral to slightly alkaline region around pH_m 9. This could be easily achieved by addition of magnesium hydroxide or Sorel-based backfill materials.

The international discussion concerning **HLW glass** under disposal conditions refers to the combination of the various mechanisms and processes resulting in a time-dependent glass corrosion rate. This rate influences the radionuclide source term especially for easily soluble elements. Some related mechanisms have the potential to alter the performance of the glass. This is the case for the cementation of fissures by alteration products and the retention of radionuclides in the gel. These retention processes can presently not be quantified unambiguously and will be neglected. The study of natural analogs (natural glasses) can help to determine the long term relevance of certain mechanisms. Such studies have been used to document the transition of glass gel to clay minerals [216-218]. However, reliable rates cannot be derived from natural analog studies. An important key mechanism relates to the role of the gel in the decrease of the glass corrosion rate with time. Some authors assume that the rate decrease is mainly due to the formation of a protective gel, whereas other authors assume that water diffusion and ion exchange are more important for the rate decrease and the long term rate. This was discussed within the GLAMOR project (2001-2004) [219]. The final conclusions of this project are as follows: "*There is agreement that the decrease of the corrosion rate of glass is due to both an affinity effect (Si saturation), and a kinetic effect caused by the condensation and diffusion of Si in the gel layer. There is agreement that there needs to be a mathematical coupling between affinity driven glass dissolution and mass transfer through the gel. There is no conclusion on the relative importance of these two mechanisms and, as a consequence, on their parameterization in the models. However the evidence of a residual corrosion rate has increased, and there is a consensus about its importance. There are also indications that water diffusion affects the rate decrease, and the residual rate (along with other mechanisms such as precipitation of secondary phases). It is recommended to elaborate a more complete documentation (values, uncertainties) of the various input parameters that are used in the models.*"

With respect to the IRF from **spent nuclear fuel** pessimistic estimate values exist. Values for the fast / instant release fraction of ^{14}C, ^{36}Cl, ^{135}Cs, ^{129}I, ^{79}Se and ^{99}Tc are still largely unknown and are represented by bounding values. Ongoing research (Euratom 7th FP CP FIRST-Nuclides, www.firstnuclides.eu) improves the knowledge and data and reduces uncertainties also providing for realistic data on the relevant radionuclide release for the Safety Case. A physico-chemical mechanism for the radiation induced spent nuclear fuel matrix dissolution was developed in the past decade.

The effect of H_2 in lowering the potentially oxidizing effect of radiolysis is known for relatively simple solutions, e.g. concentrated NaCl. There are indications that redox-sensitive radionuclides (such as Np, Pu, U and Tc) are precipitated in the close vicinity of the spent nuclear fuel under (strongly) reducing conditions. This retention process is not considered in this study.

With respect to **basic thermodynamics and solubility**, it should be noted that the radionuclide concentrations derived in this study are relevant for the considered simplified scenario and geochemical boundary conditions. If a more refined scenario is derived, this must also be reflected in updated predictions of the geochemical conditions, and hence a refined discussion of radionuclide solubility limits under the resulting geochemical boundary conditions will be required. This is notably true if a new scenario involving significant amounts of carbonate is considered relevant. The assessment of human intrusion scenarios, leading to a disturbance of the expected reducing conditions, will result in drastically changed geochemical boundary conditions. Under conditions of air contacting the waste, oxidizing conditions will prevail and CO_2 from the atmosphere will lead to considerable carbonate concentrations at high pH conditions. A totally new source term will be needed for this scenario.

Estimations of solubility limitations are only relevant for cases where solubility limits are expected to be below the respective radionuclide inventories for a given set of geochemical boundary conditions and precipitation reactions can therefore be expected to promote radionuclide retention. The potentially solubility controlled elements will strongly depend on the specific scenario analyzed (i.e. amount of water, geochemical boundary conditions). Formation of radionuclide bearing secondary phases (also solid solutions) is expected to lead to decreasing solubility limits. This process contributes to radionuclide retention and is not considered in the source term.

Sorption processes can decrease radionuclide concentrations in solution relative to the thermodynamic solubility limits under many conditions. For low ionic strength systems, a detailed understanding of many key sorption processes has been achieved. For concentrated brine conditions, similar effects are known to exist, however many of them are still lacking a reliable quantification or fundamental scientific process understanding. Sorption and reduction of U(VI) onto steel corrosion products have been observed [163]. However, presently it is not possible to quantify the radionuclide retention onto canister corrosion products. The reason is attributed to the fact that the mineralogy of the corrosion products in the salt brines is unclear. Also, the surface properties and the permeability of the corrosion products formed under the confining pressures of the backfilled disposal galleries are not known.

A **thermodynamic database** for modeling actinide solubility in brine conditions is currently integrated into the German THEREDA database project. This is certainly a scientifically challenging and demanding task. The experimental studies required to complete THEREDA database to fill important data gaps will clearly also require additional and dedicated research efforts.

In the following, a list of open questions, mostly related to the geochemical behavior of HLW and aquatic chemistry of released radionuclides is discussed. A more detailed analysis of these questions would reduce uncertainties**. T**wo different types of open questions are identified which are attributed to

(1) parameters resulting from present state of the design/layout and closure concept of the disposal and

(2) unsatisfactory knowledge of geochemical processes, mechanisms and data.

Design/layout and closure concept of the disposal

- The source term comprises a generic study. For a future safety analysis, more detailed information on the fuel load of the canisters are required, such as the type of fuel / fuel elements, initial enrichments, burn-ups, presence of neutron poisons as absorber rods or burnable poisons.

- The geochemical boundary conditions depend on the disposal concept. With respect to optimization, types and design of canisters, emplacement technology as well as kind and type of backfill, its behavior and compaction should be evaluated with respect to the geochemical conditions and the related radionuclide source term. Assessment of temporal evolution and spatial distribution of the geochemical conditions in particular chemical buffering of pH and redox potential is required.

- Rock salt considered as backfill material has a very limited sorption capacity for radionuclides. Specific additions to the backfill (thermodynamically stable materials such as Sorel cements) can improve the sorption potential for radionuclides and increase radionuclide retention.

- For the waste forms considered in this study, the use of materials based on Portland cement is not recommended. In the case of the penetration of small quantities of $MgCl_2$-rich solutions, the pH may rise accompanied by an increase of $[Ca^{2+}]$ due to Ca-Mg exchange reactions. This may lead to the formation of calcium stabilized actinide complexes at elevated Ca^{2+}-concentrations that are associated to highly alkaline pH values.

Research on geochemical processes, mechanisms and data

<u>HLW glass:</u>

- Iodine (^{129}I) is one of the elements relevant for the long-term dose rate. It is assumed that a certain percentage of the initial inventory remains in the HLW glass. However, during spent nuclear fuel reprocessing and the subsequent vitrification, iodine may have been released. Measurement of the ^{129}I concentration in the HLW glass could provide a realistic value and reduce conservative estimations.

<u>Spent LWR fuel:</u>

- Following issues are of particular importance for the evaluation of the instant release fraction (IRF):
    - Experimental data on the dependency of the fast / instant release processes on temperature.

  - IRF measurements for MOX fuel.
- A mechanistic description of the dose threshold for the transition of radiolysis induced to solubility controlled matrix dissolution needs to be developed.
  - Additional spent nuclear fuel corrosion experiments are needed at elevated temperature conditions in particular under (strongly) reducing conditions, i.e. in hydrogen-saturated iron-rich systems.
  - Experimental data on spent MOX fuel dissolution are required under strongly reducing conditions.

CSD-C waste:

- Corrosion rates / RN mobilization rates need to be provided.
- Release of ^{14}C and its speciation needs to be quantified.

Basic thermodynamics and solubility:

- Estimated solubility limits are not provided in the present study if experimental data for a particular element are not available.
- Interactions of radionuclides (and waste form components) with minor components of the geochemical system, such as HS^-, borate, organics etc. need to be included for an improved source term estimation.
- The temperature dependences of the formation of aquatic and solid radionuclide phases need to be studied further.
- Redox processes as function of the temperature need to be quantified, especially for actinides.

Sorption processes:

- Improved characterization and quantification of sorption processes under high ionic strength conditions is needed in order to include this retention mechanism in source term estimations.
- Temperature dependent sorption studies are required to assess sorption processes under elevated temperature conditions.

In this study the concentrations of hydrocarbons and possible related reactions are not explicitly analyzed or quantified. The presence of hydrocarbons in the Gorleben salt formation may lead to the formation of sulfides and carbonates in the near-field environment. These reactions might also be influenced by microbial activities. Information on microbial populations, biological activities, and behavior under the temperature conditions of HLW and the expected strongly reducing geochemical conditions are missing.

Furthermore, human intrusion scenarios are not addressed: Human intrusion might change the geochemical boundary conditions significantly. Drilling into the disposal level will release hydrogen to the atmosphere and may deliver oxygen and CO_2 gas to the disposal level.

9 References

[1] Bundesministerium für Umwelt, N.u.R.B. (2010), Sicherheitsanforderungen an die Endlagerung wärmeentwickelnder radioaktiver Abfälle. Bundesministerium für Umwelt, Naturschutz und Reaktorsicherheit (BMU). p. 22.

[2] Grambow, B. (1998), Beschreibung der kinetischen Barrierenwirkung von HAW-Glas im integrierten Nahfeldmodell, in *Erstellung eines integrierten Nahfeldmodells von Gebinden hochaktiver Abfälle im Salzstock Gorleben: geochemisch fundierter Quellterm für HAW-Glas, abgebrannte Brennelemente und Zement*. Institut für Nukleare Entsorgung (INE), Forschungszentrum Karlsruhe, Karlsruhe: **FZK-INE 015/97**.

[3] Bernotat, W., H. Geckeis, et al. (2000), Quellterme für HAW-Glas, abgebrannten Kernbrennstoff und zementierte Abfälle: HAW-Glas: Auslaugverhalten und Freisetzung von Radionukliden, in *Erstellung eines integrierten Nahfeldmodells von Gebinden hochaktiver Abfälle im Salzstock Gorleben: geochemisch fundierter Quellterm für HAW-Glas, abgebrannte Brennelemente und Zement*. Institut für Nukleare Entsorgung (INE), Forschungszentrum Karlsruhe, Karlsruhe: **FZK-INE 007/99**.

[4] GRS (2010), Vorläufige Sicherheitsanalyse für den Standort Gorleben - Beschreibung des Arbeitsprogramms.

[5] Grambow, B. and R. Muller (2001), First-order dissolution rate law and the role of surface layers in glass performance assessment. *Journal of Nuclear Materials* **298** (1-2): 112-124.

[6] Grambow, B., K. Lemmens, and Y. Minet (2008), NF-PRO Final Synthesis Report on RTD Component 1: Dissolution and release from the waste matrix, in *6th Framework Programme Integrated Project NF-PRO*. SCK–CEN, Brussels, B.

[7] Grambow, B., A. Loida, et al. (1997), Long-term safety of radioactive waste disposal: Chemical reaction of fabricated and high burnup spent UO2 fuel with saline brines. Final Report: **EUR 17111**.

[8] Grambow, B., A. Loida, et al. (2000), Long-term safety of radioactive waste disposal: Source term for performance assessment of spent fuel as a waste form. Final Report. Forschungszentrum Karlsruhe: **FZKA 6420**.

[9] Grambow, B., A. Loida, and E. Smailos (1998), Long-term stability of spent nuclear fuel waste packages in Gorleben salt repository environments. *Nuclear Technology* (121): 174-188.

[10] Grambow, B., M. Kelm, B. Kienzler, and A. Loida (1999), Quellterme für HAW-Glas, abgebrannten Kernbrennstoff und zementierte Abfälle: Abgebrannter LWR-Kernbrennstoff: Auslaugverhalten und Freisetzung von Radionukliden, in *Erstellung eines integrierten Nahfeldmodells von Gebinden hochaktiver Abfälle im Salzstock Gorleben: geochemisch fundierter Quellterm für HAW-Glas, abgebrannte Brennelemente und Zement*. Institut für Nukleare Entsorgung (INE), Forschungszentrum Karlsruhe, Karlsruhe: **FZK-INE 009/99**.

[11] Loida, A., B. Luckscheiter, and B. Kienzler (1999), Quellterme für HAW-Glas, abgebrannten Kernbrennstoff und zementierte Abfälle: Korrosionsverhalten von HAW Glas und abgebranntem Kernbrennstoff in Gorlebenlauge (FZK-INE 012/99), in *Erstellung eines integrierten Nahfeldmodells von Gebinden hochaktiver Abfälle im Salzstock Gorleben: geochemisch fundierter Quellterm für HAW-Glas, abgebrannte Brennelemente und Zement*. Institut für Nukleare Entsorgung (INE), Forschungszentrum Karlsruhe

[12] Poinssot, C., C. Ferry, et al. (2005), Spent fuel stability under repository conditions - final report of the European project. CEA, Saclay, France, Saclay.

[13] Grambow, B., J. Bruno, et al. (2010), Final Report of the Project MICADO: Model uncertainty for the mechanism of dissolution od spent fuel in nuclear waste repository.

[14] Neeb, K.-H. (1997). The radiochemistry of nuclear power plants with light water reactors. Berlin, de Gruyter.

[15] Mc Stocker, B., F. Peiffer, et al. (2011), AP3: Abfallspezifikation und Mengengerüst (Bericht für Arbeitspaket 3, Vorläufige Sicherheitsanalyse Gorleben), GRS, Editor, Köln.

[16] Grenthe, I., J. Fuger, et al. (1992). Chemical Thermodynamics of Uranium, North Holland Publisher.

[17] Guillaumont, R., T. Fanghänel, et al. (2003). Update on the Chemical Thermodynamics of Uranium, Neptunium, Plutonium, Americium and Technetium, Elsevier Science.

[18] Lemire, R.J. (2001). Chemical Thermodynamics of Neptunium and Plutonium, Elsevier Science.

[19] Rard, J.A., M.H. Rand, G. Anderegg, and H. Wanner (1999). Chemical Thermodynamics of Technetium, Elsevier Science.
[20] Silva, R.J., G. Bidoglio, et al. (1995). Chemical Thermodynamics of Americium, Elsevier Publisher.
[21] Rand, M., J. Fuger, et al. (2008). Chemical Thermodynamics of Thorium. Paris, OECD Publications.
[22] Pitzer, K.S. (1991). Activity coeeficients in electrolyte solutions. Boca Raton, Fl., USA, CRC Press, Inc.
[23] Kienzler, B., M. Altmaier, V. Metz, and C. Bube (2010). Zusammenstellung von Daten zur wissenschaftlich belastbaren Abschätzung potentieller Strahlenexpositionen in der Umgebung der Schachtanlage Asse II, Institut für Nukleare Entsorgung (INE).
[24] Choppin, G.R. (1983), Solution Chemistry of the Actinides. *Radiochim. Acta* **32**: 43
[25] Choppin, G.R. and E.N. Rizkalla (1994), Solution chemistry of actinides and lanthanides, in *Handbook on the Physics and Chemistry of Rare Earths*, Gschneidner K.A.Jr and L. Eyring, Editors. North Holland: Amsterdam. p. 559.
[26] Baes, C.F., Jr. and R.E. Mesmer (1976). The hydrolysis of cations. New York, Wiley.
[27] Grenthe, I. and I. Puigdomenech (1997), Modelling in Aquatic Chemistry. Nuclear Energy Agency: Paris, F.
[28] Neck, V. and J.I. Kim (2000), An electostatic approach for the prediction of actinide complexation constants with inorganic ligands - Application to carbonate complexes. *Radiochim. Acta* **88**: 815-822.
[29] Neck, V., M. Altmaier, et al. (2003), Teil 3: Löslichkeitsexperimente zur Absicherung der thermodynamischen Datenbasis, in *Experimentelles Programm zur Bestätigung der Ergebnisse von standortspezifischen Modellrechnungen für die Schachtanlage Asse*. FZK-INE, Karlsruhe: **FZK-INE 007/03**.
[30] Kienzler, B. and A. Loida (2001), Endlagerrelevante Eigenschaften von hochradioaktiven Abfallprodukten. Charakterisierung und Bewertung. Empfehlung des Arbeitskreises HAW-Produkte. Forschungszentrum Karlsruhe: **FZKA 6651**.
[31] Peuget, S., V. Broudic, et al. (2007), Effect of alpha radiation on the leaching behaviour of nuclear glass. *Journal of Nuclear Materials* **362** (2-3): 474-479.
[32] Kienzler, B. (1989). Cooling and Cracking of Technical HLW Glas Products: Experimental and Numerical Studies. Mat. Res. Soc. Symp., Materials Research Society, **127**, 191 - 198.
[33] Grambow, B., A. Loida, et al. (1996), Long-term safety of radioactive waste disposal: Chemical reaction of fabricated and high burnup spent UO_2 fuel with saline brines. Final Report. Forschungszentrum Karlsruhe: **FZKA 5702**.
[34] Grambow, B., W. Lutze, et al. (1996), Long-Term Safety of Radioactive Waste Disposal. Retention of Pu, Am, Np and Tc in the Corrosion of COGEMA Glass R7T7 in Salt Solutions. Final Report. Forschungszentrum Karlsruhe: **FZKA 5767**.
[35] Aagaard, P. and H.C. Helgeson (1982), Thermodynamic and Kinetic Constraints on Reaction-Rates among Minerals and Aqueous-Solutions .1. Theoretical Considerations. *American Journal of Science* **282** (3): 237-285.
[36] Murphy, W.M., E.H. Oelkers, and P.C. Lichtner (1989), Surface-reaction versus diffusion control of mineral dissolution and growth-rates in geochemical processes. *Chemical Geology* **78** (3-4): 357-380.
[37] Ricol, S. (1995), Etude du gel d'altération des verres nucléaires et synthèse de gels modèles. University of Paris XI, Orsay, France.
[38] Luckscheiter, B., B. Kienzler, and D. Bosbach (2004), Literaturstudie zum Korrosionsverhalten von HAW-Gläsern in Ton: Tongestein und Versatz-Material. Forschungszentrum Karlsruhe: **FZKA 7068**.
[39] Bruno, J. and R.C. Ewing (2006), Spent nuclear fuel. *Elements* **2**: 343-349.
[40] Kleykamp, H., J.O. Paschoal, R. Pejsa, and F. Thümmler (1985), Composition and structure of fission product precipitates in irradiated oxide fuels: Correlation with phase studies in the Mo-Ru-Rh-Pd and BaO-UO2-ZrO2-MoO2 systems. *Journal of Nuclear Materials* **130**: 426-433.
[41] Cui, D., J. Low, C.J. Sjöstedt, and K. Spahiu (2004), On Mo-Ru-Tc-Pd-Rh-Te alloy particles extracted from spent fuel and their leaching behaviour under Ar and H2 atmospheres. *Radiochimica Acta* **92**: 551-555.
[42] He, H., P.G. Keech, et al. (2007), Characterization of the influence of fission product doping on the anodic reactivity of uranium dioxide. *Canadian Journal of Chemistry* **85**: 702-713.

[43] González-Robles Corrales, E. (2011), Study of Radionuclide Release in commercial UO2 Spent Nuclear Fuel - Effect of Burn-up and High Burn-up Structure. . Universitat Politècnica de Catalunya, Barcelona, Spain.

[44] Kleykamp, H. (1988), The chemical state of the fission products in oxide fuels. *Journal of Nuclear Materials* **131**: 221-246.

[45] Johnson, L.H., N. Garisto, and S. Stroes-Gascoyne (1985). Used-fuel dissolution sudies in Canada. Waste Management 1985 Tucson, Arizona, March 24-28, WM Symposia Inc., **85**, 479-482.

[46] Poinssot, C., C. Ferry, et al. (2005), Spent fuel radionuclide source term model for assessing spent fuel performance in geological disposal. Part II: Matrix alteration model and global performance. *Journal of Nuclear Materials* **346**: 66-77.

[47] Hobbs, L.W., C.J. F.W., S.J. Zinkle, and R.C. Ewing (1994), Radiation effects in ceramic. *Journal of Nuclear Materials* **216**: 291-321.

[48] Grambow, B., L.O. Werme, R.S. Forsyth, and J. Bruno (1990), Constraints by experimental data for modelling of radionuclide release from spent fuel. *Proceedings of the International Symposium on the Scientific Basis for Nuclear Waste Management, Materials Research Society* **176**: 465-474.

[49] Loida, A., B. Grambow, and H. Geckeis (2001), Congruent and incongruent radionuclide release during matrix dissolution of partly high burnup spent fuel. *Proceedings of the 24th International Symposium on the Scientific Basis for Nuclear Waste Managment, Materials Research Society* **Mat. Res. Symp. Proc. Vol. 663**: 414-426.

[50] Hanson, B.D. and R.B. Stout (2004). Reexamining the dissolution of spent fuel: A comparison of different methods for calculating rates. Scientific Basis for Nuclear Waste Management XXVIII, San Francisco (USA), Materials Research Society, **824**, 89-94.

[51] Bailly, H., D. Ménessier, and C. Prunier (1999). The nuclear fuel of pressurized water reactors and fast neutron reactors: Design and behaviour. Paris, Lavoisier Publishing.

[52] Kelm, M. and E. Bohnert (2004), A kinetic model for the radiolysis of chloride brine, its sensitivity against model parameters and a comparison with experiments. Forschungszentrum Karlsruhe: **FZKA 6977**.

[53] Spahiu, K., L. Werme, and U.B. Eklund (2000), The influence of near field hydrogen on actinide solubilities and spent fuel leaching. *Radiochimica Acta* **88** (9-11): 507-511.

[54] Spahiu, K., D.Q. Cui, and M. Lundstrom (2004), The fate of radiolytic oxidants during spent fuel leaching in the presence of dissolved near field hydrogen. *Radiochimica Acta* **92** (9-11): 625-629.

[55] Kelm, M. and E. Bohnert (2005), Gamma radiolysis of NaCl brine: Effect of dissolved radiolysis gases on the radiolytic yield of long-lived products. *Journal of Nuclear Materials* **346**: 1-4.

[56] Metz, V., E. Bohnert, et al. (2007). γ-radiolysis of NaCl brine in the presence of UO_2(s): Effects of hydrogen and bromide. MRS Symposium NN: Scientific Basis for Nuclear Waste Management XXX, (in press), Boston, 2006, Materials Research Society.

[57] Metz, V., A. Loida, et al. (2008), Effects of hydrogen and bromide on the corrosion of spent nuclear fuel and gamma-irradiated UO2(s) in NaCl brine. *Radiochimica Acta* **96** (9-11): 637-648.

[58] Kelm, M., V. Metz, et al. (2011), Interaction of hydrogen with radiolysis products in 0.1 and 1.0 molar NaCl solutions – comparing pulse radiolysis experiments with simulations. *Radiation Physics and Chemistry* **80**: 426-434.

[59] Kelm, M. and E. Bohnert (2000), Radiation chemical effects in the near field of a final disposal site - I: Radiolytic products formed in concentrated NaCl solutions. *Nuclear Technology* **129** (1): 119-122.

[60] Kelm, M. and E. Bohnert (2000), Radiation chemical effects in the near field of a final disposal site - II: Simulation of the radiolytic processes in concentrated NaCl solutions. *Nuclear Technology* **129** (1): 123-130.

[61] Braitsch, O. (1971). Salt deposits, their origin and composition. Berlin, Springer Verlag.

[62] Herrmann, A.G. and L.E.v. Borstel (1991), The composition and origin of fluid inclusions in Zechstein evaporites of Germany. *Neues Jahrbuch fuer Mineralogie, Monatshefte* (6): 263-269.

[63] Herrmann, A.G. and B. Knipping (1993), Fluide Komponente als Teile des Stoffbestandes der Evaporite im Salzstock Gorleben. Technische Universität Clausthal.

[64] Ershov, B.G., M. Kelm, et al. (2002), Radiation-chemical effects in the near-field of a final disposal site: role of bromine on the radiolytic processes in NaCl-solutions. *Radiochimica Acta* **90**: 617-622.

[65] Bollingerfehr, W., W. Filbert, C. Lerch, and M. Tholen (2011), AP 5: Endlagerkonzepte (Bericht für Arbeitspaket 5, Vorläufige Sicherheitsanalyse Gorleben), GRS, Editor, Köln.

[66] Johnson, L.H., C. Poinssot, C. Ferry, and P. Lovera (2004), Estimates of the instant release fraction for UO2 and MOX fuel at t=0. NAGRA, Wettingen, Switzerland: **Technical Report 04-08**.

[67] Ferry, C., J.P. Piron, A. Poulesquen, and C. Poinssot (2007). Radionuclides release from the spent fuel under disposal conditions: Re-Evaluation of the Instant Release Fraction. Scientific Basis for Nuclear Waste Management XXXI, Sheffield (UK).

[68] Poinssot, C. and J.-M. Gras (2009). Key scientific issues related to the sustainable management of the spent nuclear fuel in the back-end of the fuel cycle. Scientific Basis for Nuclear Waste Management XXXII, Boston, USA, Mat. Res. Soc. Symp. Proc., **1124**.

[69] Cobos, J., L. Havela, et al. (2002), Corrosion and dissolution studies of UO2 containing alpha-emitters. *Radiochimica Acta* **90** (9-11): 597-602.

[70] Jegou, C., B. Muzeau, et al. (2005), Effect of external gamma irradiation on dissolution of the spent UO2 fuel matrix. *Journal of Nuclear Materials* **341**: 62-82.

[71] Bailey, M.G., L.H. Johnson, and D.W. Shoesmith (1985), The effects of alpha radiolysis of water on the corrosion of UO2. *Corrosion Science* **25**: 233-238.

[72] Gray, W.J. (1998), Spent fuel dissolution rates as a function of burnup and water chemistry. Pacific Northwest National Laboratory, PNNL, Technical Report, PNL-11895, Richland,Washington, USA.

[73] Poinssot, C., C. Ferry, et al. (2006), Mechanisms governing the release of radionuclides from spent nuclear fuel in geological repository: major outcomes of the European Project SFS. *Proceedings of the 29th International Symposium on the Scientific Basis for Nuclear Waste Management* **Mat. Res. Symp. Proc. Vol. 809**.

[74] Rondinella, V.V., H. Matzke, J. Cobos, and T. Wiss (1999). Alpha-radiolysis and alpha-radiation damage effects on UO2 dissolution under spent fuel storage conditions. MRS Symposium QQ: Scientific Basis for Nuclear Waste Management XXII, Boston (USA), Materials Research Society, **556**, 447-454.

[75] Rondinella, V.V., H. Matzke, J. Cobos, and T. Wiss (2000), Leaching behaviour of UO2 containing alpha-emitting actinides. *Radiochimica Acta* **88** (9-11): 527-531.

[76] Sattonnay, G., C. Ardois, et al. (2001), Alpha-radiolysis effects on UO2 alteration in water. *Journal of Nuclear Materials* **288**: 11-19.

[77] Stroes-Gascoyne, S., L.H. Johnson, et al. (1997), Leaching of used CANDU fuel: results from a 19-year leach test under oxidizing conditions. . *Materials Research Society Symposium Proceedings* **465**: 511-518.

[78] Suzuki, T., A. Abdelouas, et al. (2006), Oxidation and dissolution rates of UO2(s) in carbonate-rich solutions under external alpha irradiation and initially reducing conditions. . *Radiochimica Acta* **94**: 567-573.

[79] Kelm, M., V. Metz, et al. (2010), Interaction of hydrogen with radiolysis products in 0.1 and 1.0 molar NaCl solutions – comparing pulse radiolysis experiments with simulations. *in preparation*.

[80] Carbol, P., P. Fors, S. Van Winckel, and K. Spahiu (2009), Corrosion of irradiated MOX fuel in presence of dissolved H2. *Journal of Nuclear Materials* **392**: 45–54.

[81] Carbol, P., K. Spahiu, et al. (2005), The effect of dissolved hydrogen on the dissolution of 233U doped UO2(s), high burn-up spent fuel and MOX fuel. SKB TR-05-09. Svensk Kärnbränslehantering AB, Stockholm.

[82] Cui, D.Q., E. Ekeroth, P. Fors, and K. Spahiu (2008), Surface mediated processes in the interaction of spent fuel or alpha-doped UO2 with H-2. *Actinides 2008 - Basic Science, Applications and Technology* **1104**: 87-99.

[83] Ekeroth, E., M. Jonsson, et al. (2004), Reduction of UO2++ by H2. *Journal of Nuclear Materials* **334**: 35-39.

[84] Fors, P. (2009), The effect of dissolved hydrogen on spent nuclear fuel corrosion. . Chalmers University of Technology, Göteborg, Sweden.

[85] Loida, A., V. Metz, B. Kienzler, and H. Geckeis (2005), Radionuclide release from high burnup spent fuel during corrosion in salt brine in the presence of hydrogen overpressure. *Journal of Nuclear Materials* **346**: 24-31.

[86] Ollila, K., Y. Albinsson, V. Oversby, and M. Cowper (2003), Dissolution rates of unirradiated UO2, UO2 doped with 233U, and spent fuel under normal atmospheric conditions and under reducing conditions using an isotope dilution method, in *TR-03-13*. Svensk Kärnbränslehantering AB, tockholm.

[87] Pastina, B. and J.A. LaVerne (2001), Effect of molecular hydrogen on hydrogen peroxide in water radiolysis. *Journal of Physical Chemistry A* **105**: 9316-9322.

[88] Bruno, J., J. Merino, et al. (2009), MICADO, Model uncertainty for the mechanism of dissolution of spent fuel in nuclear waste repository. Comparison of fitting strategies and uncertainty analyses. Deliverable 3.2. European Commission, Brussels.

[89] Spahiu, K. and P. Sellin (2000), SR 97: Spent fuel alteration/dissolution and the influence of near field hydrogen. *Scientific Basis for Nuclear Waste Management XXIV* **663**: 765-772.

[90] Wittwer, C. (1986). Sondierbohrungen Böttstein, Welach, Riniken, Schafisheim, Kaisten, Leuggern - Probennahmen und chemische Analysen von Grundwässern aus den Sondierbohrungen. NTB 85-49 report, NAGRA, Wettingen, Switzerland.

[91] Ekberg, C. (1999). Uncertainties in actinide solubility calculations illustrated using the Th-OH-PO4 system. Ph. D. thesis, Chalmers University of Technology, Göteborg, Sweden.

[92] Pearson, F.J., D. Arcos, et al. (2003), Mont Terri Project - geochemistry of water in the Opalinus clay formation at the Mont Terri rock laboratory. Bundesamt für Wasser und Geologie, BWG, Bern.

[93] Blair, P. (2008), Modelling of fission gas behavoiur in high burnup nuclear fuel. École Polytechnique Fédérale, Lausanne, Switzerland.

[94] Lewis, B.J. and H.E. Sills (1991), Fission-product transport and the diffusion approximation. *Journal of Nuclear Materials* **184** (2): 107-112.

[95] Wise, C. (1988), The transport of short-lived fission products close to the fuel surface. *Journal of Nuclear Materials* **152** (2-3): 102-113.

[96] Cera, E., J. Merino, et al. (2003), Modelo de alteración del combustible nuclear gastado., in *ENRESA 2003. AGP arcilla.*

[97] Cera, E. (2003), Conceptual model of the Matrix Alteration Model (MAM). Enviros.

[98] Martínez-Esparza, A., M.A. Cunado, et al. (2005), Development of a Matrix Alteration Model (MAM). Publicacíon técnica 01/2005, ENRESA, Madrid, Spain, Madrid.

[99] SFS (2003), 5. EU Framework Programme "Spent Fuel Source", Vorschlag zur Modellierung.

[100] Quiñones, J., E. Iglesias, et al. (2005). Modelling of the spent fuel dissolution rate evolution for repository conditions.Matrix Alteration Model results and sensitivity analysis. Scientific Basis for Nuclear Waste Management XXIX, Gent, September 12-16, 2005, Materials Research Society, Warrendale, Pa. 2006, **932**.

[101] Christensen, H., K. Sehested, and H. Corfitzen (1982), Reaction of hydroxyl radicals with hydrogen peroxide at ambient and elevated temperatures. *Journal of Physical Chemistry* **86**: 1588-1590.

[102] Christensen, H. and K. Sehested (1980), Pulse radiolysis at high temperatures and high pressures. *Radiation Physics and Chemistry* **16**: 183-186.

[103] Christensen, H. and K. Sehested (1981), Pulse radiolysis at high temperatures and high pressures. *Radiation Physics and Chemistry* **18**: 723.

[104] Christensen, H. and K. Sehested (1983), Reaction of hydroxyl radicals with hydrogen at elevated temperatures. Determination of the activation energy. *Journal of Physical Chemistry* **87**: 118-120.

[105] Christensen, H. and K. Sehested (1986), The hydrated electron and its reactions at high temperatures. *Journal of Physical Chemistry* **90**: 186.

[106] Christensen, H. and K. Sehested (1988), HO2 and O2- radicals at elevated temperatures. *Journal of Physical Chemistry* **92**: 3007-3011.

[107] Buxton, G.V., N. Wood, and S. Dyster (1988), Ionization-constants of .OH and HO.2 in aqueous-solution up to 200-degrees-C - a pulse radiolysis study. *Journal of the Chemical Society Faraday Transactions* **84**: 1113.

[108] Elliot, A.J. and D.R. McCracken (1989), Effect of temperature on O- reactions and equilibria. A pulse radiolysis study. *Radiation Physics and Chemistry* **33**: 69-74.

[109] Elliot, A.J. (1989), A pulse radiolysis study of the temperature dependence of reactions involving H, OH and e-aq in aqueous solutions. *Radiation Physics and Chemistry* **34**: 753-758.

[110] Ishigure, K., J. Takagi, and H. Shiraishi (1987), Hydrogen injection in BWR and related radiation chemistry. *Radiation Physics and Chemistry* **29**: 195.

[111] Katsumura, Y., Y. Takeuchi, and K. Ishigure (1988), Radiation chemistry of high temperature water - I. Degradation products in acid by gamma radiolysis. *Radiation Physics and Chemistry* **32** (2): 259.
[112] Katsumura, Y., Y. Takeuchi, D. Hiroishi, and K. Ishigure (1989), Fast-neutron radiolysis of acid water at elevated temperatures. *Radiation Physics and Chemistry* **33**: 299.
[113] Lundström, T., H. Christensen, and K. Sehested (2001), The reaction of hydrogen atoms with hydrogen peroxide as a function of temperature. *Radiation Physics and Chemistry* **61**: 109-113.
[114] Lundström, T., H. Christensen, and K. Sehested (2002), The reaction of OH with H at elevated temperatures. *Radiation Physics and Chemistry* **64**: 29-33.
[115] Lundström, T., H. Christensen, and K. Sehested (2004), Reactions of the HO2 radical with OH, H, Fe2+ and Cu2+ at elevated temperatures. *Radiation Physics and Chemistry* **69**: 211-216.
[116] McCracken, D.R. and G.V. Buxton (1981), Failure of Arrhenius equation for hydroxyl radical-bicarbonate ion reaction above 100oC. *Nature* **292** ( ): 439-441.
[117] Mezyk, S.P. and D.M. Bartels (1995), Direct EPR measurement of Arrhenius parameters for the reaction of H atoms with H2O2 and D atoms with D2O2 in aqueous solution. *Journal of the Chemical Society Faraday Transactions* **91**: 3127–3132.
[118] Schmidt, K.H. (1977), Measurement of the activation energy for the reaction of the hydroxyl radical with hydrogen in aqueous solution. *Journal of Physical Chemistry* **81**: 1257–1263.
[119] Shiraishi, H., Y. Katsumura, et al. (1988), *Journal of Physical Chemistry* **92**: 1113.
[120] Shiraishi, H., G.R. Sunaryo, and K. Ishigure (1994), Temperature dependence of equilibrium and rate constants of reactions inducing conversion between hydrated electron and atomic hydrogen. *Journal of Physical Chemistry* **98**: 5164-5173.
[121] Sehested, K. and H. Christensen (1990), The rate constant of the biomolecular reaction of hydrogen atoms at elevated temperatures. *Radiation Physics and Chemistry / International Journal of Radiation Applications and Instrumentation. Part C* **36**: 499-500.
[122] Sweet, J.P. and J.K. Thomas (1964), Absolute rate constants for H atom reactions in aqueous solutions. *Journal of Physical Chemistry* **68**: 1363-1368.
[123] Wang, T.X. and D.W. Margerum (1994), Kinetics of reversible chlorine hydrolysis: Temperature dependence and general-acid / base-assisted mechanisms. *Inorganic Chemistry* **33**: 1050-1055.
[124] Christensen, H., A. Molander, et al. (1996), Studies of water radiolysis in the INCA loop at 50°C and 150°C. Studsvik Material AB (Studsvik/M-96/180).
[125] Christensen, H. (2006), Calculation of corrosion rates of alpha-doped UO2. *Nuclear Technology* (155): 358-364.
[126] de Pablo, J., I. Casas, et al. (1999), The oxidative dissolution mechanism of uranium dioxide. I. The effect of temperature in hydrogen carbonate medium. *Geochimica et Cosmochimica Acta* **63**: 3097-3103.
[127] de Pablo, J., I. Casas, et al. (1997), Effect of temperature and bicarbonate concentration on the kinetics of UO2(s) dissolution under oxidizing. *Mat. Res. Soc. Symp. Proc.* **465**: 535-542.
[128] Gray, W.J. and C.N. Wilson (1995), in *Spent Fuel Dissolution Studies FY 1991 to 1994*. Pacific Northwest National Laboratory, PNNL, Technical Report, PNL-10540, Richland,Washington, USA.
[129] Johnson, L. and D.W. Shoesmith (1988), Spent Fuel, in *Radioactive Waste Forms for the Future*, W. Lutze, Ewing,R.,, Editor. Elsevier North Holland: Amsterdam.
[130] Loida, A., B. Grambow, and M. Kelm (1999), Abgebrannter LWR-Kernbrennstoff: Auslaugverhalten und Freisetzung von Radionukliden (FZK-INE 009/99), in *Abschlußbericht BfS-Projekt 9G213532100*. Institut für Nukleare Entsorgung (INE), Forschungszentrum Karlsruhe
[131] Karsten, G. (1990). Bisherige Ergebnisse von Auslaugexperimenten an hochabgebranntem oxidischen Brennstoff in Salzlaugen und Wasser. Jahrestagung Kerntechnik, Nürnberg (Germany), May, 15-17, Deutsches Atomforum e.V. Bonn.
[132] Würz, R. and M. Ellinger (1983), Fördervorhaben BMFT KWA 512/4. Kraftwerk Union (KWU): **R914/83/001**.
[133] Würz, R. and M. Ellinger (1986), Fördervorhaben BMFT KWA 512/4. Kraftwerk Union (KWU): **R914/86/013**.
[134] Chotin, F. and P. Pinson (1999). The atelier de compactage des coques (ACC) facility: The R&D Programme. Technologies for the Management of Radioactive Waste from Nuclear Power

Plants and Back End Nuclear Fuel Cycle Activities, Taejon (Korea), August, 30 - September, 03, IAEA.

[135] Lavergne, J.-G.D.d. and B. Boullis (2006), Industrial solutions for long-lived, high- and intermediate-level waste. AREVA & CEA.

[136] Gräbner, H., H. Kapulla, and H. Frotscher (1984), Hülsenkonditionierung. Untersuchungen zur Charakterisierung des Huelsen-Betonproduktes Europäische Kommission, Brüssel: **EUR-9108 DE**.

[137] Kapulla, H. (1984), Kalorimeter zur Bestimmung nuklearer Wärmequellen in MAW-Abfallfässern mit zementierten Hülsen- und Strukturteilen von LWR-Brennelementen aus der Wiederaufarbeitung. Kernforschungszentrum, Karlsruhe: **KfK-3785**.

[138] Wertenbach, H. (1984). Bestimmung von Kernbrennstoffresten in Hülsen nach der Wiederaufarbeitung. Seminar: Neue Entwicklungen auf dem Gebiet der Wiederaufarbeitung, Obertraun (Austria), March, 4-10.

[139] Bähr, W. and S. Kunze (1985), Versuche zur Konditionierung von Brennelementhuelsen und Strukturteilen durch Kaltpressen. Ein alternatives Konzept zum Zementieren von Hülsen. Kernforschungszentrum Karlsruhe: **KfK-3947**.

[140] Köster, R. (1977), Verfestigung von Brennelement-Hülsen und Strukturteilen, Feed-Klärschlämmen (HAW-fest) aus der Wiederaufarbeitung von LWR-Brennstoffen mit Zementen: Teil II. KfK-ABRA: **PWA 75/77**.

[141] Smailos, E. (1979), Berechnung der Temperaturentwicklung bei der Lagerung von zementierten Brennelementhülsen/Feed-Klärschlamm und Strukturteilen aus der WAK in Bohrlöchern in salinaren Formationen. KfK-ABRA: **-**.

[142] Kapulla, H. and R. Heine (1981), -Hülsenkonditionierung - Untersuchungen zur Charakterisierung des Hülsen-Betonproduktes: Kalorimeter zur Bestimmung nuklearer Wärmeleistungsdichten in Hülsen-Fässern. KfK-IT: **PWA 75/81**.

[143] Gräbner, H. (1982), -Hülsenkonditionierung - Untersuchungen zur Charakterisierung des Hülsen-Betonproduktes. KfK-IT: **PWA 52/82**.

[144] Gräbner, H., H. Kapulla, and H. Frotscher (1983), Hülsenkonditionierung: Untersuchungen zur Charakterisierung des Hülsen-Betonproduktes. KfK-Hauptabteilung Ingenieurtechnik: **PWA 47/83**.

[145] Frotscher, H., H. Gräbner, H.K.a. IT), and P. Vejmelka (1986), Untersuchungen zur Fixierung von BE-Hülsenabfällen mit wasserarmen keramischen Zementen. KfK-IT INE: **PWA 14/86**.

[146] Frotscher and Gräbner (1980), Konditionierung von Hüllen bestrahlter Brennelemente durch Walzen und Einbetten in Beton. KfK-IT: **PWA 90/79**.

[147] Frotscher, Gräbner, and Spenk (1979), Konditionierung von Hüllen bestrahlter Brennelemente durch Walzen und Einbetten in Beton. KfK-Hauptabteilung Ingenieurtechnik: **PWA 24/79**.

[148] Frotscher, Gräbner, and Spenk (1980), Konditionierung von Hüllen bestrahlter Brennelemente durch Walzen und Einbetten in Beton. KfK-INE: **PWA 96/79**.

[149] Frotscher, H. (1986), Konditionierung von Hüll- und Strukturmaterialabfällen durch Hochdruckkompaktierung. KfK-IT: **-**.

[150] Frotscher, H. and J. Bernert (1978), Versuchsanlage zur Konditionierung von Hüll- und Strukturmaterialabfällen (Leistungsverzeichnis). KfK-Reaktorbetrieb und Technik: **PWA 46/78**.

[151] Nazare, S. (1985), Studies of hull compaction by powder technological methods - a progress report. KfK-Institut für Material- und Festkörperforschung: **PWA 89/85**.

[152] Sombret, C. (1980), Review of the State of Art of Methods of Conditioning and Storage of Spent Fuel Cladding Hulls, in *PWA 94/79*. KfK-Hauptabteilung Ingenieurtechnik: **PWA 94/79**.

[153] Sombret, C. and G. Spenk (1979), Review of the State of Art of Methods of Conditioning and Storage of Spent Fuel Cladding Hulls, in *PWA 47/80*. KfK-Hauptabteilung Ingenieurtechnik: **PWA 47/80**.

[154] Vehlow, J. and H. Geisert (1983), Messung der Aktivitätsverteilung einiger Nuklide in der Zirkaloy-Hülle abgebrannter LWR-Brennelemente. KfK-Laboratorium für Isotopentechnik: **PWA 77/83**.

[155] Elbachiri, K., P. Doumalin, et al. (2009), Characterization of Local Strain Distribution in Zircaloy-4 and M5 (R) Alloys*. Zirconium in the Nuclear Industry: 15th International Symposium* **1505**: 181-192.

[156] Keller, C. (1993). Grundlagen der Radiochemie. Frankfurt, Aarau, Salzburg, Salle & Sauerländer.

[157] Watteau, M., B. Estève, R. Güldner, and R. Hoffman (2001). Framatome ANP extended burnup experience and views on LWR fuels. World Nuclear Association Annual Symposium, London (UK), September, 5-7.
[158] Würz, H., K. Wagner, and H.J. Becker (1990), Nondestructive determination of residual fuel on leached hulls and dissolver sludges from LWR fuel reprocessing. *Nuclear Engineering and Design* **118** (1): 123-131.
[159] Bleier, A., R. Kroebel, K.H. Neeb, and H.W. Wiese (1987). Kohlenstoff-14 in LWR-Brennstäben und dessen Verhalten beim Wiederaufarbeitungsprozess. Jahrestagung Kerntechnik '87, Karlsruhe (Germany), Kerntechnische Gesellschaft e.V.417-420.
[160] Kienzler, B. and B. Gmal (2007). Critical safe disposal of spent fuel: Behavior of neutron poisons. Global 2007, Boise, Id (USA), ANS1453-1460.
[161] Smailos, E., M.Á. Cunado, et al. (2002), Long-Term performance of candidate materials for HLW / spent fuel disposal containers. European Comission, 5th Euratom Framework Programme 1998-2002: **Second Annual Report**.
[162] Raharinaivo, A., G. Arliguie, et al. (1998). La corrosion et la protection des aciers dans le béton. Paris, Presses de l'École Nationale des Ponts et Chaussées.
[163] Grambow, B., E. Smailos, et al. (1996), Sorption and reduction of uranium(VI) on iron corrosion products under reducing saline conditions. *Radiochimica Acta* **74**: 149-154.
[164] Kupfer, A. (2000), Radiochemische Korrosionsuntersuchungen an Urandioxid und Cladding-Materialien von Kernbrennstoffen in praxisrelevanten Salzlaugen als Beitrag zur direkten Endlagerung. Freie Universität Berlin, Berlin.
[165] HKL Technology (2003), Investigating zirconium hydride formation in nuclear fuel cladding. Available from: http://www.hkltechnology.com/data/0-zriconium-hydride.pdf.
[166] Bourgoin, J., F. Couvreur, et al. (1999), The behaviour of control rod absorber under irradiation. *Journal of Nuclear Materials* **275** (3): 296-304.
[167] Schneider, J., A. Kienzler, et al. (2008), Mechanical structuring, surface treatment and tribological characterization of steel mould inserts for micro powder injection moulding. *Microsystem Technologies-Micro-and Nanosystems-Information Storage and Processing Systems* **14** (12): 1797-1803.
[168] Poinssot, C., C. Ferry, et al. (2005). Mechanisms governing the release of radionuclides from spent nuclear fuel in geological repository: major outcomes of the European Project SFS. Scientific Basis for Nuclear Waste Management XXIX, Gent, September 12-16, 2005, Materials Research Society, Warrendale, Pa. 2006, **932**, 361-368.
[169] Loida, A., R. Gens, et al. (2011). Corrosion behaviour of Spent Nuclear Fuel in high pH solutions. MRS Symposium: Scientific Basis for Nuclear Waste Management XXXV, Buenos Aires (Argentina), Materials Research Society, **1475**.
[170] Bleier, A., M. Beuerle, M. Ellinger, and D. Bohlen (1988), Untersuchungen zum chemischen Status von C14 nach Auslaugung mit einer Salzlösung aus Hüllmaterial bestrahlter DWR- und SWR-Brennelemente, BMFT, Editor. Siemens AG, Erlangen.
[171] Kaneko, S., H. Tanabe, et al. (2002). A Study on the Chemical Forms and Migration Behavior of Carbon-14 Leached from the Simulated Hull Waste in the Underground Condition. Scientific Basis of Nuclear Waste Management, Boston.
[172] Agarwala, R.P. and A.R. Paul (1975), Diffusion of Carbon in Zirconium and Some of Its Alloys. *Journal of Nuclear Materials* **58** (1): 25-30.
[173] Tanabe, H. (2007). Characterization of hull waste in underground condition. International Workshop on Mobile Fission and Activation Products in Nuclear Waste Disposal (MoFAP), L'Hermitage, La Baule (France), January, 16-19.
[174] Vercouter, T., P. Vitorge, et al. (2005), Stabilities of the aqueous complexes $Cm(CO_3)_3^{3-}$ and $Am(CO_3)_3^{3-}$ in the temperature range 10−70 °C. *Inorganic Chemistry* **44** (16): 5833-5843.
[175] Skerencak, A., P.J. Panak, et al. (2009), TRLFS study on the complexation of Cm(III) with nitrate in the temperature range from 5 to 200 degrees C. *Radiochimica Acta* **97** (8): 385-393.
[176] Skerencak, A., P.J. Panak, et al. (2010), Complexation of Cm(III) with Fluoride in Aqueous Solution in the Temperature Range from 20 to 90 degrees C. A Joint TRLFS and Quantum Chemical Study. *Journal of Physical Chemistry B* **114** (47): 15626-15634.
[177] Palmer, D.A., R. Fernández-Prini, and e. A.H. Harvey (2004). Aqueous systems at elevated temperatures and pressures. Amsterdam Elsevier.
[178] Palmer, D.A., P. Bénézeth, D.J. Wesolowski, and L.M. Anovitz (2002), Impact of nickel oxide solubility on pressurized water reactor fuel deposit chemistry. EPRI, Palo Alto, CA and U.S. Department of Energy, Washington D.C.: **1003155**.

[179] Benezeth, P., D.A. Palmer, David J. Wesolowski, and C. Xiao (2002), New measurements of the solubility of zinc oxide from 150 to 350±C. *Journal of Solution Chemistry* **31** (12): 947-973.
[180] Rao, L., D. Rai, and A.R. Felmy (1996), Solubility of Nd(OH)3(c) in 0.1 M NaCl Aqueous Solution at 25°C and 90°C. *Radiochim. Acta* **72**: 151-155.
[181] Giffaut, E. (1994), Influence des ions chlorure sur la chimie des actinides. Universite de Paris-Sud, Orsay, France.
[182] Rai, D., M. Yui, and D.A. Moore (2003), Solubility and Solubility Product at 22°C of UO_2(cr) Precipitated From Aqueous U(IV) Solutions. *J. Solution Chem.* **32**: 1.
[183] Parks, G.A. and D.C. Pohl (1985), Hydrothermal solubility of uraninite. *Geochimica et Cosmochimica Acta* **52**: 863.
[184] Efurd, D.W., W. Runde, et al. (1998), Neptunium and Plutonium Solubilities in a Yucca Mountain Ground Water. *Environmental Science and Technology* **32** (24): 3893-3900.
[185] Tholen, M., J. Hippler, M. Kreienmeyer, and J. Krone (2008), AP7: Nachweiskonzepte für die Einhaltung der nicht radiologischen Schutzziele in der Nachbetriebsphase, in *Überprüfung und Bewertung des Instrumentariums für eine sicherheitliche Bewertung von Endlagern für HAW: ISIBEL*. DBE Technology GmbH, Peine
[186] Weber, J.R., J. Hammer, and O. Schulze (2011), Empfehlungen der BGR zur Berücksichtigung der Kohlenwasserstoff-Vorkommen im Hauptsalz des Salzstockes Gorleben im Rahmen einer vorläufigen Sicherheitsanalyse. Bundesanstalt für Geowissenschaften und Rohstoffe (BGR), Hannover.
[187] Lovley, D.R., D.F. Dwyer, and M.J. Klug (1982), Kinetic analysis of competition between sulfate reducers and methanogens for hydrogen in sediments. *Applied and Environmental Microbiology* **43** (6): 1373-1379.
[188] Ellis, G.S., T. Zhang, Q. Ma, and Y. Tang (2007). Kinetics and mechanisms of hydrocarbon oxidation by thremochemical sulfate reduction. IMOG 2007, Torquay, Devon (UK), September, 9-14.
[189] Machel, H.G. (2001), Bacterial and thermochemical sulfate reduction in diagenetic settings -- old and new insights. *Sedimentary Geology* **140** (1-2): 143-175.
[190] Yue, C., S. Li, K. Ding, and N. Zhong (2006), Thermodynamics and kinetics of reactions between C_1–C_3 hydrocarbons and calcium sulfate in deep carbonate reservoirs. *Geochemical Journal* **40**: 87-94.
[191] Neck, V., M. Altmaier, et al. (2009), Thermodynamics of trivalent actinides and neodymium in NaCl, $MgCl_2$, and $CaCl_2$ solutions: Solubility, hydrolysis, and ternary Ca-M(III)-OH complexes. *Pure and Applied Chemistry* **81** (9): 1555-1568.
[192] Altmaier, M. (2010), Studie zur Abschätzung der standortspezifischen Pu- und Am-Löslichkeiten - Experimentelle Arbeiten zur Absicherung der Modellrechnungen und Maximalkonzentrationen für Plutonium und Americium., in *Projekt Schachtanlage Asse*, KIT-INE, Karlsruhe, *in preparation.*
[193] Altmaier, M., V. Neck, and T. Fanghanel (2004), Solubility and colloid formation of Th(IV) in concentrated NaCl and $MgCl_2$ solution. *Radiochimica Acta* **92** (9-11): 537-543.
[194] Nabivanets, B.I. and L.N. Kudritskaya (1964), Hydroxocomplexes of thorium(IV). *Ukr. Khim. Zh.* **30**: 891
[195] Altmaier, M., V. Neck, R. Muller, and T. Fanghanel (2005), Solubility of ThO_2xH_2O(am) in carbonate solution and the formation of ternary Th(IV) hydroxide-carbonate complexes. *Radiochimica Acta* **93** (2): 83-92.
[196] Altmaier, M., V. Neck, et al. (2006), Solubility of ThO_2xH_2O(am) and the formation of ternary Th(IV) hydroxide-carbonate complexes in $NaHCO_3$-Na_2CO_3 solutions containing 0-4 M NaCl. *Radiochimica Acta* **94** (9-11): 495-500.
[197] Grenthe, I. (1991), Thermodynamics in migration chemistry. *Radiochimica Acta* **55**: 425-432.
[198] Fanghänel, T. and V. Neck (2002), Aquatic chemistry and solubility phenomena of actinide oxides/hydroxides. *Pure Appl. Chem.* **74**: 1895.
[199] Altmaier, M., V. Neck, and T. Fanghänel (2006). Solubility of uranium(VI) in dilute to concentrated NaCl, $MgCl_2$ and $CaCl_2$ solutions. 12th Internat.Symp.on Solubility Phenomena and Related Equilibrium Processes (ISSP 2006), Freiberg (Germany), July, 23-28.
[200] Neck, V., M. Altmaier, et al. (2003). Solubility of U(VI) in NaCl and MgCl2 solutions. Migration`03, Gyeongju (Korea), September, 21-26.
[201] Neck, V., M. Altmaier, et al. (2007), Solubility and redox reactions of Pu(IV) hydrous oxide: Evidence for the formation of PuO_{2+x}(s, hyd). *Radiochimica Acta* **95** (4): 193-207.

[202] Neck, V., M. Altmaier, and T. Fanghanel (2007), Thermodynamic data for hydrous and anhydrous PuO_{2+x}(S). *Journal of Alloys and Compounds* **444**: 464-469.
[203] Neck, V., M. Altmaier, and T. Fanghanel (2007), Solubility of plutonium hydroxides/hydrous oxides under reducing conditions and in the presence of oxygen. *Comptes Rendus Chimie* **10** (10-11): 959-977.
[204] Altmaier, M., V. Neck, J. Lutzenkirchen, and T. Fanghaenel (2009), Solubility of plutonium in $MgCl_2$ and $CaCl_2$ solutions in contact with metallic iron. *Radiochimica Acta* **97** (4-5): 187-192.
[205] Nilsson, H. (2004), The chemistry of plutonium solubility. Chalmers University of Technology, Göteborg, Sweden.
[206] Rai, D., D.A. Moore, et al. (2001), Thermodynamics of the PuO_2^+-Na^+-OH^--Cl^--ClO_4^--H_2O system: use of NpO_2^+ Pitzer parameters for PuO_2^+. *Radiochim. Acta* **89**: 491-498.
[207] Brendebach, B. (2009), persönliche Mitteilung. KIT-INE: Karlsruhe.
[208] Yamaguchi, T., Y. Sakamoto, and T. Ohnuki (1994), Effect of the complexation on solubility of Pu(IV) in aqueous carbonate system. *Radiochim. Acta* **66/67**: 9-14.
[209] Rai, D., N.J. Hess, A.R. Felmy, and D.A. Moore (1999), A thermodynamic model for the solubility of NpO_2(am) in the aqueous K^+-HCO_3^--CO_3^{2-}-OH^--H_2O system. *Radiochim. Acta* **84**: 159-169.
[210] Meyer, R.E., W.D. Arnold, F.I. Case, and G.D. O'Kelley (1991), Solubilities of Tc(IV) Oxides. *Radiochimica Acta* **55**: 11-18.
[211] Eriksen, T.E., P. Ndalamba, J. Bruno, and M. Caceci (1992), The solubility of TcO_2 x nH_2O in neutral to alkaline solutions under constant p_{CO2}. *Radiochim. Acta* **58/59**: 67–70.
[212] Rard, J.A., M.H. Rand, G. Anderegg, and H. Wanner (1999). Chemical Thermodynamics of Technetium. Amsterdam, Elsevier Science.
[213] Olin, Å., B. Noläng, et al. (2005). Chemical thermodynamics of selenium. Issy-les-Moulineaux (France), OECD Nuclear Energy Agency, Data Bank.
[214] Kahl, I., G. Rudolph, and P. Vejmelka (1982), Entwicklung von Puffermaterialien für MAW-Lagerkammern: Verteilungsversuche nit ausgewählten Radionukliden. KfK: **05.12.03P13A**.
[215] Gompper, K. and P. Vejmelka (1998), Nuklidmigration im Deckgebirge des Endlagers für radioaktive Abfälle Morsleben (ERAM). Teil 1: Sorption im Grubengebäude. p. FZK-INE 20/98.
[216] Steinmann, M., P. Stille, W. Bernotat, and B. Knipping (1999), The corrosion of basaltic dykes in evaporites: Ar-Sr-Nd isotope and rare earth elements evidence. *Chemical Geology* **153**: 259-279.
[217] Steinmann, M., P. Stille, et al. (1997). Nd-Sr isotope and REE evidence for the long-term stability of HLW glass products and trace metal migration in a salt repository: corroding basaltic dykes in evaporites as natural analogues. MRS Symposium: Scientific Basis for Nuclear Waste Management XXI, Davos (Switzerland), Materials Research Society, **506**, 1081-1082.
[218] Grambow, B. (2006), Nuclear waste glasses - How durable? *Elements* **2** (6): 357-364.
[219] van Iseghem, P., M. Aertsens, et al. (2006), GLAMOR - A critical evaluation of the dissolution mechanisms of high-level waste glasses in conditions of relevance for geological disposal. EC contract No FIKW-CT-2001-20140.
[220] Ferrand, K., A. Abdelouas, and B. Grambow (2006), Water diffusion in the simulated French nuclear waste glass SON 68 contacting silica rich solutions: Experimental and modeling. *Journal of Nuclear Materials* **355** (1–3): 54-67.
[221] Luckscheiter, B. and M. Nesovic (1996), Langzeitsicherheit der Endlagerung radioaktiver Abfälle: Entwicklung und Charakterisierung eines Glasprodukts für den HAWC der WAK. Forschungszentrum Karlsruhe: **FZKA 5825**.

Annex A

Parameters for modelling the HLW glass dissolution

Tab. A - 1 Parameters for the glass corrosion model after [2]

Parameter	Symbol	Value	Units
Data for the COGEMA glass + canister			
inner diameter of the canister		0.42	m
length of the canister	L_kok	1.338	m
mass fraction of SiO_2 in the glass	f_SI	0.45	-
mass (glass)	Wt_gl	412	kg
density (glass)	rho_gl	2.75	g/cm^3
volume (glass)	V_gl	0.15	m^3
length of partially filled glass cylinder	L_gl	1.08	m
surface area of glass filled part		1.43	m^2
base area (inside)	Q_gl	0.1385	m^2
geometric surface of partially filled cylinder	S_g	1.7039	m^2
surface roughness factor	beta	2	-
diameter of precipitates	d_Ph	1	µm
void volume of the canister	V_leer	0.02	m^3
fraction factor		10	-
total glass surface (incl. fracture surfaces)	S_tot	17	m^2
Canister			
material	steel	1.4833	-
material density	rho_Beh	7.5	g/cm^2
mass	Wt_Beh	80	kg
wall thickness	d_Stahl	0.005	m
outside diameter	d_Beh	0.43	m
outside surface area		2.098	m^2
inside surface area		2.029	m^2
total surface	S_Beh	4.127	m^2
corrosion rate of the steel	r_Beh	0.1	µm/yr
(simplification: temperature independent)		3	g/canister/yr
HLW drillhole			
diameter	d_Bo	0.55	m
annular gap: to be calculated	d_RI	0.06	m
annular gap width	Q_Ri	0.043	m^2
porosity	phi	0.3	-

Parameter	Symbol	Value	Units
tortuosity	lambda	1	-
Scenario-dependent parameters			
linear solution exchange rate	V_adv	0-100	m/yr
max. solution reservoir	V_max	?	m^3
time of solution contact	t_0		
number of canisters per drillhole	NB		
density of the solution	rho_Lsg	1.1-1.35	g/cm^3
composition of the solution	NaCl to $MgCl_2$-rich		
initial Si concentration of the solution	m_ccb	0	mol/L
General parameters			
gas constant	R	8.3145	J
molar weight SiO_2	MW_SiO2	60	g/mol

Tab. A - 2 Composition of HLW glasses. COGEMA min./max. spec.: minimum and maximum values guaranteed by AREVA, CEA-R7T7: Experimentally simulated glass according to the COGEMA specification, SON 68: Composition of a simulated glass representative for the COGEMA/AREVA composition, BNFL Blend1: Composition of a simulated glass representative for the Sellafield vitrification plant, GP WAK1: Composition of a simulated glass representative for the VEK glass, VEK glass: High level radioactive waste glass from the VEK process

Oxides / %	COGEMA min. spec.	COGEMA max. spec.	CEA-R7T7 [34]	SON 68 [220]	BNFL Blend 1 [30], "Stellungnahme Nr. 5"	GP WAK1 [221]	VEK glass
SiO_2	42.4	51.7	46.2	45.48	47.0	50.4	50.40
Al_2O_3	3.6	6.6	4.9	4.91	1.9	2.6	2.60
B_2O_3	12.4	16.5	14.3	14.02	17.2	14.8	14.78
sum SiO_2+B_2O_3+ Al_2O_3	**60**		**65.4**	**64.31**	**66.1**	**67.8**	**67.78**
CaO	3.5	4.8	4.1	4.04	-	4.5	4.54
MgO					2.1	1.80	1.97
Na_2O	8.1	11.0	9.7	9.86	8.5	10.3	10.31
Li_2O	1.6	2.4	2.0	1.98	4.0	2.9	2.94
TiO_2							1.01
ZnO	2.2	2.8	2.5	2.50		0.002	-
sum glass matrix components							**88.55**

Oxides / %	**COGEMA min. spec.**	**COGEMA max. spec.**	**CEA-R7T7 [34]**	**SON 68 [220]**	**BNFL Blend 1** [30], "Stellungnahme Nr. 5"	**GP WAK1 [221]**	**VEK glass**
NiO		0.5	0.4	0.41			0.31
Cr_2O_3			0.5	0.51		0.49	0.44
Fe_2O_3		4.5	2.7	2.91	1.0	1.87	1.68
CoO				0.12			
MnO				0.72		0.34	0.06
P_2O_5		1.0	0.3	0.28		0.38	0.45
ZrO_2			1.0	1.0	2.0		0.60
corrosion-products/ chemicals							**3.48**
UO_2		1.25	0.5	0.52	0.1	1.27	1.19
ThO_2				0.33			-
PuO_2		0.03	0.26		<0.1		0.04
NpO_2			0.0007		0.1		0.09
AmO_2			0.019		0.1		0.08
actinides							**1.40**
waste oxides			**10.6**	**11.25**	**<19.0**	**16.0**	**16.00**
noble metals RuO_2+Rh+Pd		**3.0**			**2.0**	**0.91**	**0.93**
SrO				0.33		0.10	0.16
Cs_2O				1.42		0.59	0.59
La_2O_3				0.90		0.43	0.42
Ce_2O_3				0.93		0.34	0.63
Nd_2O_3				1.59		1.29	0.13
Pr_2O_3				0.44		0.29	0.29
Sm_2O_3						0.25	0.23
Eu_2O_3						0.026	0.03
Gd_2O_3						0.064	0.08
Y_2O_3				0.20		0.13	0.13
Sb_2O_3				0.004		0.002	-
TeO_2				0.24		0.13	0.12
BaO				0.61		0.46	0.46
SnO_2				0.02		0.013	0.01
CdO				0.03		0.016	0.02
SeO							0.02
Ag_2O				0.03		0.02	0.02
TcO_2							0.24
MoO_3				1.7		0.89	0.93

Annex B

Overview on the kinetic models of glass and spent fuel corrosion

1. Glass corrosion:

   The model of [2] differentiates between a short-term and a long-term dissolution rate. As soon as the solution is saturated with respect to SiO_2(am) , which is usually achieved within hours/days, the long-term corrosion rate becomes relevant. Considering the time scales of a nuclear waste repository, the short-term rate can be neglected in a simplified approach, so that only the long-term dissolution is accounted for (cf. Section 3.1.2):

   $$r_{longterm\,rate}(T) = 5.6 \cdot 10^{2} \cdot exp\left(\frac{-7397}{T}\right) \qquad \text{eq. 15}$$

   For this approximation, the long-term corrosion rate was fitted to the temperature in K (unit of the rate is kg m^{-2} day^{-1}).

2. Spent Fuel corrosion:

   - The instant release fraction (IRF) comprises the contribution of radionuclides released from gaps and fissures given in % of the inventory (see Tab. A - 3).

     Tab. A - 3. Best estimate values of IRF (% of total inventory) for various radionuclides for PWR UO_2 fuel (Pessimistic estimate values in brackets [67]).

Burn-up (GWd/t HM)	41	48	60	75
fission gas	1 (2)	2 (4)	4 (8)	8 (16)
^{14}C	10	10	10	10
^{36}Cl	5	10	16	28
^{90}Sr	1 (2)	1 (3)	1 (5)	1 (9)
^{99}Tc, ^{107}Pd	0.1 (1)	0.1 (3)	0.1 (5)	0.1 (9)
^{129}I, ^{135}Cs, ^{137}Cs	1 (3)	2 (4)	4 (8)	8 (16)

   - Release from the matrix depends on the boundary conditions, e.g. H_2 partial pressure. With increasing partial pressure of H_2, decreasing dissolution rates have been observed (inhibition effect). However, experiments in salt brines with traces of Br^- (10^{-4} and 10^{-3} mol $(kgH_2O)^{-1}$) have shown that the presence of Br^- significantly reduces the protective hydrogen effect. Considering the effect of even small concentrations of Br^- on the ^{90}Sr release rate (used as a proxy for the UO_2 matrix dissolution), it is recommended to use a corrosion rate of 10^{-5} FIAP day^{-1} for spent nuclear fuel dissolution in concentrated NaCl and $MgCl_2$ brine at strongly reducing conditions.

- Cladding corrosion: See mobilization of radionuclides from CSD-C wastes (next paragraph)

3. Mobilization of radionuclides from CSD-C wastes:

   Kaneko et al. [171] observed ^{14}C leach rates between 2 - 2.3×10^{-3} yr^{-1} for the oxide layer covering the Zircaloy and 2.9 and $4.6x10^{-5}/yr^{-1}$ for Zry metal. Since there is no information available on the other radionuclides, similar leach rates are assumed.

ISSN 1869-9669
ISBN 978-3-86644-907-7